Thermochemical investigation of molten fluoride salts for Generation IV nuclear applications– an equilibrium exercise

Juliette van der Meer

Thermochemical investigation of molten fluoride salts for Generation IV nuclear applications – an equilibrium exercise

Juliette van der Meer

2006

Thermochemical investigation of molten fluoride salts for Generation IV nuclear applications – an equilibrium exercise

Thermochemisch onderzoek aan gesmolten fluoride zouten voor Generatie IV nucleaire toepassingen – een evenwichtsoefening

(met een samenvatting in het Nederlands)

PROEFSCHRIFT

ter verkrijging van de graad van doctor aan de Universiteit Utrecht
op gezag van de rector magnificus, prof. dr. W.H. Gispen,
ingevolge het besluit van het college voor promoties in het openbaar te
verdedigen op maandag 28 augustus 2006 des ochtends te 10.30 uur

door

Juliette Paola Marguérite van der Meer

geboren op 9 mei 1978, te Alphen aan den Rijn

Contents

Chapter 1

Introduction

Nuclear fission

Nuclear fission is a process in which the nucleus of an atom splits into two or more smaller nuclei, which are called fission products. Fission can happen spontaneously, but also be triggered by the impact of neutrons. During this process, by-products are released that include free neutrons, photons, usually in the form of gamma radiation, and other nuclear fragments such as beta particles and alpha particles. The fission of heavy elements can release huge amounts of energy, both as gamma rays and as kinetic energy of the fragments.

This energy can be converted to electric power by nuclear power plants, it can drive the engines of ships and submarines, but can also drive an explosion in a nuclear weapon. Not all isotopes undergo triggered fission when impacted by a neutron. Only a few are suitable for nuclear fission, which are called fissile
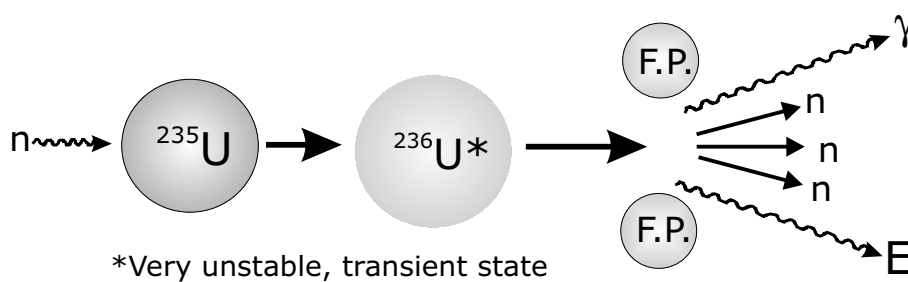
Figure 1.1: The fission of ^{235}U by the impact of a neutron.

elements; the most well-known are ^{235}U and ^{239}Pu. When their nuclei split by the impact of a neutron, other free neutrons are generated, which can sustain the reaction chain. Nuclear reactors make use of the energy that is released at a controlled rate, whereas a very rapid uncontrolled rate causes the explosion in a nuclear weapon.

For each fuel atom that undergoes fission, several hundred MeV of energy are released. In contrast, most chemical oxidation reactions, such as the burning of oil or gas, release at most a few tens of eV per event. Nuclear fuel contains therefore at least ten million times more usable energy per mass than does chemical fuel.

Resources of uranium

At the moment there is an estimated resource of economically minable uranium of about 3.5 Mt on Earth. Most of it is present as orebodies, rich in the minerals uraninite and pitchblende. With the present need of about 68 kiloton uranium per year, it would last for approximately 50 years. There are, however, more reserves that are not economical to mine yet, but which could be made economical by better exploitation techniques or by an increase in the price for uranium ore. These reserves are estimated to be about 13.2 Mt, but this is probably a very conservative estimation. The exploration activity for uranium ore was rather low the last decade. It is expected that when more money is put in exploration, more uranium will be found [1].

The natural abundance of thorium is about three times higher [2]. None of the thorium isotopes are fissile, but ^{232}Th, which is fertile, can via neutron capture and beta decay be converted into ^{233}U, a fissile isotope.

Nuclear reactors

Basically, two reactor types exist, thermal and fast reactors. The neutrons that result from fission are fast and have a high energy. The first reactor type sustains the fission chain by neutrons that have the same average kinetic energy as the surrounding particles. They have a far greater chance to cause another fission than fast neutrons. To slow the neutrons down to the thermal spectrum, a moderator is used. The fast reactor on the opposite, uses the fast neutrons to sustain the reaction. A higher grade of enrichment is needed to start up the reaction, but after that a fast reactor is able to produce its own fuel and even a surplus, which is called breeding. When for example uranium

is used, ^{238}U can capture a fast neutron to become via a couple of steps ^{239}Pu, another fissile isotope. The surplus could be used to start another fast reactor. However, all commercial reactors are thermal reactors.

A nuclear reactor typically consists of the following elements:

Fuel elements. They contain the fissile isotopes. Traditional is to use the isotopes as oxides, although the metallic form can be used as well for certain types of reactors. Pellets are pressed, which are piled up in long pins. The pins are packed together in rods, which form together a fuel assembly. This is illustrated in Figure 1.2.

This is still a common fuel form in nowadays reactors, but several others forms are proposed for the systems of the future, such as coated particles for the so-called pebble bed reactor. Also fissile isotopes in the form of carbides, nitrides or molten salts are studied.

Working fluid, or coolant. It acts as the heat carrier from the reaction vessel to the generator. A common fluid is water, pressurized, or boiling. Gases, as helium or carbon dioxide may also be used. If it is a fast reactor, one does not want the neutrons to slow down to the thermal spectrum. Since water acts as a moderator, it cannot be used as the coolant. Molten metals, such as molten sodium, lead or bismuth-lead are used instead. Molten salts also have excellent coolant properties.

Moderator. If the neutrons that result from fission need to have a lower energy to cause new fissions, water, deuterium or graphite can be used to moderate their energy. When neutrons collide with the neutrons in the nuclei, they will be slowed down. Sometimes, water is used as the coolant and as the moderator at the same time. Deuterium is more effective than normal water, but it is expensive to produce.

Control rods. To control and modify the amount of free neutrons with the desired energy and therefore the rate of the reaction, control rods are used. They are strong neutron absorbers, such as boron carbide, silver, cadmium and hafnium. In emergency cases, when the reaction has to be stopped as quick as possible, the control rods are inserted completely in the reaction vessel.

The spent fuel that is left over after operation consists of a mixture of fissile elements that are still useful and can be recovered by reprocessing, fission products and transuranium elements. Figure 1.3 shows the typical camel-shaped distribution of the fission product yield after thermal fission of ^{235}U. The first "bulge" mainly covers the range of elements between strontium ($Z=$ 87.6) and ruthenium ($Z=$ 101.1); the second between iodine ($Z=$ 126.9) and
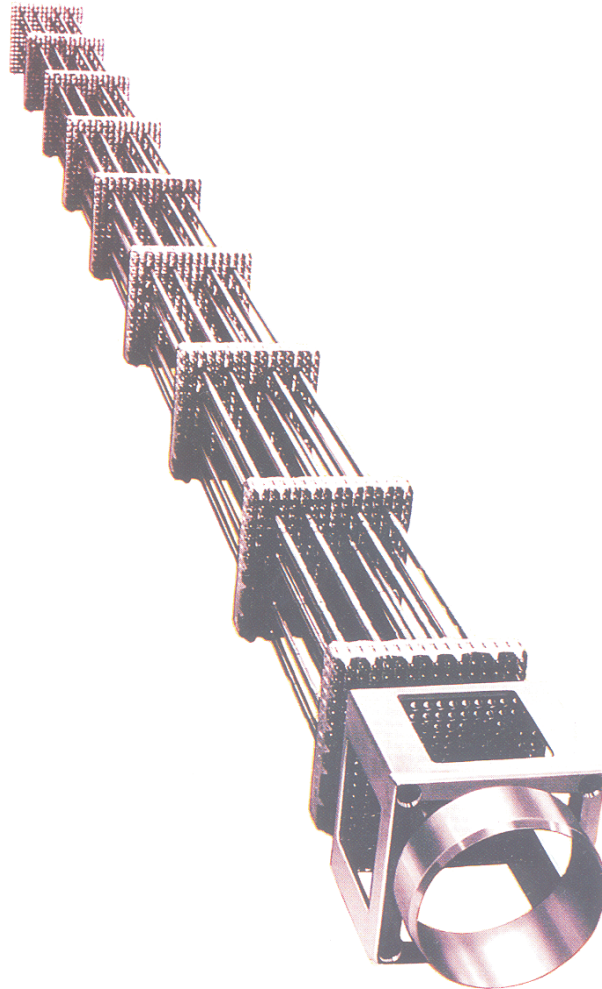
Figure 1.2: Fuel elements for a conventional light water reactor.

neodymium ($Z=$ 144.2). They are mostly radioactive themselves and release a considerable amount of heat. Transuranium elements, or actinides, is the name for all isotopes in the actinide series in the periodic system, but especially meant are the isotopes higher than uranium. They are artificially formed during the fission process by neutron capture by ^{238}U. ^{239}U is formed and by subsequent neutron captures significant percentages of neptunium, plutonium and americium are formed. They are highly radioactive, often with long half-lives. It is generally recognized that the nuclear waste is one of the major disadvantages of the use of nuclear energy. During time, it has been attempted to reduce the volume and toxicity of the waste by several means.

Nuclear reactors through time

Since the early beginnings of nuclear energy in the 1940s, three generations of nuclear reactors have been developed. There were the early prototype reactors in the 1950s and 1960s, followed by a fleet of more advanced reactors in the 1970s and 1980s when nuclear power became commercialized on a wider scale. A third generation of advanced light water reactors arose in the 1990s.

The first commercial nuclear reactor in the United Kingdom was the Magnox reactor in Calder Hall, Cumbria. The name magnox was derived from the magnesium alloy that contained natural uranium as the fuel. It was a gas-cooled reactor built in 1953 and connected to the national grid in 1956. The first commercial reactor in the United States was the Shippingport, a so-called pressurized water reactor (PWR), which got connected to the grid in 1957. Other examples of first generation reactors were the Dresden I in Illinois and the Fermi I in Michigan, both boiling water reactors (BWR).

The PWRs and the BWRs got further developed to what is called now the Generation II reactors. They still form the major part of the United States nuclear reactor fleet. Both use ordinary light water as coolant and moderator. The PWR has two coolant cycles. The first coolant is water under pressure to avoid boiling. This transfers the heat to a second water cycle, which is allowed to boil. The steam drives the turbines and finally the generators to produce electricity. The BWR on the other hand has one coolant cycle. The water is allowed to boil and the steam drives the turbines directly. Typical outlet temperatures for both types are approximately 300 $^{\text{O}}$C.

In Canada the CANDU reactor was developed (CAnada Deuterium Uranium). It uses natural uranium in the form of oxide and heavy water as moderator and
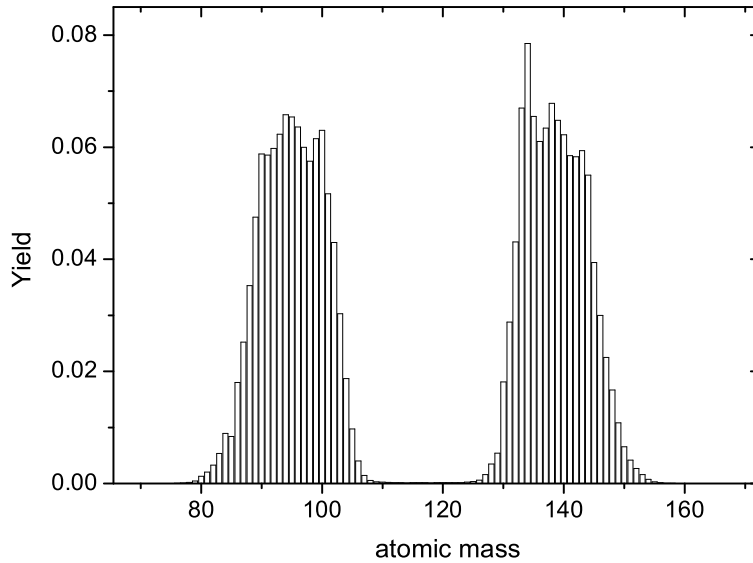
Figure 1.3: Fission product yield distribution after thermal fission of ^{235}U. Data from the American ENDF-BVI nuclear data library.

coolant. The Advanced Gas-cooled Reactor (AGR) was built uniquely in the United Kingdom and uses uranium oxide pellets as fuel, graphite as moderator and pressurized CO_2 gas for cooling. In the same period in the Soviet Union, the RBMK (Reaktor Bolshoj Moshchnosti Kanalnij, or 'large power reactor of the channel type') was operative. It was designed to use low enriched uranium oxide as fuel, graphite as moderator and water as coolant. It was a reactor of this type that exploded in Chernobyl in 1986. The problem with this reactor was the high positive void coefficient. It means that the thermal output of the reactor increases as bubbles form in the liquid moderator or coolant. This can cause a run-away effect as happened during the disaster in Chernobyl.

Since the 1990s, effort was put to modify the existing Generation II reactors to what is called Generation III reactors. It resulted in designs as the Advanced Boiling Water Reactor (ABWR) and the European Pressurized Reactor. They are characterized by more safety features than their predecessors. Other advanced reactors are the Pebble Bed Reactor and the Advanced High Temperature Reactor (AHTR). People tend to see these designs as the intermediate steps between the old Generation II reactors and the systems that will be developed in the farther future in the Generation IV programme.

Generation IV

The world nowadays is facing a growing population with a growing energy consumption. That implies that energy production should increase to meet the demands. In the light of the risks of global warming, reduced or no emission of harmful gases is a necessity; and further, the production should be clean, cost-effective and safe. More and more people have come to realize that nuclear energy will play an important role in the world's energy supply. In 2001, the Generation IV International Forum (GIF) was formed. It is an agreement between ten countries, namely Argentina, Brazil, Canada, France, Japan, the Republic of Korea, the Republic of South Africa, Switzerland, the United Kingdom, the United States and Euratom, which represents the European Union, for international collaboration for the development of the future-generation nuclear energy systems. The goals defined by the Generation IV International Forum are to improve the sustainability, economics, safety and proliferation resistance aspects of the future systems. They are the following:

- The supply of sustainable energy with an effective use of fuel, that promotes long-term availability and that reduces the risk for the environment.

- A minimization of the nuclear waste, as well as its volume and toxicity and an improvement of the protection for the environment and public health.

- Economical competitiveness over other energy sources.

- A financial risk comparable to other energy projects.

- Excellent safety and reliability.

- A very low likelihood and degree of reactor core damage.

- The elimination of the need of off-site response in case of an emergency.

- The fact that the future systems are the most unattractive way for theft of weapon-usable material and an enhanced physical protection against acts of terrorism.

Many reactor concepts were proposed, but finally six were selected as most promising. They are briefly introduced below.

Gas-Cooled Fast Reactor (GFR). It has a fast neutron spectrum, is helium gas cooled and uses ceramic fuel (carbide or nitride) in the form of coated particles or conventional pellets. The typical outlet temperature is 850 ^{O}C. It is primarily designed for electricity production, but hydrogen production is a possibility as well.

Lead-Cooled Fast Reactor (LFR). A fast neutron spectrum is featured, combined with a closed fuel cycle and cooled with molten lead or with a lead-bismuth eutectic melt. The outlet temperature is between 550 and 800 ^{O}C. Small to intermediate sized reactors are foreseen to be installed in remote areas for energy supply. The LFR is primarily envisioned for electricity production, hydrogen production and actinide management.

Sodium-Cooled Fast Reactor (SFR). It has similarities with the LFR. It features a fast neutron spectrum and a closed fuel cycle as well. There are two major options for the design: an intermediate size (150-500 MWe) reactor with a uranium-plutonium-minor actinides-zirconium metal alloy as fuel, or a medium to large size (500-1500 MWe) reactor with a MOX fuel (uranium-plutonium mixed oxide). The outlet temperature is approximately 550 ^{O}C. Electricity production and actinide management are the primary aims for the SFR.

Supercritical Water-Cooled Reactor (SCWR). This type features a thermal neutron spectrum and a once-through uranium fuel cycle. It is a high pressure, high temperature reactor, operating above the thermodynamic critical point of water, which will achieve a thermal efficiency of approximately 45%. It may bear similarities to the LWR or the CANDU reactor, but with a higher thermal efficiency. The outlet temperature is approximately 550 ^{O}C. The primary aim will be electricity production.

Very High Temperature Reactor (VHTR). It has a thermal neutron spectrum and uses a once-through uranium fuel cycle. Its strength will be its flexibility by the small size and the very high coolant temperature of 1000 ^{O}C or higher. Electricity and hydrogen production are primarily envisioned.

Molten Salt Reactor (MSR). This reactor features a thermal to epithermal neutron spectrum. It has a closed fuel cycle with a remarkable feature, namely that the fissile isotopes are dissolved in a molten fluoride salt. A study on the thermodynamic properties, but also the density and viscosity of molten fluoride mixtures that are of interest for MSR application is the main topic of this PhD thesis. The outlet temperature of 700 ^{O}C or higher gives it a high thermal efficiency. The MSR is primarily aimed at electricity generation and

actinide management.

The history of the Molten Salt Reactor

The history of the Molten Salt Reactor started after World War II with the proposal by Bettis and Briant (as a reference in [3]) to design a nuclear-powered aircraft. It was thought as an equivalent to nuclear submarines with an almost unlimited range. For this purpose a Molten Salt Reactor was chosen with its concept based on a liquid fuel that is dissolved in a molten salt loop, making it able to reach a high burn up. Fluorides were chosen as the most desirable solvent for reasons that will be explained. For the use in an aircraft it was important that molten fluoride salts are high temperature-low pressure fluids. This avoided the use of heavy high pressure vessels thus reducing the weight of the plane, while the high temperature maximized the jet engine efficiency.

The aircraft programme resulted in the successful operation of an experimental reactor in 1954, which was called the Aircraft Reactor Experiment (ARE). It was a 2.5 MW(t) reactor operating at a peak temperature of 860 ^{O}C and using a molten NaF-ZrF$_4$ mixture as the solvent for UF$_4$. However, this nuclear aircraft programme was abandoned in the end, because it was realized what the unacceptable risks were in case of an airplane crash. And moreover, the shielding to protect the crew against radiation would be too high for a plane to ever become airborne. But, the principle of a Molten Salt Reactor was not forgotten and found a continuation in the field of civil power production.

Later in the 1960s, the MSR got recognized for its capacities to enable the breeding of ^{233}U in a thermal neutron spectrum. Also its financial support became dependant on its breeding capacities to compete with the Liquid Metal-cooled Fast Breeder Reactor (LMFBR), which was being developed elsewhere in the United States.

The fertile isotope ^{232}Th captures a neutron to become ^{233}Th decaying rapidly to ^{233}Pa, which decays to the fissile isotope ^{233}U, with a half-life of 27 days. It was proven that the best possible solvent for the actinide fluorides was a ^{7}LiF-BeF$_2$ mixture. To retain optimum breeding conditions, it is necessary to reprocess the fuel to remove the fission products that act as neutron poisons. The idea was that a liquid fuel offers advantage and facilitates the chemical reprocessing.

In 1960 engineers at Oak Ridge National Laboratory in Tennessee, USA, started to design the reactor for the Molten Salt Reactor Experiment (MSRE)

and construction started two years after. The reactor became critical in 1965 and at full power a year after. Figure 1.4 shows the design of the MSR as built in Oak Ridge National Laboratory in the 1960s. Numerous experiments were carried out; concerning for example the fuel and solvent composition, fission product deposition, tritium behavior and plutonium additions. This lasted until December 1969 when operation was finally terminated due to the stop of financial support. At that time it was chosen to apply the funds to the development of other reactor concepts.

Design, fuels and construction of the Molten Salt Reactor

Figure 1.5 shows the cross section of the Molten Salt Reactor as designed in the 1970s. It was recognized that the solvent for the fuel should [4]:

- be thermally stable

- be resistant against radiation

- be soluble for uranium, thorium and other actinides

- have, in case of breeding, a small neutron absorption cross section

- have a low vapor pressure, for safety reasons

- exert no reaction with the Ni-alloy cladding of the vessel

- be inexpensive to make the whole system economically viable

Depending on the aim of the reactor, several candidate solvents were selected. For the breeding of uranium from thorium it appeared that a mixture of ^{7}LiF-BeF_2, with approximately 18 mole % BeF_2, would be most suitable. This was studied during the Molten Salt Breeder Reactor experiment (MSBR). The only fluoride of thorium is tetrafluoride and also the majority of the present uranium fluoride appears under typical reactor conditions as tetrafluoride. ^{7}LiF-BeF_2 combines an optimum solubility for actinide tetrafluorides with the smallest neutron absorption cross section. The chosen composition is not the eutectic in the LiF-BeF_2 system; adding more BeF_2 would lower the temperature, but also increase the viscosity of the melt in the same time. The use of ^{7}LiF instead of ^{6}LiF was chosen to lower the tritium production, which damages the cladding and construction materials.

1. Reactor Vessel, 2. Heat Exchanger, 3. Fuel Pump, 4. Freeze Flange, 5. Thermal Shield, 5. Coolant Pump, 7. Radiator, 8. Coolant Drain Tank, 9. Fans, 10. Fuel Drain Tanks, 11. Flush Tank, 12. Containment Vessel, 13. Freeze Valve.
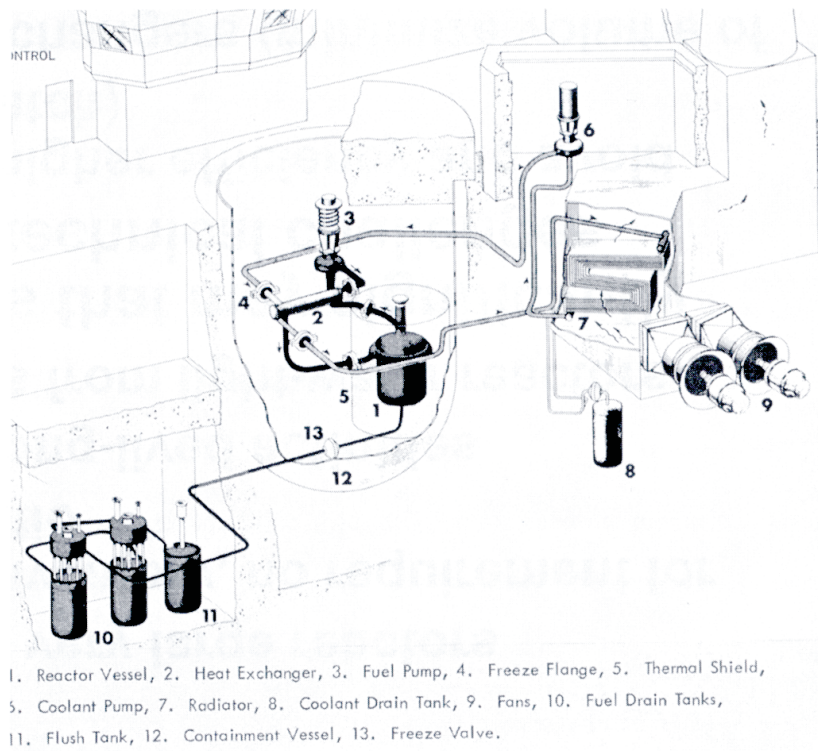
Figure 1.4: Sketch of the Molten Salt Reactor in Oak Ridge National Laboratory.
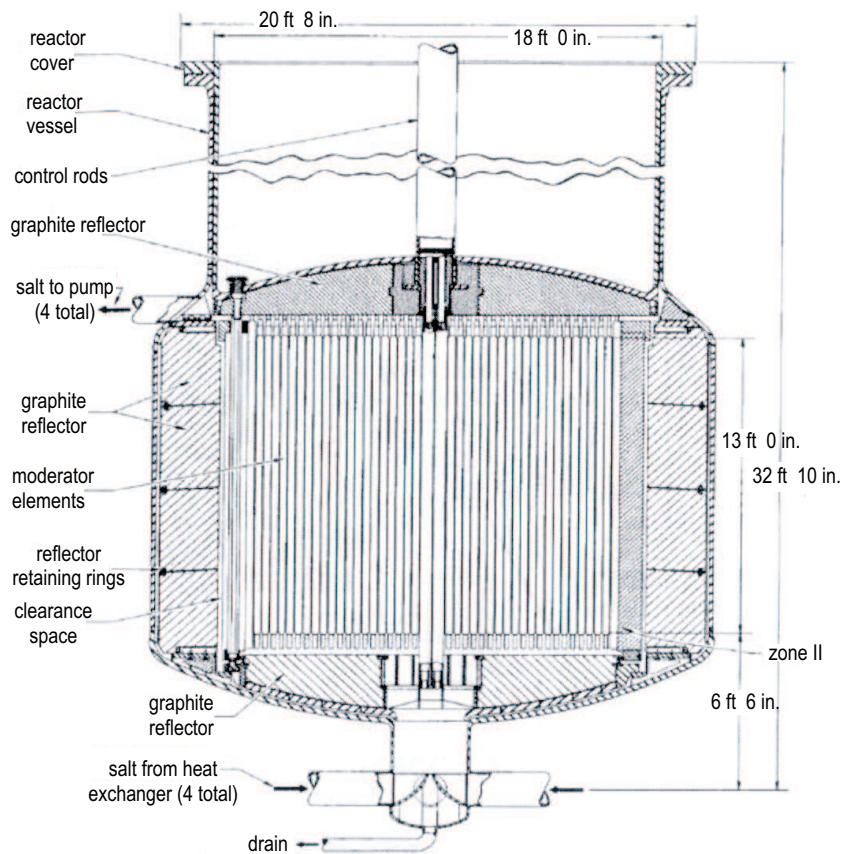
Figure 1.5: Cross section of the 1970s 2250 MW(t) MSR design.

The Molten Salt Reactor Experiment (MSRE) showed that when the burning of uranium was aimed, it was desired to add a small amount of ZrF_4. This would act as an oxygen getter. If a sudden inlet of air or oxygen occurred, ZrO_2 would precipitate instead of UO_2. Table 5.5 lists the properties of the MSRE and MSBR fuels [4].

For the choice of the coolant, several options existed. It was realized that a eutectic mixture of ^7LiF-BeF_2 (52 mole % BeF_2) would be too viscous and relatively expensive due to the use of ^7LiF. Instead, compositions containing NaF were investigated. Some physical properties of NaF-$NaBF_4$, LiF-NaF-BeF_2 and NaF-BeF_2 based coolants are listed in Table 1.2.

The construction material that turned out to have the best corrosion resistance was Hastelloy-N. This is a nickel alloy containing approximately 12% Mo, 7% Cr, 4% Fe, 1% Ti and traces of some other elements. After long-term experiments at ORNL (500 days), the average corrosion by the molten fuel mixture was estimated as less then 0.1 mm per year at an average temperature of 650 ^{O}C [4]. Data on the corrosion by the coolant salt were less extensive, but it was assumed that the corrosion by the coolant would be in the same order of magnitude.

The Molten Salt Reactor as Generation IV initiative

MSR design and operating temperature

After interest in the MSR technology ceased after the 1960s, it was subject of renewed interest in the 1990s. Especially the opportunity to use the thorium cycle on the one hand and the possibility for actinide (waste) burning on the other hand made the MSR suitable for the Generation IV programme. An example of a Molten Salt Reactor design for Generation IV is shown in the cartoon in Figure 1.6. The reaction takes place in a big vessel, moderated by ordinary graphite rods. In the design shown, the inlet temperature of the molten salt containing the fissile isotope(s) is 566 ^{O}C. The heat generated by the fission of ^{233}U, ^{235}U, ^{239}Pu, or other fissile actinide isotopes increases the temperature of the molten salt mixture. The outlet temperature is estimated here as 704 ^{O}C. This hot salt gives off its heat to a coolant, which is also a molten salt. The heat of the coolant salt is converted into energy by a

Table 1.1: **Composition and properties of MSRE and MSBR fuels**

	MSRE fuel	MSBR fuel
composition/mole%	65 LiF	71.7 LiF
	29.1 BeF_2	16 BeF_2
	5 ZrF_4	12 ThF_4
	0.9 UF_4	0.3 UF_4
liquidus temperature	707	773
physical properties (873 K[a])		
density/kg·m^{-3}	2270	3350
heat capacity/J·g^{-1}·K^{-1}	1.966	1.381
viscosity/Pa·s	$9 \cdot 10^{-3}$	$2 \cdot 10^{-3}$
vapor pressure/Pa	negligible	negligible
thermal conductivity/W·m^{-1}·K^{-1}	1.4	1.1

[a] The mean operating temperature

generator.

The estimation for the average temperature differs a bit per project, but it is generally higher than 600 ^{O}C. The TIER project [5] is a design based on an average operating temperature of 650 ^{O}C, which is also foreseen in the Czech SPHINX project [6]. In the further future, if the physical strength and the thermal resistance of the structural materials allow it, the working temperature might be raised a hundred degrees more to reach a higher thermal efficiency. The choice of the solvent and fuel composition is very important, since that fixes the lowest possible temperature in a reactor system. Most of the times, a eutectic (the composition in any chemical system at which the first melt forms) or a near-eutectic composition is chosen for the solvent + fuel mixture.

One of the important aspects of the MSR are its safety aspects. The vapor pressure of molten salt is low in general, enabling the reactor to operate under atmospheric pressures, at 1 bar or slightly higher. One of the worst case scenarios for other reactor designs, a core melt-down, is eliminated here, as the core is already molten. An important feature is the possibility for an emergency shutdown. If it happens that the temperature rises too high, the freeze plug will be released and the salt will automatically be drained in critically

Table 1.2: **Composition and properties of possible MSBR coolants**

	C_1	C_2	C_3
composition/mole%	8 NaF	23 LiF	57 NaF
	92 NaBF$_4$	41 NaF	43 BeF$_2$
		36 BeF$_2$	
liquidus temperature	658	601	613
physical properties (727 K^a)			
density/kg·m^{-3}	1938	2179	2227
heat capacity/J·g^{-1}·K^{-1}	1.506	1.966	1.841
viscosity/Pa·s	$2.5 \cdot 10^{-3}$	$4.0 \cdot 10^{-2}$	$6.5 \cdot 10^{-2}$
vapor pressure/Pa (880 K^b)	$2.67 \cdot 10^{4c}$	negligible	negligible
thermal conductivity/W·m^{-1}·K^{-1}	0.5	1	1

^{a} The mean coolant outlet temperature

^{b} The highest normal coolant operating temperature

^{c} Represents pressure of BF$_3$ in equilibrium with this melt composition
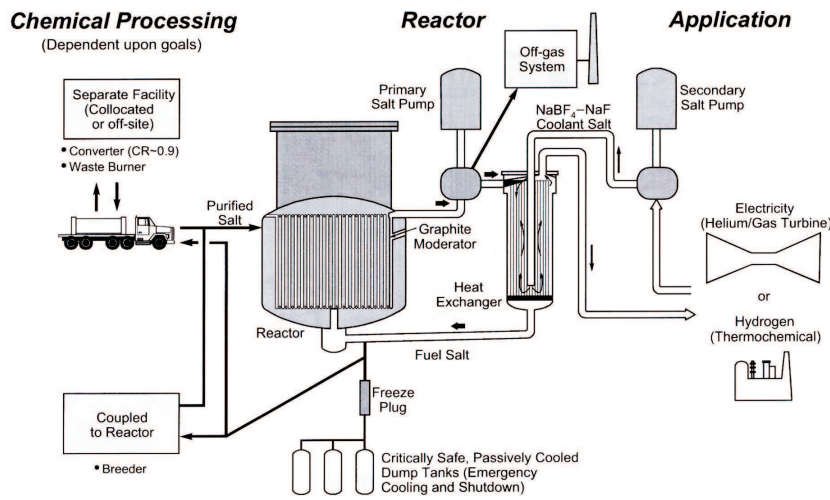
Figure 1.6: The Molten Salt Reactor and its reprocessing and applications scheme as proposed in the Generation IV initiative.

safe, passively cooled dump tanks. Another feature of the MSR design is the possibility of having an online chemical processing plant, where mobile fission products can be removed continuously.

MSR fuels

Several fuel compositions have been proposed. The traditional MSBR (^{7}LiF-BeF$_2$) or ARE (NaF-ZrF$_4$) have already been mentioned. But nowadays alternative fluoride compositions, depending on the aim of the reactor, have been investigated as well. Three concepts exist at the moment: the MSR as thermal breeder, as fast breeder and as fast burner.

Listed are some considerations on the choice of the solvents:

- A ^{7}LiF-BeF$_2$ mixture has a very low solubility of the actinide trifluoride, AnF$_3$, compounds. It is not suited for the fast concepts, because it has a thermal spectrum.

- The AnF$_3$, solubility increases with decreasing BeF$_2$ content and increasing NaF content.

- BeF$_2$ is an excellent component to reduce the melting temperature and should therefore be introduced, despite its toxicity. ZrF$_4$ reduces the melting temperature as well, but has a very negative impact on the reprocessing, since it is reduced to Zr^0 in fluoride melts. Moreover, it is extremely volatile. MgF$_2$ and CaF$_2$ have too little effect on lowering the melting temperature. RbF can be used only in case of the MSR as waste burner. For a breeder is would be less suitable for in-core use due to neutron activation.

- It appears that the tritium production from Li in a MSR is less than in a CANDU heavy water reactor, but it can be lowered by replacing LiF by NaF.

This led to the current options:

A ^{7}LiF-BeF$_2$ mixture as in MSBR for the thermal breeder to have optimum breeding conditions.

A ^{7}LiF-NaF mixture for the fast breeder to have the optimum spectrum.

A ^{7}LiF-NaF-BeF$_2$ for the fast burner to optimize both the spectrum and the AnF$_3$ solubility.

Table 1.3 lists a few important properties of several MSR solvent compositions, where ρ is density, C_p is heat capacity, η is dynamic viscosity and k is thermal conductivity. These parameters are very important to design the reactor, which can be considered as a thermohydraulical problem. Knowledge on the rheological behavior (defined by a.o. ρ and η) and on the heat conduction (defined by a.o. k, ρ and C_p) is indispensable. The data given in the table are after Forsberg [7].

MSR coolants

The options for the coolant salt has not changed since the MSBR design in the 1970s, see Table 1.2. Especially the NaF-NaBF$_4$ mixture is currently considered as a good candidate. Table 1.4 compares the molten salt coolant to other conventional Gen IV coolants. LiF-BeF$_2$ (FLiBe) is considered as a primary in-core coolant, whilst NaF-NaBF$_4$ is suitable as a secondary coolant in a separate loop. The data are after Forsberg [7]. Because of its excellent coolant properties, it is not unlikely that the near future use of molten salt will not be as fuel or coolant in a Molten Salt Reactor, but as the coolant of the Advanced High Temperature Reactor (AHTR) [7].

Development needs

The MSR is a promising concept, but still important parts need to be developed. Molten fluoride salt has many advantages, but also one serious drawback, which is its corrosiveness. A stable cladding material with a long corrosion life-time at very high temperatures is still not available. Of course, the nickel alloy Hastelloy-N has proven to be resistant for a couple of years at working temperatures of 650 ^{O}C ([4]). Also Monel is known as a resistant alloy, but its working temperature is about 540 ^{O}C. One of the strengths of the MSR is its high efficiency due to its high outlet temperature. To reach temperatures above 700 ^{O}C in a reactor running for a couple of decades, improvements ought to be made. Expectations are also set on the use of carbon composites, which could probably turn out as an excellent cladding material, because molten salt does not corrode graphite. Carbon has, however, poor

Table 1.3: **Physical properties of selected MSR solvents**

salt /mole %	at. wt /g·mol^{-1}	T_{fus} /K	ρ /kg·m^{-3}; T/K	C_p [a] /J·g^{-1}·K^{-1}	η /10^{-3} Pa·s	k /W·m^{-1}·K^{-1}
LiF-BeF$_2$ (66-34)	33.1	731	2413-0.4884*T	2.38	0.116 exp(3755/T)	1.1
LiF-NaF-BeF$_2$ (32-31-37)	38.7	588	2000 [a]	2.05	5 [a]	0.97
NaF-BeF$_2$ (57-43)	44.1	633	2371-0.37*T	2.18	0.034 exp(5164/T)	$\sim$ 1
LiF-NaF (61-39)	32.2	922	1985 [a]	$\sim$ 2.1	*unknown*	$\sim$ 0.9
LiF-NaF-KF (11.5-46.5-42)	41.2	727	2729-0.73*T	1.88	0.04 exp(4170/T)	0.6-1
LiF-RbF (43-57)	70.7	748	3488-0.69*T	1.19	0.021 exp(4678/T)	$\sim$ 6
NaF-ZrF$_4$ (50-50)	104.6	783	4044-0.93*T	1.17	0.071 exp(4168/T)	$\sim$ 1
NaF-KF-ZrF$_4$ (10-48-42)	102.3	658	3693-0.89*T	1.09	0.061 exp(3171/T)	$\sim$ 1
LiF-NaF-ZrF$_4$ (10-48-42)	71.56	733	3597-0.83*T	1.46	0.0585 exp(4647/T)	$\sim$ 1

[a] Valid at T=973 K

Table 1.4: **Several coolants proposed in GenIV compared**

	unit	helium 60 bar 773 K	CO$_2$ 60 bar 773 K	water 150 bar 573 K	sodium 1 bar 773 K	LiF-BeF$_2$ 1 bar $T > 723$ K	NaF-NaBF$_4$ 1 bar $T > 723$ K
ρ	kg· m^{-2}	3.7	40.9	726	865	1940	1938
C_p	kJ·kg^{-1}·K^{-1}	5.2	1.2	5.6	1.3	2.3	1.5
$\rho\,C_p$	kJ·m^{-2}·K^{-1}	19.4	48.6	4066	1125	4540	2907
k	W·m^{-1}·K^{-1}	0.29	0.06	0.56	80	1.0	0.5
η	10^{-5} Pa·s	3.8	3.3	9	23.3	563	250

thermal and mechanical properties in a neutron environment, so that research and development for a composite that is less sensitive for neutron corrosion is needed.

One of the claimed advantages of the MSR is the possibility for on-site reprocessing of the salt, i.e. the removal of fission products, preferably in the same medium as the fuel is dissolved in. Techniques to remove the alkalic, earth-alkalic and halogenous fission products are well-developed, but a significant part of the fission products consists of lanthanides. To separate these elements from the fuel (actinides) is far more complicated, because the chemical properties are very similar. An overview of the development in pyrochemical separation methods is given by Nawada and Fukuda [8]. Valuable information is also found in the "PYROREP" final report on the Pyrometallical Processing Research Programme in the European Commission 5th Framework Programme [9]. The Commissariat à l'Energie Atomique (CEA) has developed the liquid-liquid extraction technique between molten salts and liquid alloys in molten chloride and fluoride media [10, 11]. At ITU, important steps have been achieved using electrochemical reprocessing in chloride salts [12]. The advantage of chlorides compared to fluorides is their lower melting temperature, which makes it less expensive to work with. Fluorides are also more corroding then chlorides. From the electrochemical point of view, the electrochemical window for chlorides, i.e. the range where electrolysis can reduce the lanthanides and actinides without reducing the solvent, is far more greater than for fluorides. Therefore, the concept of one solvent serving all purposes is not impossible; it needs however still a lot of research and effort to realize it.

The Molten Salt Reactor is still considered by many in the nuclear field as a very exotic design. The first application of molten salts will therefore probably not directly as a fuel, but as a coolant, combined with an Advanced High Temperature Reactor (AHTR). In the farther future, a reactor with molten salt as the fuel will probably run in combination with a fast breeder reactor, so that the MSR can burn the waste resulting from the fast reactor to close the cycle.

Despite the research and development that need to be done, the MSR is regarded by several parties with great interest. Bowman *et al.* applied already in 1992 for an Accelerator-Driven System (ADS) in combination with a molten salt loop that facilitates the breeding of ^{233}U from ^{232}Th and the burning of transuranium elements at the same time [13]. In France, Electricité de France (EDF) [14], the Centre National de la Recherche Scientifique (CNRS)

and the CEA do a lot of research and also countries as the Czech and Slovak Republic have adopted the MSR concept. And some scientists, as Moir and Teller [15], are optimistic and foresee and describe an underground thorium-fuelled breeder reactor, complete with waste storage and power plant.

1

The scope of this thesis

This thesis deals with the thermochemical properties of molten salt fuels. For the design of a reactor, it is important to know at what temperature a certain fuel composition melts or decomposes. In the 1960s, during the MSRE and MSBR programmes, numerous phase diagrams were measured, for systems with two or three components. But it is impossible to measure every single composition one might be interested in, so a solution is to develop a model, which is able to predict the phase behavior not only for binary or ternary, but also for higher order systems.

The thermodynamic models in this study are based on the critical assessment of available information in the literature on thermodynamic properties and experimental data. We also performed thermal and calorimetric experiments ourselves to incorporate them in the models. In addition, other physical properties as density, vapor pressure and viscosity were included as well.

Chapter 2 focuses on the calorimetric analysis of NaF, NaLaF$_4$ and ThF$_4$. It describes the techniques of differential scanning calorimetry and low temperature adiabatic calorimetry.

The thermodynamic assessment of some selected MSR solvents is the topic of Chapter 3. The quasi-chemical model is introduced here. It contains the modelling and/or measurements on the systems LiF-BeF$_2$, NaF-BeF$_2$, LiF-NaF and NaF-ZrF$_4$.

---

[1]Sources that were not referred to explicitly in the text:

on Generation IV: Khalil [16],

on the history of the MSR: Forsberg [7],

on the present MSR developments: Forsberg [7] and Konings *et al.* [17].

The fuels for the MSR option are central in Chapter 4. The LiF-NaF-MF$_3$ (M = La, Ce, Pu) systems are highlighted. The modified quasi-chemical model with quadruplet approximation is introduced, as well as the calculation of ternary diagrams from binaries. The effect of adding the melting temperature lowering substance RbF is investigated.

Chapter 5 deals with the MSR Breeder fuel LiF-BeF$_2$-ThF$_4$-UF$_4$, which is still the reference fuel in all reactor designs. The thermodynamic models are expanded with properties as vapor pressure, density and viscosity. The contents of the chapters 2 to 5 have already been published during the study or were submitted/accepted as manuscripts for publications.

Chapter 6 gives a brief outlook on the continuation of the study that is described in this thesis, to satisfy our scientific curiosity, but also seen in the light of the development needs for the Generation IV Molten Salt Reactor.

Chapter 2

Calorimetry

In this Chapter, the technique of differential scanning heat flux calorimetry is explained. We used a salt, of which the heat capacity is well-known, NaF, to test the equipment. After satisfactory results, we performed similar experiments on $NaLaF_4$. The method of synthesis and characterisation are explained and discussed. In addition, low temperature adiabatic calorimetric analysis was performed on this salt. The two heat capacity series from the low and the high temperature measurements fit smoothly. The resulting C_p function was used in a reassessment of the binary system $NaF-LaF_3$, as will be discussed in Chapter 4 *MSR Burner Fuels*. The contents of this Chapter were published as the paper: Van der Meer, Konings, Sedmidubský, Van Genderen and Oonk, "Calorimetric analysis of NaF and $NaLaF_4$", J. Chem. Thermodyn. (in press).

Differential Scanning heat flux calorimetry

A Setaram Multi-HTC calorimeter, equipped with a HF-DSC (Heat Flux Differential Scanning Calorimetry) detector, see Figure 2.1, was used to measure the heat capacity at high temperatures (> 550 K). Temperature calibration was performed with metals (Sn, Zn, Al, Ag, Au) in aluminum oxide crucibles. The metals were tested at three different heating rates: 1, 2 and 5 K·min^{-1},

which provided well-defined, weakly concave parabolic functions. It appeared that the smallest deviations ($\pm 1\%$) from the literature values were obtained with the lower rates. After this, four different salts (Ag_2SO_4, CsCl, $BaCO_3$, LiF) were tested in platinum crucibles at the same heating rates. The data points obtained for a given heating rate did not fit in a neat curve, but were scattered around the curve for the metals in Al_2O_3 with the same heating rate.

A platinum crucible, with a boron nitride liner (grade AX05) and a cover, was filled in a dry and pure argon atmosphere with the powdered sample. A picture of the crucible with a length of 20 mm and an outer diameter of 7 mm is shown in Figure 2.3. Then it was quickly transported in a closed capsule to the calorimeter where it was loaded immediately together with an identical empty crucible which was used as the reference. Figure 2.2 is a cross section from the detector. The thermopile, existing of 28 thermocouples, enables an optimum heat flow detection.

All measurements were carried out under a continuous argon (grade 5.0) flow using the C_p-by-step method. This is explained in Figure 2.4. The sample was heated stepwise and during every step the response, i.e. the peak was recorded. Intervals of 1.5 to 2 hours between the steps were used to let the instrument equilibrate after each temperature increment. After the experiment, the peak areas were integrated and converted to heat capacity values. For each experiment, three different runs were needed: a run with a sample as was described above, a blank run for the background measurement completed by a run with a standard reference material (α-Al_2O_3) to obtain a function for the sensitivity. All runs were performed with identical temperature programs.

To process the experimental data, the software package DSCEval [18] was used. The peaks obtained for the sample were corrected for the background signal. Hereafter the signals were converted to C_p values using the sensitivity function.

The heat capacity of solid NaF

To prove the validity of the high temperature DSC measurements, we first measured pure NaF salt (800 mg) and compared the data to the C_p function which was derived from the known enthalpy function. Table 2.1 shows these data for NaF.

Figure 2.1: The Setaram Multi-HTC calorimeter, with a closeup from the detector.
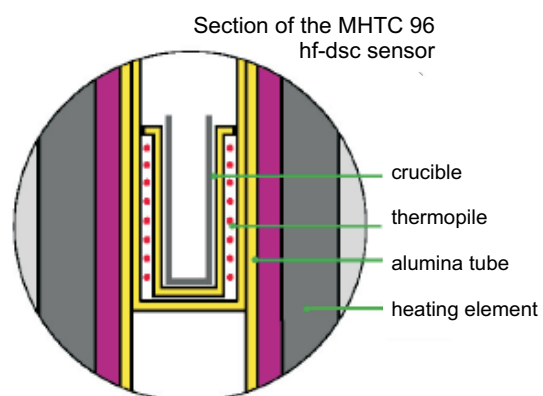

Figure 2.2: A cross section from the Multi-HTC detector.

Figure 2.3: The platinum crucibles with a cover and a boron nitride liner, as used in the experiments.
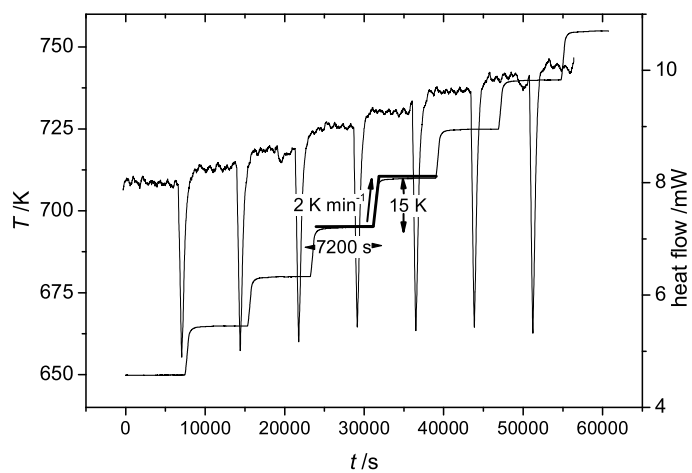
Figure 2.4: Example of a C$_p$-by-step run. The step indicated has a size of 15 K, a rate of 2 K·min^{-1} and a duration of 7200 s.

Table 2.1: **Heat capacity data of NaF; high temperature measurements**

T	C_p^0	T	C_p^0	T	C_p^0
/K	/J·K^{-1}·mol^{-1}	/K	/J·K^{-1}·mol^{-1}	/K	/J·K^{-1}·mol^{-1}
630.6	58.08	870.6	58.37	952.5	59.98
645.6	58.11	885.5	59.37	967.5	60.92
675.7	59.55	900.5	59.70	982.6	60.11
690.6	59.36	915.5	60.11	997.5	60.91
720.6	58.15	945.5	59.64	1012.6	61.02
735.5	59.11	960.6	60.43	1027.6	60.56
750.6	58.85	975.4	59.89	1042.6	61.86
765.6	59.28	990.5	61.01	1057.7	61.63
795.6	58.36	907.5	59.76	1072.7	62.08
825.5	58.26	922.3	60.21	1087.8	62.41
840.4	58.49	937.4	60.58	1102.9	62.25
855.6	59.14				

A graph is shown in Figure 2.5 containing the high temperature heat capacity data for solid NaF. Added are the low temperature data from King [19] that appear to fit smoothly with the high temperature run. Moreover, the inset graph shows the enthalpy data from O'Brien and Kelley [20] and Macleod plotted as $(H^0(T/\mathrm{K}) - H^0(298.15\ \mathrm{K}))/(T\text{-}298.15\ \mathrm{K})$ together with our own data, which were recalculated to the same units for this purpose. It should be noted that the measurement series from Macleod is considered as the more accurate, as it has been suggested that an analytical error exists in the temperature measurements by O'Brien and Kelley [21]. It can be seen that our data, integrated to an enthalpy function mainly overlaps with the data from Macleod. Above 900 K the two series start to diverge, which can probably be ascribed to a decline in precision in our heat capacity measurements at higher temperatures.

The low temperature C_p data by King and our high temperature C_p data, combined with the high temperature enthalpy data by Macleod, fit according to the function for T= 250 K to T_{fus} (1269 K):

$$C_p(T) = 47.63 \; + \; 1.479 \cdot 10^{-2} \; T \; - \; 4.643 \cdot 10^5 \; T^{-2} \qquad (2.1)$$

It can be seen that our C_p data coincide almost exactly with the combined

fit. After the satisfying results on NaF, the similar procedure was applied to $NaLaF_4$.

The heat capacity of solid $NaLaF_4$

The synthesis of $NaLaF_4$

As fluoride salts are hygroscopic, sample preparation and measurements were carried out in an inert argon atmosphere. NaF 99.99% (on metals basis) and LaF_3 99.99% (REO) from Alfa Aesar were used. The two salts was purified before use. A few grams of powdered salt in an open nickel container were heated under vacuum in a Monel tube furnace to 423 K and kept at this temperature for 12 hours. Immediately after, the salts were transported to a glovebox, which was filled with dry and pure argon (grade 5.0) gas.

In here, amounts of NaF and LaF_3 were carefully weighed and mixed. The synthesis was performed *in situ* in the Setaram Multi-HTC heat flux calorimeter. Platinum crucibles with a cover and with a boron nitride liner were filled with the salt mixture. The compound $NaLaF_4$ melts peritectically around 1060 K [23, 24]. To reach an optimum mixing, the salt samples were heated above the melting temperature, up to 1100 K at a rate of 5 $K \cdot min^{-1}$. Then they were slowly cooled at a rate of 2 $K \cdot min^{-1}$ down to 1043 K and the samples were kept for 24 hours at that temperature. After a rapid cooling to room temperature, the samples were immediately transported to the argon glovebox.

X-Ray Diffraction

X-Ray Diffraction analysis was performed on a sample of powdered $NaLaF_4$. In the past, Zachariasen [25] and Burns [26] made a XRD analysis on this compound and they found a trigonal and a hexagonal phase, respectively. It should be noted that, despite the fact that different crystal structures were reported, their results do not differ much. The former found a space group of P321, with cell parameters a=b = 617.47 pm, c = 382.62 pm, while the latter reported $P\bar{6}$ as space group with parameters a=b = 615.7 pm, c = 382.2 pm, which
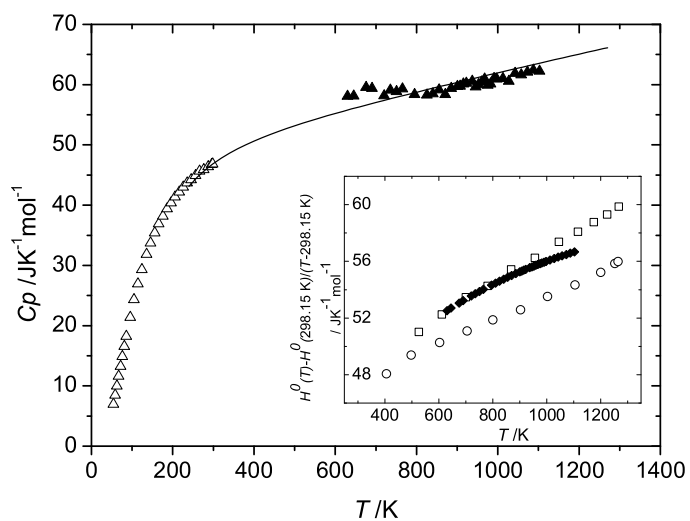
Figure 2.5: Heat capacity data of solid NaF. △ low temperature measurements by King [19]; ▲ our data obtained by heat flow calorimetry; solid line: the combined fit between the low temperature C_p data [19], our high temperature C_p data and the high temperature enthalpy data by Macleod [22]. Inset graph: □ enthalpy data by Macleod [22]; ○ enthalpy data by O'Brien and Kelley [20]; ♦ our data recalculated to enthalpy data.

suggests that the hexagonal cell can be superposed to the trigonal cell. Our results, for which the cell parameters a=b = 617.471 $\pm$ 0.072 pm, c = 382.62 $\pm$ 0.058 pm were found, are in agreement with the findings from Zachariasen, as our XRD spectrum fitted best with the parameters for a trigonal phase. A tiny peak at $2 \Theta = 36^o$ could not be ascribed to the presence of LaF_3, NaF, LaOF or any $La(OH)_n$ compound and could not be identified.

Low temperature heat capacity

The low temperature heat capacity was measured by the adiabatic calorimeter CAL V, which was developed at the Chemical Thermodynamics Group of Utrecht University [27]. The accuracy of the machine was checked for the 10-100 K range using n-heptane and from 100-400 K with sapphire (NBS Standard Reference Material 720). The differences between the measured values and the literature data were smaller than 0.1 %. In a glovebox operating under a dry nitrogen atmosphere, the sample (4.31 g) was loaded in a gold container and carefully placed in the calorimeter. The sample was cooled and analyzed in two stages, first to liquid N_2 temperature and subsequently to the temperature of liquid He. Seven measurement series were performed of which an overview is given in Table 2.2.

High temperature heat capacity

The Setaram Multi-HTC calorimeter was used to measure the heat capacity of $NaLaF_4$ from 623 to 1213 K. It was not possible to perform the analysis immediately after the synthesis in the calorimeter, because a space was formed between the sample and the crucible wall, so that the thermal contact was too small. It had to be taken out and crushed in the argon glovebox. The crucible was filled with 700 mg of the sample. The specific temperature program was the following: from 473 to 1028 K a step size of 15 K, a heating rate of 2 K·min^{-1} and an isothermal step of 7200 s were selected. From 1018 to 1078 K a more detailed run was performed with a step size of 5 K, a rate of 2 K·min^{-1} and an isothermal step of 5400 s. In the molten phase from 1053 to 1213 K the parameters 20 K, 2 K·min^{-1} and 7200 s were chosen.

Table 2.2: **Measurement series adiabatic calorimetry**

Series	T range (K)
1	298-394
2	94-214
3	6-30
4	5-25
5	28-100
6	103-300
7	277-399

Heat capacity of NaLaF$_4$ at low and high temperature

The data which were obtained by the low temperature adiabatic measurements are presented in Table 2.4 in the Appendix *Data tables for NaLaF$_4$ heat capacity measurements*. Note that an analytical error exists of $\pm$ 0.5%, based on the deviation from the used standards [27]. The data obtained by the high temperature heat flux calorimetric measurements on NaLaF$_4$ are presented in Table 2.5.

Data from the low temperature series 3 and 4, covering the temperature range from 5 to 30 K, were plotted against T^3 to find a linear relationship. The value of this parameter was used to calculate the initial values for the integration from 10 K for H and S^0. The data were fitted according to the function:

$$C_p/(\text{J} \cdot \text{K}^{-1} \cdot \text{mol}^{-1}) = 4.23 \cdot 10^{-4} \ (T/\text{K})^3 \tag{2.2}$$

This equation results in $S^0(10 \text{ K})= 0.141$ J·K^{-1}·mol^{-1} and $H(10 \text{ K}) = 1.0575$ J·mol^{-1}. The heat capacity and entropy values were determined by numerical integration followed by interpolation of the values of the experimental data points. The results can be found in Table 2.3. Added are the values that were derived from the high temperature measurements. The values between 400 and 600 K are obtained by interpolation between the low and the high temperature series.

The following values at T=298.15 K were extracted from Table 2.3:

$$C_p(298.15 \text{ K}) = 139.1 \text{ J} \cdot \text{K}^{-1} \cdot \text{mol}^{-1} \tag{2.3}$$

Table 2.3: **Heat capacity and entropy of NaLaF$_4$ at selected temperatures from 10 to 1200 K**

T	C_p^0	$S^0(T)$	T	C_p^0	$S^0(T)$
/K	/J·K^{-1}·mol^{-1}	/J·K^{-1}·mol^{-1}	/K	/J·K^{-1}·mol^{-1}	/J·K^{-1}·mol^{-1}
10	0.655	0.141	120	86.4	59.1
15	1.58	0.479	130	92.5	66.3
20	3.29	1.14	140	97.9	73.3
25	6.18	2.16	150	102.9	80.3
30	8.72	3.50	160	107.3	87.0
35	13.4	5.20	170	111.5	93.6
40	16.7	7.19	180	115.0	100.1
45	21.3	9.41	190	118.3	106.4
50	26.1	11.9	200	121.3	112.5
55	31.1	14.6	210	123.8	118.5
60	35.9	17.5	220	126.1	124.3
65	40.5	20.6	230	128.5	130.0
70	45.3	23.8	240	130.8	135.5
75	50.1	27.1	250	132.9	140.9
80	54.9	30.4	260	133.4	146.1
85	59.6	33.9	270	135.3	151.2
90	64.0	37.4	280	136.9	156.1
95	68.3	41.0	290	138.6	160.9
100	72.3	44.6	298.15	139.1	164.8
105	76.0	48.2	300	139.7	165.7
110	79.7	51.9	310	140.2	170.2

Table continued from previous page.

T	C_p^0	$S^0(T)$	T	C_p^0	$S^0(T)$
/K	/J·K^{-1}·mol^{-1}	/J·K^{-1}·mol^{-1}	/K	/J·K^{-1}·mol^{-1}	/J·K^{-1}·mol^{-1}
320	141.0	174.7	725	170.9	300.4
330	141.9	179.0	750	172.9	306.2
340	142.7	183.3	775	175.0	311.9
350	143.2	187.4	800	177.1	317.5
360	143.8	191.5	825	179.3	323.0
370	144.3	195.4	850	181.5	328.4
380	144.6	199.3	875	183.8	333.7
390	145.1	203.0	900	186.0	338.9
400	146.8	206.8	925	188.4	344.0
425	148.6	215.7	950	190.7	349.1
450	150.4	224.3	975	193.1	354.0
475	152.1	232.5	1000	195.6	359.0
500	153.9	240.3	1025	198.1	363.8
525	155.7	247.9	1050	200.6	368.6
550	157.5	255.1	1075	203.2	373.4
575	159.3	262.2	1100	205.8	378.1
600	161.1	269.0	1125	208.4	382.7
625	163.0	275.6	1150	211.1	387.3
650	164.9	282.1	1175	213.9	391.9
675	166.9	288.3	1200	216.7	396.4
700	168.9	294.4			

$$S^0(298.15 \text{ K}) = 164.8 \text{ J} \cdot \text{K}^{-1} \cdot \text{mol}^{-1} \qquad (2.4)$$

$$H^0(298.15 \text{ K}) - H^0(0 \text{ K}) = 25901 \text{ J} \cdot \text{mol}^{-1} \qquad (2.5)$$

After processing the data of the heat flow calorimetric measurements, both series, for the low and the high temperature, were plotted in Figure 2.6, with a more detailed plot of the data excluding the prominent peak in Figure 2.7. The function that fits the C_p function for $298.15 < T/\text{K} \le 1010$ K, with an average error of 0.75%, is:

$$C_p(T) = 132.61 + 2.9109 \cdot 10^{-2}\,T + 3.4332 \cdot 10^{-5}\,T^2 - 4.6607 \cdot 10^5\,T^{-2} \quad (2.6)$$

The peak at 1060 K is interpreted as the decomposition of NaLaF$_4$, since it is known as an incongruently melting compound [28, 23], giving rise to the peritectic in the binary system NaF-LaF$_3$. Above this temperature, the compound is decomposed in solid LaF$_3$ plus a liquid, persisting in equilibrium up to 1400 K, where the liquidus is crossed [24]. The data from 1060 to 1213 K in Figure 2.6 can therefore not be interpreted as the C_p of liquid NaLaF$_4$.

Comparison with the Neumann-Kopp rule

Figure 2.7 also shows the empirical C_p of NaLaF$_4$ according to the Neumann-Kopp rule. The C_p functions of NaF and LaF$_3$, which are used in Chapter 4 *MSR Burner Fuels* to assess LiF-NaF-LaF$_3$, are added here. It can be seen that this rule is only valid in the temperature range between 300 to 700 K. At higher temperatures the Neumann-Kopp considerably underestimates the observed C_p data, probably because the lattice interactions in the compound are significantly different compared to those in the pure components, leading to different anharmonic contributions to the heat capacity.

Summary on calorimetry

The heat capacity of solid NaF was measured using differential scanning heat flux calorimetry. The results show a good agreement with the low temperature
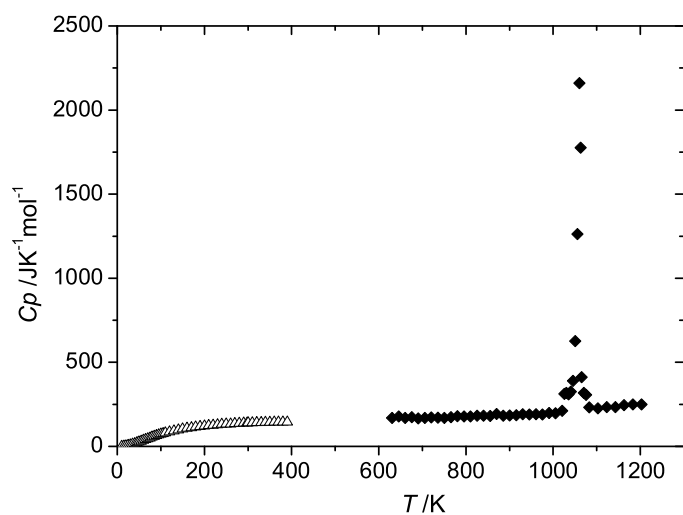
Figure 2.6: Heat capacity measurements on NaLaF$_4$. $\triangle$ obtained by adiabatic calorimetry; $\blacklozenge$ obtained by heat flow calorimetry.
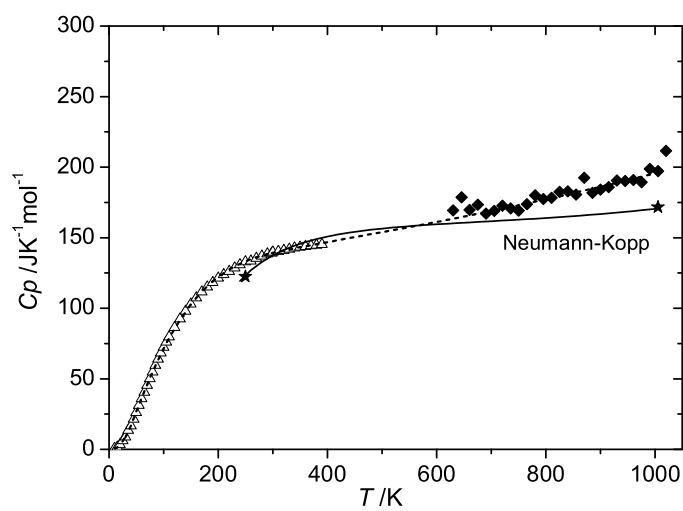
Figure 2.7: Detailed image of the heat capacity data of NaLaF$_4$ together with the fitting function till 1000 K plotted.

data by King [19] on the one hand and with the high temperature data by Macleod [22] on the other hand.

The similar technique was applied on $NaLaF_4$, which was synthesized *in situ* from NaF and LaF_3 in the calorimeter and its purity was checked by XRD analysis. In addition to the high temperature heat capacity measurements, adiabatic calorimetry was used to perform low temperature measurements, from 4 to 400 K, as well. The two data series fitted smoothly.

A comparison with the Neumann-Kopp rule showed that the sum of the C_p of NaF and LaF_3 describes the experimental curve well up to about 700 K. Above this temperature the empirical C_p values are smaller than the experimental values, probably due to the fact that the lattice interactions in the compound start to differ significantly from those in the pure components.

Data tables for NaLaF$_4$ heat capacity measurements

Table 2.4: **Heat capacity data of NaLaF$_4$; low temperature measurements by adiabatic calorimetry**
Series 1

T/K	C_p/J·K^{-1}·mol^{-1}	T/K	C_p/J·K^{-1}·mol^{-1}	T/K	C_p/J·K^{-1}·mol^{-1}
298.39	139.3	332.21	143.3	363.74	145.9
300.40	139.7	334.18	143.5	365.72	146.1
302.41	139.9	336.15	143.4	367.70	146.3
304.41	140.1	338.12	143.7	369.68	145.7
306.41	140.5	340.09	143.8	371.67	146.1
308.40	140.8	342.06	144.0	373.65	146.5
310.40	141.0	344.03	144.1	375.64	146.4
312.39	141.3	346.00	144.2	377.63	146.2
314.38	141.7	347.97	144.4	379.63	145.9
316.37	141.9	349.94	144.4	381.63	146.3
318.35	141.8	351.91	144.6	383.64	146.3
320.34	142.0	353.88	145.1	385.65	146.2
322.32	142.4	355.86	144.7	387.67	146.5
324.30	142.6	357.83	145.0	389.69	146.4
326.28	142.8	359.80	145.3	391.71	146.8
328.26	143.2	361.77	145.7	393.74	146.8
330.23	143.4				

Series 2

T/K	C_p/J·K^{-1}·mol^{-1}	T/K	C_p/J·K^{-1}·mol^{-1}	T/K	C_p/J·K^{-1}·mol^{-1}
93.73	66.87	134.65	95.17	176.27	113.8
95.64	68.81	136.63	96.16	178.26	114.5
97.56	70.37	138.60	97.17	180.25	115.1
99.48	71.80	140.57	98.34	182.24	115.9
101.41	73.33	142.55	99.41	184.23	116.4
103.34	74.87	144.53	100.4	186.22	117.2
105.28	76.29	146.51	101.3	188.21	117.8
107.22	77.82	148.49	102.2	190.20	118.3
109.16	79.27	150.47	103.2	192.19	119.0
111.11	80.67	152.45	104.1	194.18	119.5
113.06	81.87	154.43	105.0	196.17	120.3
115.01	83.19	156.41	105.9	198.16	120.8
116.96	84.63	158.40	106.7	200.16	121.2
118.92	85.72	160.38	107.5	202.15	122.1
120.88	86.98	162.37	108.3	204.14	122.3
122.84	88.13	164.35	109.3	206.14	123.0
124.81	89.42	166.34	109.8	208.13	123.4
126.77	90.74	168.32	110.7	210.12	123.8
128.74	91.87	170.31	111.7	212.12	124.4
130.71	92.93	172.30	112.3	214.11	124.8
132.68	94.07	174.28	113.1		

Series 3

T/K	C_p/J·K^{-1}·mol^{-1}	T/K	C_p/J·K^{-1}·mol^{-1}	T/K	C_p/J·K^{-1}·mol^{-1}
6.44	0.112	15.45	1.81	22.86	4.77
8.52	0.362	16.67	1.90	24.16	5.55
10.73	0.544	17.92	2.36	25.49	6.58
12.06	0.846	19.17	2.88	26.84	7.25
13.14	0.952	20.38	3.40	28.23	7.62
14.27	1.28	21.59	4.17	29.66	8.41

Series 4

T/K	C_p/J·K^{-1}·mol^{-1}	T/K	C_p/J·K^{-1}·mol^{-1}	T/K	C_p/J·K^{-1}·mol^{-1}
5.00	0.31	13.72	0.94	19.66	3.22
6.42	0.83	14.81	1.48	20.95	3.76
8.63	0.44	15.92	1.74	22.28	4.45
10.43	0.63	17.13	2.14	23.61	5.23
11.58	0.67	18.39	2.71	24.95	6.14
12.67	0.87				

Series 5

T/K	C_p/J·K^{-1}·mol^{-1}	T/K	C_p/J·K^{-1}·mol^{-1}	T/K	C_p/J·K^{-1}·mol^{-1}
28.19	7.48	51.56	27.55	77.40	52.31
29.84	8.56	53.34	29.38	79.30	54.21
31.40	10.05	55.13	31.25	81.20	55.95
32.95	11.54	56.93	32.91	83.11	57.83
34.53	12.99	58.75	34.70	85.03	59.60
36.15	14.27	60.58	36.48	86.95	61.39
37.80	14.95	62.41	38.08	88.87	63.08
39.47	16.26	64.26	39.83	90.80	64.71
41.16	17.66	66.12	41.61	92.73	66.41
42.85	19.23	67.98	43.34	94.67	68.04
44.57	20.85	69.85	45.17	96.61	69.53
46.29	22.55	71.73	46.86	98.55	71.12
48.03	24.28	73.61	48.75	100.49	72.69
49.79	25.92	75.50	50.53		

Series 6

T/K	C_p/J·K^{-1}·mol^{-1}	T/K	C_p/J·K^{-1}·mol^{-1}	T/K	C_p/J·K^{-1}·mol^{-1}
103.07	74.58	169.24	111.3	236.05	129.9
105.50	76.40	171.74	112.0	238.52	130.5
107.91	78.35	174.21	113.0	240.99	131.0
110.33	79.90	176.68	113.8	243.45	131.6
112.75	81.61	179.16	114.7	245.93	132.1
115.18	83.23	181.64	115.4	248.40	132.6
117.60	84.89	184.12	116.4	250.88	133.1
120.04	86.46	186.60	117.2	253.35	133.0
122.47	87.95	189.08	118.0	255.83	132.6
124.91	90.18	191.57	118.7	258.31	133.1
127.36	91.05	194.05	119.5	260.78	133.6
129.80	92.39	196.53	120.2	263.26	134.1
132.25	93.77	199.00	121.0	265.73	134.5
134.70	95.17	201.47	121.8	268.21	135.0
137.16	96.41	203.94	122.6	270.68	135.4
139.61	97.75	206.41	123.0	273.15	135.8
142.07	98.89	208.88	123.6	275.62	136.2
144.53	100.3	211.35	124.1	278.10	136.7
146.99	101.5	213.82	124.7	280.57	137.1
149.45	102.7	216.29	125.2	283.05	137.6
151.92	103.7	218.76	125.9	285.53	137.9
154.39	105.0	221.23	126.3	288.01	138.3
156.86	106.0	223.70	127.0	290.49	138.8
159.33	107.1	226.17	127.5	292.97	139.1
161.80	108.1	228.64	128.1	295.45	139.2
164.27	109.2	231.11	128.7	297.94	139.1
166.74	110.6	233.58	129.4	300.43	139.2

Series 7

T/K	C_p/J·K^{-1}·mol^{-1}	T/K	C_p/J·K^{-1}·mol^{-1}	T/K	C_p/J·K^{-1}·mol^{-1}
276.77	136.0	318.91	140.9	361.26	144.1
279.26	136.6	321.39	141.0	363.76	144.3
281.74	136.5	323.87	141.4	366.27	144.3
284.22	137.2	326.36	141.5	368.78	144.3
286.70	137.6	328.85	141.8	371.28	144.3
289.17	138.2	331.34	141.9	373.79	144.8
291.65	138.6	333.82	142.0	376.30	145.0
294.13	138.8	336.31	142.3	378.81	144.4
296.60	138.8	338.80	142.6	381.33	144.8
299.08	139.1	341.29	142.7	383.84	145.1
301.56	139.2	343.78	142.8	386.36	145.0
304.03	139.7	346.28	143.1	388.88	145.2
306.50	140.1	348.77	143.2	391.41	145.1
308.98	140.2	351.27	143.2	393.94	145.2
311.46	140.3	353.76	143.3	396.47	145.3
313.94	140.5	356.26	143.5	398.99	145.4
316.42	140.8	358.76	143.6		

Table 2.5: **Heat capacity data of NaLaF$_4$; high temperature measurements by differential scanning heat flux calorimetry**

T/K	C_p/J·K^{-1}·mol^{-1}	T/K	C_p/J·K^{-1}·mol^{-1}	T/K	C_p/J·K^{-1}·mol^{-1}
630.5	169.4	765.5	173.7	900.4	184.1
645.7	178.6	780.6	180.1	915.4	185.9
660.5	169.7	795.6	177.3	930.5	190.6
675.7	173.4	810.5	178.3	945.5	190.1
690.6	167.0	825.5	182.4	960.5	190.9
705.5	169.1	840.5	182.8	975.5	189.3
720.5	172.6	855.5	180.6	990.5	198.8
735.6	170.7	870.5	192.4	1005.5	197.2
750.4	169.2	885.5	181.7	1020.4	211.5

smaller temperature steps around T of decomposition:

T/K	C_p/J·K^{-1}·mol^{-1}	T/K	C_p/J·K^{-1}·mol^{-1}	T/K	C_p/J·K^{-1}·mol^{-1}
1020.5	311.0	1035.5	310.0	1060.5	2159.3
1025.5	312.7	1040.5	325.4	1065.5	412.0
1020.5	311.4	1045.6	389.5	1070.5	318.7
1025.5	312.5	1050.7	625.7	1075.5	306.7
1030.5	318.2	1055.6	1261.8		

Chapter 3

Solvents

In this Chapter, an explanation is given on the why and how of thermodynamic assessments. The use of the so-called general polynomial model is clarified. This assessment section is followed by the application of it to the most common MSR solvents: $LiF\text{-}BeF_2$, $NaF\text{-}BeF_2$, $LiF\text{-}NaF$ and $NaF\text{-}ZrF_4$. The results and discussion on the $LiF\text{-}BeF_2$ and $LiF\text{-}NaF$ systems were published as parts of two papers: Van der Meer, Konings, Jacobs and Oonk, "A miscibility gap in $LiF\text{-}BeF_2$ and $LiF\text{-}BeF_2\text{-}ThF_4$", J. Nucl. Mater., **344**, p. 94, 2005 and: Van der Meer, Konings, Hack and Oonk, "Modeling and Calculation of the $LiF\text{-}NaF\text{-}MF_3$ (M=La,Ce,Pu) Phase Diagrams", Chem. Mater., **18**, p. 510, 2006.

Thermodynamic assessment of a binary system

Phase diagrams describe the phase behavior of a chemical system. They can be measured by, for example, Differential Thermal Analysis. This is a straight-forward, but time-consuming technique, especially when the systems become more complicated. It is therefore useful to calculate phase diagrams. The concept of thermodynamic modelling is to calculate diagrams using Gibbs energy data on the one hand and experimental data on whatever property that

may be useful on the other hand. Data on the phase diagram itself, on the activity of a component or on the vapor pressure are commonly used. Usually the coefficients describing the binary diagrams are optimized, which can be extrapolated to calculate ternary or multi-component diagrams.

Gibbs energy functions of all phases of the system and especially the excess Gibbs energy coefficients of the solution phases are necessary to calculate a T-X phase diagram. When they are unknown, which is rather the rule than exception, they can be obtained by performing a thermodynamic assessment. This is done by making use of the known Gibbs energy functions of the compounds and the available experimental data in the following way: The Gibbs energy functions for the relevant compounds are set up after careful investigation of thermodynamic tables [29] in such a way that they are described as the polynomial in Eq. 3.1.

$$G(T) = a + bT + cT\ln(T) + \sum d_i T^i \tag{3.1}$$

For each phase, Gibbs energy functions are defined. The Gibbs energy is derived from the temperature dependence of enthalpy and entropy, which in turn are dependent on $C_p(T)$ (Eqs. 3.2, 3.3). By convention, the reference state for the enthalpy H_{ref} equals the enthalpy of formation from the elements at T=298.15 K and p=1 bar. S^0 (298.15) is used as a reference state for the entropy at T=298.15 K and p=1 bar, but it should be kept in mind that the third law holds for the entropy, i.e. it is zero at 0 K.

$$H(T) = H_{ref} + \int_{T_{ref}}^{T} C_p \, dT \tag{3.2}$$

$$S(T) = \int_{T=0}^{T} \frac{C_p}{T} \, dT \tag{3.3}$$

$$S(T) = S^0(298.15) + \int_{298.15}^{T} \frac{C_p}{T} \, dT \tag{3.4}$$

The Gibbs energy is then obtained from the Gibbs-Helmholtz equation (Eq. 3.5):

$$G(T) = H(T) - S(T)T \tag{3.5}$$

When two pure components mix, the Gibbs energy of the mixing -or solution-phase can be described at the sum of an ideal and an excess part. The ideal

part is the weighted average of the Gibbs energy of the pure components plus an ideal mixing term, defined as in Eq. 3.6:

$$\Delta G_{A-B} = X_A \Delta G_A + X_B \Delta G_B + \mathrm{R}T(X_A \ln(X_A) + (X_B)\ln(X_B)) + \Delta_{\mathrm{xs}} G_{A-B}$$
(3.6)

Several models exist to describe the excess Gibbs energy of the binary solution phase. Relatively simple Redlich-Kister polynomials can be used, which are defined as in Eq. 3.7 for an $A - B$ system:

$$\Delta_{xs} G_{A-B} = X_A X_B \sum_{k=0}^{N} {}^{k}L_{A,B}(X_A - X_B)^k$$
(3.7)

${}^{k}L_{A,B}$ are the interaction coefficients, of which the temperature dependence is defined in the same way as Eq. 3.1. However, in most cases a simple linear dependence is sufficient (Eq. 3.8):

$$^{k}L_{A,B} = {}^{k}p_{A,B} + {}^{k}q_{A,B}\, T$$
(3.8)

Another model is the quasi-chemical model by Pelton and Blander [30]. This treats a binary system in which symmetry group numbers i and j are attributed to the components A and B, allowing 'i' and 'j' particles to mix substitutionally on a quasi-lattice. In this formalism, general polynomials can be used as well to describe the excess Gibbs energy coefficients. The equation for a binary system $A - B$ is given in Eq. 3.9.

$$\Delta_{xs} G = \sum_{p,q} L_{A,B}^{p,q}(T) Y_A \left(\frac{\chi_i}{\chi_i + \chi_j}\right)^p Y_B \left(\frac{\chi_j}{\chi_i + \chi_j}\right)^q$$
(3.9)

$L_{A,B}^{p,q}(T)$ is the excess Gibbs energy term as a function of the temperature. In this case, a linear dependence $L_{A,B}(T) = {}^{k}L_{A,B} + {}^{l}L_{A,B}T$ was chosen. Y_A and Y_B are the equivalent fractions of the components, p and q are the power coefficients of the equivalent fraction expression, while χ_i and χ_j are the sum of the equivalent fractions in the same symmetry group with i and j as indices for the group numbers. It should be marked that the ${}^{k}L_{A,B}$ and ${}^{l}L_{A,B}$ terms are mathematical parameters and cannot automatically be translated to parameters with a physical meaning, namely an excess enthalpy and entropy. It is possible to rewrite the Redlich-Kister equation for binary interactions in

the general polynomial notation if the equivalent fractions are similar to the mole fractions. The choice depends on how the binary excess equations should be extrapolated to higher order systems. The software used was powerful, but had a little drawback. To calculate chemically asymmetric ternary systems, it was only able to extrapolate equations of the general polynomial type; Redlich-Kister polynomials could only be used for symmetric systems. This will be explained in more detail in Chapter 4 *MSR Burner Fuels*.

The Redlich-Kister coefficients $^{k}p_{A,B}$ and $^{k}q_{A,B}$ or, depending on the choice, the $L_{A,B}^{p,q}(T)$ parameters, can be optimized for any binary system *A-B*. For this purpose, the optimization module of FactSage 5.3 [31] is used, which makes use of the Bayesian optimization algorithm. This is a genetic algorithm, based on the estimation of a probability distribution function. A given experimental data set and initial estimates are used to generate new candidate solutions [32] in such a way that an optimum fit between the Gibbs energy functions and the experimental values is obtained. The LiF-BeF$_2$ system has also been assessed using the BINGSS program [33] that makes use of the least square method to get a best fit between the experimental data and optimized Gibbs energy coefficients.

LiF-BeF$_2$

The relevance of LiF-BeF$_2$

To obtain an optimum neutron balance and also to meet other important thermal and physicochemical demands for a Molten Salt Breeder Reactor, a composition of mainly LiF-BeF$_2$ has proved to be the most viable matrix for the fuel to dissolve in.

LiF-BeF$_2$ was also considered as a "weakened" analogue for MgO-SiO$_2$ and ZnO-SiO$_2$ by Goldschmidt (for example in [34] and [35]), because the size of the fluor ion (13.6 pm) and of the oxygen ion (14.0 pm) are nearly similar and the charge is reduced from minus 2 to minus 1. Since melting temperatures for the fluorides are significantly lower than for the silicates, thermal and calorimetric investigation of the former was technically easier to perform, particularly in the past.

For these reasons, the LiF-BeF$_2$ phase diagram has been investigated by sev-

eral researchers, for example Thilo and Lehmann [34], Roy *et al.* [36, 37], Novoselova *et al.* [38], Thoma *et al.* [39] and Romberger *et al.* [40]. However, disagreements exist between the results, especially on the BeF$_2$-rich side, probably because of the experimental difficulties to perform measurements on the highly viscous melt. Molten BeF$_2$ is, as SiO$_2$, known to form glass easily. Glass-formation in a melt results inevitably in supercooling effects during thermal analysis, which in the early days was mainly based on cooling curves. An example of a heating and a cooling curve is shown as a signal versus temperature plot in Figure 3.1. In this case, a sample of a LiF-NaF-CeF$_3$ mixture was measured, which is not particularly known as a glass-former. Three thermal events could be distinguished, interpreted as the eutectic, peritectic and liquidus. It can be seen that the peaks during cooling, are at lower temperatures than the corresponding peaks during heating. A difference of some tens of degrees is common, even when the heating and cooling rate are the same.

A miscibility gap in LiF-BeF$_2$

The data on the standard enthalpy of formation, the standard entropy and the heat capacity function of the pure components LiF, BeF$_2$ and the intermediate compound Li$_2$BeF$_4$, which were used for the thermodynamic assessment, are found in Tables 3.2 and 3.3. The optimized excess Gibbs coefficients are found in Table 3.4. The calculated phase diagram is presented in Figure 3.2.

The calculated phase diagram of the LiF-BeF$_2$ system reproduces the diagram that is proposed on the basis of the experimental results, as for example by Thoma *et al.* [39], but for one exception. The calculated diagram shows a miscibility gap in the BeF$_2$ rich side. Assessments using FactSage and BINGSS gave comparable results. There was no other way to perform a successful parameter optimization than to allow a miscibility gap in the liquid phase, in order to let the entropy of fusion of BeF$_2$ be in concordance with the experimental liquidus data. The entropy of fusion of the bounding component defines the initial slope of the liquidus curve at that component in a T-X diagram [41]:

$$\frac{\mathrm{d}T}{\mathrm{d}X} = \frac{R\ T_{fus}}{\Delta_{fus}S^0} \tag{3.10}$$

The initial slope at $X = \text{BeF}_2$ proposed by Thoma *et al.* suggests $\Delta_{fus}S^0 \simeq 17$ JK^{-1}mol^{-1} or $\Delta_{fus}H^0 \simeq 13.7$ kJmol^{-1}. The experimental value is con-
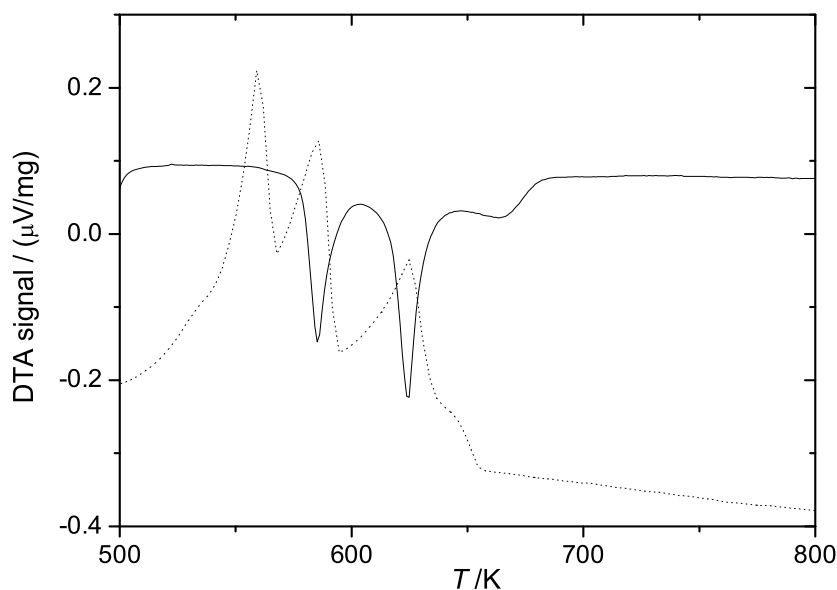
Figure 3.1: An example of a DTA heating and cooling curve.

siderably lower, $\Delta_{fus}S^0 \simeq 5.4$ JK^{-1}mol^{-1} and $\Delta_{fus}H^0 \simeq 4.5$ kJmol^{-1} and is well-established. Also Vallet and Braunstein [42] calculated a miscibility gap in the LiF-BeF$_2$ system. They used the Cook-Hilliard method [43] to compute the binodal and spinodal curves. For this method, liquidus data and extrapolated data on isothermal activity coefficients were needed, which were provided by several phase diagram measurements [39, 40] and an electromotive force study [44]. The result was a two-liquid region, which is almost entirely below the liquidus, i.e. metastable, except for a small section around the critical temperature of $T_c = 807$ K at 0.781 mole fraction. The shape of the miscibility gap is slightly different from the one calculated in our assessment process.

A miscibility gap in LiF-BeF$_2$ is also in concordance with the analogous MgO-SiO$_2$ system, which has a significant gap at the SiO$_2$ rich side, between 0.585 and 0.98 mole fraction SiO$_2$ and in the temperature range from 1968 K to 2240 K [45]. The possibility of a two liquids region in LiF-BeF$_2$ is also in agreement with findings of Thoma *et al.* [39], who published an experimental phase diagram of LiF-BeF$_2$-ZrF$_4$, with a miscibility gap in the BeF$_2$ rich corner of the ternary diagram, which nearly reaches the LiF-BeF$_2$ edge.
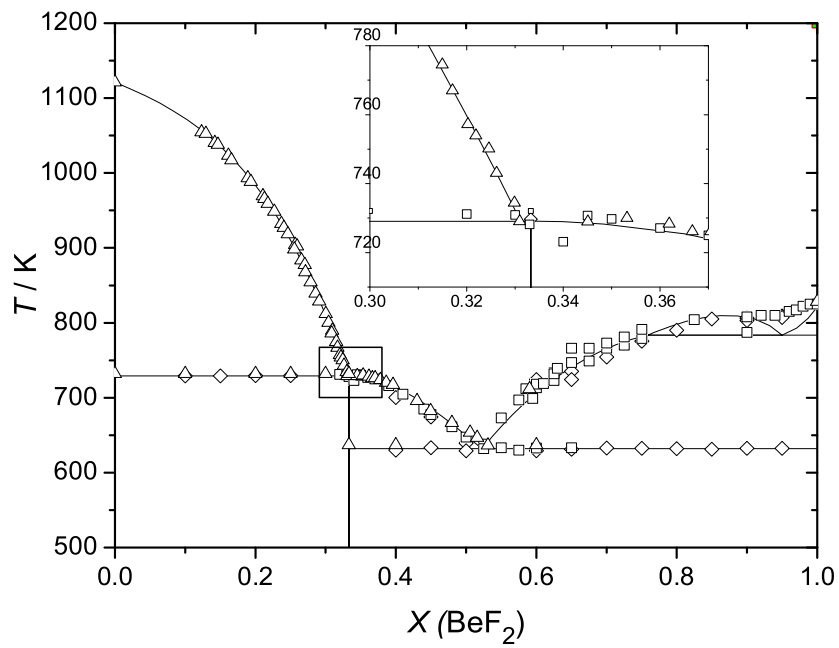
Figure 3.2: The assessed LiF-BeF$_2$ diagram, with an enlargement of the area around the congruently melting Li$_2$BeF$_4$; ◊ experimental data by Roy *et al.* [37]; □ data by Thoma *et al.* [39] and △ data by Romberger *et al.* [40]

NaF-BeF$_2$

The drawback of a ^{7}LiF-BeF$_2$ composition, is that ^{7}LiF acts as a tritium breeder, which damages the construction and structural materials of the reactor. The effect is less compared to ^{6}LiF, but still significant. Therefore, the substitution of some LiF by NaF in the solvent for Molten Salt Breeder fuel was proposed. A solvent consisting of only NaF and BeF$_2$ would be less desirable, because the cross section for neutron capture is approximately ten times higher for NaF than for ^{7}LiF [4]. Despite the fact that some interest was shown, data on the NaF-BeF$_2$ are very scarce. To our best knowledge, the most recent data stem from 1950 and are by Roy *et al.* [36], who did not list experimental data nor invariant equilibria. The suggested phase diagram was based on the work by Novoselova *et al.*(1944), as a reference in [36] and unpublished work by ORNL researchers.

The data on the standard enthalpy of formation, the standard entropy and the heat capacity function of NaF, BeF$_2$ and the intermediate compounds Na$_2$BeF$_4$ and NaBeF$_3$, which were used for the thermodynamic assessment, are found in Tables 3.2 and 3.3. It should be noted that the Gibbs energy functions of the intermediate compounds were optimized, but not the $\Delta_f H^0$ and S^0 separately, so that the given $\Delta_f H^0$ and S^0 values are arbitrary. The excess Gibbs coefficients of the liquid, which were optimized using the quasichemical model as described above, are listed in Table 3.4. The calculated phase diagram is presented in Figure 3.3.

It can be seen that the agreement with the calculated and the proposed phase diagram is reasonable. The most remarkable feature, as in LiF-BeF$_2$, is the appearance of a small miscibility gap at the BeF$_2$ side. For further investigations, more and more reliable experimental data are indispensable to create a proper model of the system.

LiF-NaF

When the MSR is designed as an actinide burner, a potential solvent is a eutectic melt of LiF and NaF, because higher solubilities can be reached for PuF$_3$ and other actinides trifluorides than in a traditional LiF-BeF$_2$ solvent [46].

The data on the standard enthalpy of formation, the standard entropy and the heat capacity function of LiF and NaF are listed in Tables 3.2 and 3.3.
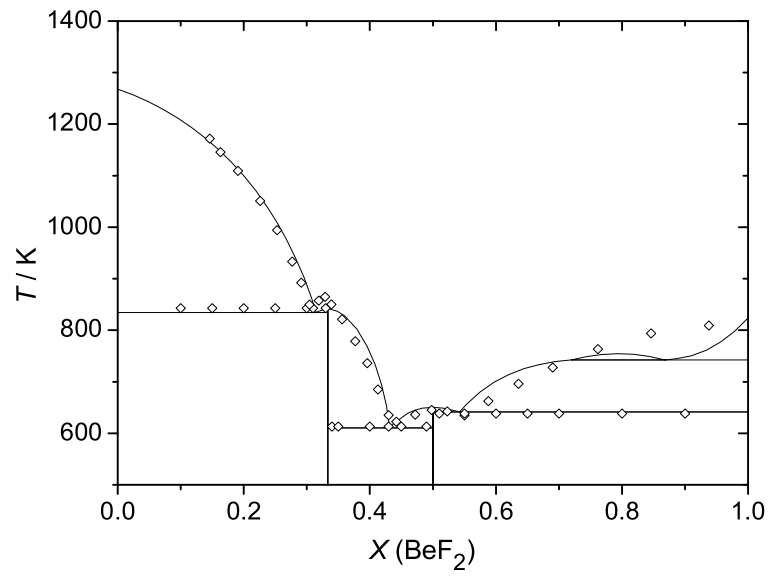
Figure 3.3: The calculated phase diagram of the NaF-BeF$_2$ system. $\Diamond$ data obtained by scanning the phase diagram as proposed by Roy *et al.* [36].

The optimized excess Gibbs coefficients of the liquid phase can be found in Table 3.4. The calculated phase diagram is presented in Figure 3.4. An excellent agreement was obtained between the model and the experimental data of this single eutectic system.

NaF-ZrF$_4$

NaF-ZrF$_4$ was the solvent for ARE, the Aircraft Reactor Experiment in the 1950s in Oak Ridge National Laboratory. It has also been mentioned as a solvent candidate for the Generation IV MSR. NaF-ZrF$_4$ is a complicated binary system with many intermediate compounds. It has been analyzed by Barton *et al.* [47]. Crystallographic analysis was performed by Thoma *et al.* [48], which confirmed the existence of six intermediate compounds.

We carried out Differential Thermal Analysis, using a Netzsch STA 449C Jupiter, on NaF-ZrF$_4$ samples. The molar fraction of ZrF$_4$ in the samples varied from 0.3 to 0.6. The used salts, purchased at Alfa Aesar, were NaF, with a purity grade of 99.99% and ZrF$_4$ with a grade of 99.9%, both on metal basis. Before use the salts were dried in a furnace, for 5 hours at 523 K under continuous Ar 6.0 flow. Weighed mixtures were put in boron nitride crucibles. After being closed with a screwed cap, they were transported immediately to the DTA apparatus, where the measurements were performed. More details on the technique and the interpretation can be found in Chapter 4 *MSR Burner Fuels*.

The data on the standard enthalpy of formation, the standard entropy and the heat capacity function of NaF, ZrF$_4$ and the six intermediate compounds are found in Tables 3.2 and 3.3. As for the NaF-BeF$_2$ compounds, the G functions of the intermediate compounds were optimized as well, so that the given $\Delta_\mathrm{f}H^0$ and S^0 are arbitrary. The optimized excess Gibbs coefficients of the liquid phase are found in Table 3.4. The experimental DTA data were interpreted as invariant points and phase transitions and are listed in Table 3.1. The calculated phase diagram is presented in Figure 3.5.

It can be concluded that the thermodynamic modelling and analysis on this system is preliminary. The interpretation of the thermal signals appeared to be complicated. However, a large difference was observed in the peak sizes. There were peaks that represented an -estimated- enthalpy effect of -100– -200 J·g^{-1} and peaks of significantly smaller size: between -5 and -20 J·g^{-1}. It
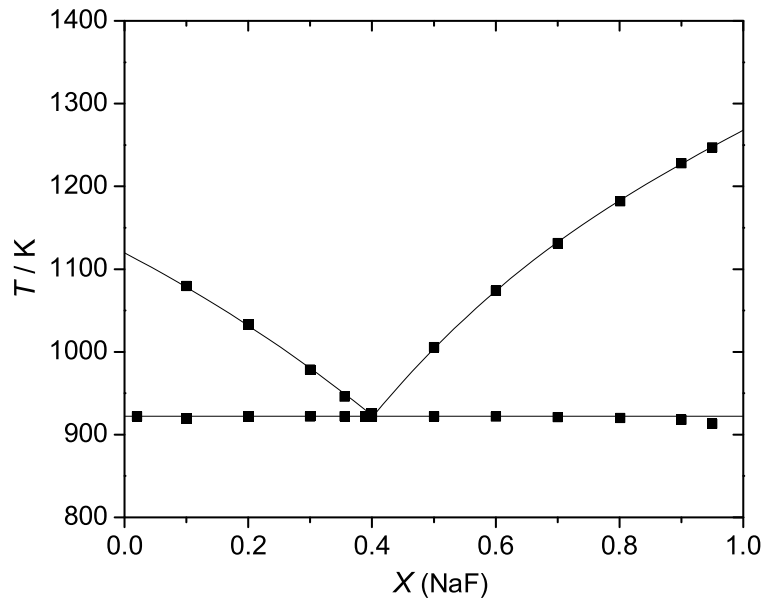
Figure 3.4: The calculated diagram of LiF-NaF with the quasi-chemical model using general polynomials. Data are from Holm and Kleppa [35].
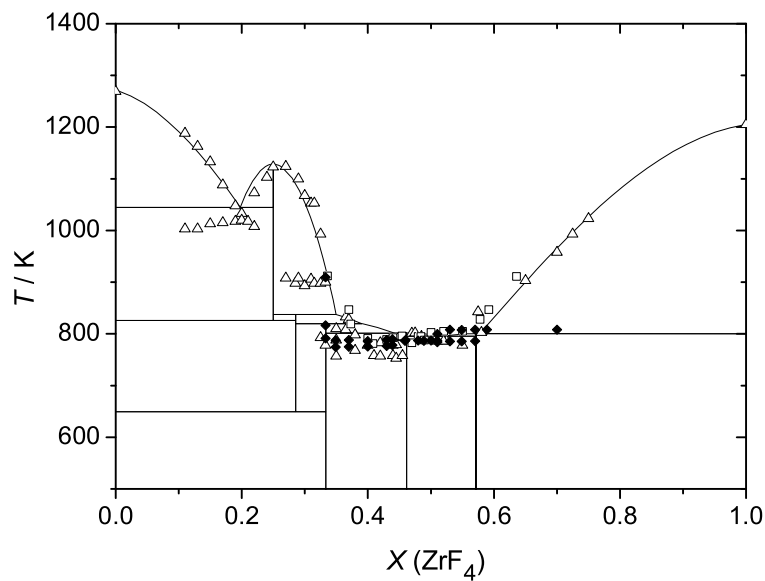
Figure 3.5: The calculated phase diagram of the NaF-ZrF$_4$ system. $\triangle$ exper-imental TA data by Barton *et al.* [47]; $\square$ DTA data by Barton *et al.*; $\blacklozenge$ our experimental DTA data.

Table 3.1: **DTA data, interpreted as invariant points and phase transitions in NaF-ZrF$_4$.**

X ZrF$_4$	T_{exp}/K	interpretation
0.333	783.9	phase transition
	791.1	phase transition
	816.7	phase transition
	909.5	incongr. mel. Na$_5$Zr$_2$F$_{13}$
0.349	774.4	eutectic Na$_2$ZrF$_6$ and Na$_7$Zr$_6$F$_{31}$
	783.5	phase transition
	787.8	phase transition
0.370	774.9	eut. Na$_2$ZrF$_6$ and Na$_7$Zr$_6$F$_{31}$
	784.3	phase transition
	788.3	phase transition
0.400	775.7	eut. Na$_2$ZrF$_6$ and Na$_7$Zr$_6$F$_{31}$
	786.1	phase transition
0.430	776.7	phase transition
	788.3	eut. Na$_7$Zr$_6$F$_{31}$ and Na$_3$Zr$_4$F$_{19}$
0.439	777.9	phase transition
	789.9	eut. Na$_7$Zr$_6$F$_{31}$ and Na$_3$Zr$_4$F$_{19}$
0.459	786.3	eut. Na$_7$Zr$_6$F$_{31}$ and Na$_3$Zr$_4$F$_{19}$
0.460	788.3	eut. Na$_7$Zr$_6$F$_{31}$ and Na$_3$Zr$_4$F$_{19}$
0.480	786.9	eut. Na$_7$Zr$_6$F$_{31}$ and Na$_3$Zr$_4$F$_{19}$
0.489	786.3	eut. Na$_7$Zr$_6$F$_{31}$ and Na$_3$Zr$_4$F$_{19}$
0.500	781.7	phase transition
	787.2	eut. Na$_7$Zr$_6$F$_{31}$ and Na$_3$Zr$_4$F$_{19}$
0.510	783.8	phase transition
	786.3	eut. Na$_7$Zr$_6$F$_{31}$ and Na$_3$Zr$_4$F$_{19}$
	799.9	phase transition
0.530	785.3	phase transition
	807.9	incongr. mel. Na$_3$Zr$_4$F$_{19}$
0.549	785.7	phase transition
	807.3	incongr. mel. Na$_3$Zr$_4$F$_{19}$
0.570	785.8	phase transition
	807.9	incongr. mel. Na$_3$Zr$_4$F$_{19}$
0.589	784.9	phase transition
	808.2	incongr. mel. Na$_3$Zr$_4$F$_{19}$
0.700	783.6	phase transition
	807.8	incongr. mel. Na$_3$Zr$_4$F$_{19}$
	906.3	phase transition

was assumed that the larger peaks represented eutectic or peritectic equilibria, while the smaller ones could be ascribed to other phase transitions.

The calculated diagram is not optimal and is therefore not publishable yet. This was, however, the best possible result with the quasi-chemical model using general polynomials. The fact that no thermodynamic data, such as enthalpy of formation and entropy, are known for the intermediate compounds does not help in the assessment. Improvements are expected when more calorimetric data are available. The application of another model, such as the quasi-chemical model in quadruplet approximation, explained in Chapter 4, could probably improve the calculated diagram.

During the DTA experiments on the $NaF-ZrF_4$ mixtures, we noticed that ZrF_4 is extremely volatile. Since the boron nitride crucibles could not be hermitically sealed, it often happened that approximately half of the sample disappeared in thin air during heating. So from our experimental experience, we realized that a 50%-50% molten $NaF-ZrF_4$ mixture is probably too volatile to use it as MSR solvent. The vapor pressure diagram, that was calculated for $T =850$, 950 and 1050 K using the Gibbs energy equations for the NaF and ZrF_4 solid and gas phases, confirms this. It can be seen that the addition of some ZrF_4, up to approximately 15%, to NaF does not affect the vapor pressure a lot. The small amount of ZrF_4 as oxygen getter in the Molten Salt Reactor Experiment (see Chapter 1 *Introduction*) will therefore not cause problems. But a 50%-50% $NaF-ZrF_4$ mixture is not suitable as solvent. A comparison is made with $LiF-BeF_2$ as solvent. It was measured by Cantor *et al.* [49] that a typical MSBR fuel at $T =850$ K has a vapor pressure of 10^{-7} bar, whereas the $NaF-ZrF_4$ mixture exerts a vapor pressure of 10^{-5} bar, so hundred times higher.

Conclusion on the MSR solvents

A $^7LiF-BeF_2$ mixture was proposed as the solvent for Molten Salt Breeder fuel. The $LiF-BeF_2$ system was modelled and the calculated phase diagram is in good agreement with the experimental data. The $LiF-BeF_2$ model can now be used as a part of a higher-order model, when the fuels ThF_4 and UF_4 are included. The most remarkable feature in the model is the appearance of a small miscibility gap at the BeF_2 side. This was not experimentally confirmed, but it is conform the analogy with the $MgO-SiO_2$ system. It was concluded
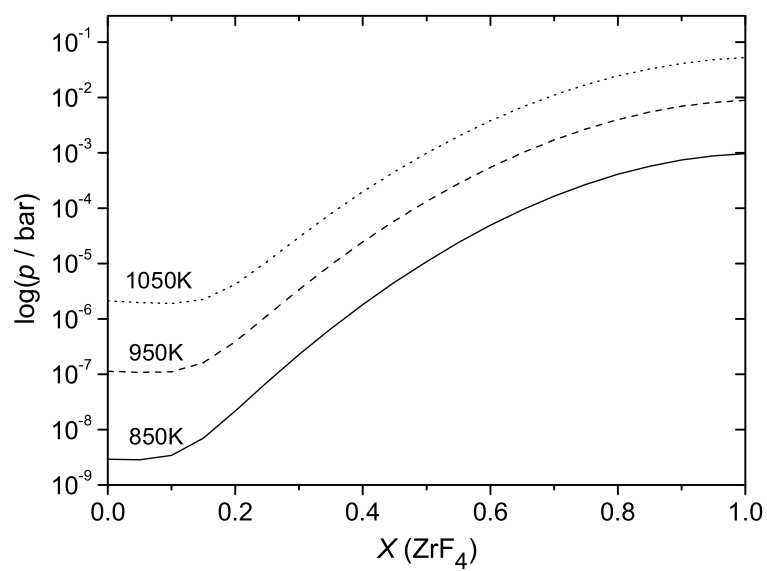
Figure 3.6: The calculated vapor pressure in the NaF-ZrF$_4$ system at $T =$850, 950 and 1050 K.

that the entropy of fusion of BeF_2 "forces" the system to have a small region of demixing. However, this little gap has no influence on the solvent composition.

It was also proposed to substitute some ^7LiF by NaF to avoid excessive tritium breeding. The $NaF-BeF_2$ system is not well-known. It has been assessed, but the results are not confirmed by reliable experiments and will therefore not be included in further modelling.

A LiF-NaF eutectic mixture is the candidate for fuel for the MSR waste burner option. LiF-NaF was modelled and an excellent fit with the experimental data was obtained. This system is further investigated when actinide fluorides are added in Chapter 4 *MSR Burner Fuels*.

DTA experiments were performed on $NaF-ZrF_4$, which was also thermodynamically modelled. The solvent for the ARE project, a 50%-50% $NaF-ZrF_4$ mixture, appears to be extremely volatile and therefore not suitable for an operating reactor. However, the addition of small amounts of ZrF_4 as an oxygen getter would be harmless.

Gibbs energy tables

The data in Tables 3.2 and 3.3 are extracted from the NIST-JANAF Thermochemical Tables [29], if not indicated as otherwise.

Table 3.2: $\Delta_f H^0$(**298.15 K**) and S^0(**298.15 K**) **for the pure components and intermediate compounds mentioned in this Chapter** *Solvents*

Comp.	$\Delta_f H^0$(298.15 K)	S^0(298.15 K)
	/kJ·mol^{-1}	/J·K^{-1}·mol^{-1}
LiF (l)	-598.654	42.962
BeF$_2$ (l)	-1021.658	60.495
NaF (l)	-557.730	52.755
ZrF$_4$ (l)	-1836.270	173.915
LiF (cr)	-616.931	35.660
BeF$_2$ (cr,α)^a	-1026.800	53.354
BeF$_2$ (cr,β)^a	-1025.795	55.645
NaF (cr)	-576.650	51.210
ZrF$_4$ (cr)	-1911.300	104.7
LiF (g)	-598.654	42.962
BeF$_2$ (g)	-1021.658	60.495
NaF (g)	-290.453	217.610
ZrF$_4$ (g)	-1673.000	319.516
Li$_2$F$_2$ (g)	-942.781	258.627
Li$_2$BeF$_4$ (g)^b	-1958.200	324.449
LiBeF$_3$ (g)^b	-1390.300	292.583
Li$_2$BeF$_4$ (cr)	-2274.254	129.483
Na$_2$BeF$_4$ (cr)^c	-2185.555	167.470
NaBeF$_3$ (cr)^c	-1609.846	107.994
Na$_3$ZrF$_7$ (cr)^c	-3540.872	428.298
Na$_5$Zr$_2$F$_{13}$ (cr)^c	-6761.816	494.263
Na$_2$ZrF$_6$ (cr)^c	-3104.644	202.817
Na$_7$Zr$_6$F$_{31}$ (cr)^c	-15670. 820	986.019
Na$_3$Zr$_4$F$_{19}$ (cr)^c	-9475.635	545.951

^{a} A transition from low quartz to high quartz occurs at 500 K.

^{b} Derived from Büchler and Stauffer [50].

^{c} Obtained by assessment with the quasi-chemical general polynomial model.

Table 3.3: C_p **data for the pure components and intermediate compounds mentioned in this Chapter** *Solvents*

Comp.	a T^{-2} /K^{-2}	b T^{-1} /K^{-1}	c	d T /K	e T^2 /K^2	f T^3 /K^3
LiF (l)^a			64.183			
BeF$_2$ (l)^a			0.984	4.4936E-2		
NaF (l)			72.989			
ZrF$_4$ (l)			123.60			
LiF (cr)^a	-5.6912E+5		43.309	1.6312E-2	5.0470E-7	
BeF$_2$ (cr,α)^b			19.181	1.0954E-1		
BeF$_2$ (cr,β)^b			39.457	4.6255E-2		
NaF (cr)	-4.6430E+5		47.630	1.4790E-2		
ZrF$_4$ (cr)	1.6005E+6		115.613	2.0500E-2		
LiF (g)^a	-2.6573E+5		32.312	7.5126E-3	-3.2485E-6	5.0097E-10
BeF$_2$ (g)^a	-5.2161E+5		47.300	1.8946E-2	-8.4383E-6	1.259E-9
NaF (g)	-2.6656E+5		36.882	1.1426E-3	-9.9703E-8	
ZrF$_4$ (g)		-9.3522E+3	121.112	-8.7222E-3	2.7543E-6	-3.2832E-10
Li$_2$F$_2$ (g)	-1.5149E+6		79.206	3.4702E-3	-7.6415E-7	
Li$_2$BeF$_4$ (g)^c		-1.9785E+4	173.425	-3.1121E-3	-1.0006E-6	3.2171E-10
LiBeF$_3$ (g)^c		-1.1441E+4	113.201	2.9946E-3	-2.7011E-6	5.0080E-10
Li$_2$BeF$_4$ (cr)^d	1.9708E+5		90.779	1.4915E-1	-1.8416E-8	
Na$_2$BeF$_4$ (cr)^d	3.6357E+5		89.786	1.5427E-1	-1.8416E-8	
NaBeF$_3$ (cr)^d	1.8083E+5		53.895	1.2808E-1		
Na$_3$ZrF$_7$ (cr)^d	4.3732E+5		243.276	8.0142E-2		
Na$_5$Zr$_2$F$_{13}$ (cr)^d	1.2624E+6		443.998	1.4040E-1		
Na$_2$ZrF$_6$ (cr)^d	8.2505E+5		200.722	6.0261E-1		
Na$_7$Zr$_6$F$_{31}$ (cr)^d	6.8890E+6		991.558	2.6216E-1		
Na$_3$Zr$_4$F$_{19}$ (cr)^d	5.2389+6		590.115	1.4164E-1		

[a] Data taken from an internal report [17].

[b] A transition from low quartz to high quartz occurs at 500 K .

[c] Derived from molecular structure studies by Snelson *et al.* [51] and Cyvin and Cyvin [52].

[d] Obtained by assessment with the quasi-chemical general polynomial model.

Table 3.4: **Optimized excess Gibbs parameters of the liquid phase for the binaries mentioned in this Chapter** *Solvents*

$A - B$	p	q	$^{k}L_{A,B}$/J·mol^{-1}	$^{l}L_{A,B}$/J·K^{-1}·mol^{-1}
BeF$_2$-LiF	0	0	-15580	-11.645
	1	0	71320	-63.487
	0	1	-71320	63.487
	1	1	-9612.0	0.000
	2	1	4806.0	0.000
	1	2	4806.0	0.000
BeF$_2$-NaF	0	0	-7789.0	2.0695
	1	0	7513.0	-21.619
	0	1	-86398	97.186
	1	1	-5121.0	1.3571
	2	1	10050	0.59481
	1	2	-49636	0.91539
NaF-LiF	0	0	-5468.2	1.5505
	0	1	5133.2	-6.9989
ZrF$_4$-NaF	0	0	-32622	-13.206
	0	1	-17891	-41.833
	1	0	-44230	-22.622

Chapter 4

MSR Burner Fuels

The composition of MSR Burner fuel

When the MSR is designed as waste burner, most of the actinides will occur as trivalent fluoride species, for which a LiF-NaF mixture is an excellent solvent. Therefore, LiF-NaF-MF$_3$ systems, with M as plutonium, americium or other actinides, are interesting. In this study, experiments were carried out for the chemical analogue for actinides: lanthanides. The ternary systems LiF-NaF-LaF$_3$ and LiF-NaF-CeF$_3$ have been experimentally analyzed and thermodynamically assessed. Two models were used and compared to describe the excess Gibbs terms of the binary subsystems. One was a regular simple quasi-chemical model with polynomial description of the excess terms, the other a modified quasi-chemical model in the quadruplet approximation. In both cases, a fine agreement with the experimental data was achieved, after asymmetrical extrapolation from the binary to the ternary systems. The binary systems of the related actinide system LiF-NaF-PuF$_3$ were assessed making use of experimental data known from the literature. The lanthanide systems served as a proxy for LiF-NaF-PuF$_3$ to calculate the ternary phase diagram. The eutectic temperature in the LiF-NaF-PuF$_3$ system is probably too high for an operating reactor. Therefore, the effect of adding the tempera-

ture lowering component RbF was investigated. The section on LiF-NaF-MF$_3$ (M=La,Ce,Pu) was mainly published as: Van der Meer, Konings, Hack and Oonk, "Modeling and Calculation of the LiF-NaF-MF$_3$ (M=La,Ce,Pu) Phase Diagrams", Chem. Mater., **18**, p. 510, 2006. The contents of the section, in which the addition of RbF is investigated, was submitted as Beneš, Van der Meer and Konings, "Modelling and calculation of the phase diagrams of the LiF-NaF-RbF-LaF$_3$ system" to the Calphad journal.

LiF-NaF-MF$_3$ (M=La,Ce,Pu)

In this study we first performed thermodynamic assessments on binary subsystems of LiF-NaF-LaF$_3$ and LiF-NaF-CeF$_3$. Excess Gibbs energy terms were optimized according to a general polynomial description, as is described in the *Solvents* Chapter. The system LiF-NaF-LaF$_3$ was also assessed using the modified quasi-chemical model in the quadruplet approximation proposed by Pelton and Chartrand [53, 54]. For the optimization, our own experimental DTA data and data found in the literature were used. After extrapolation according to the Kohler-Toop model [55], the ternary diagrams were calculated. The results were compared to our own experimental data for the ternary systems. Using the two lanthanide analogues as a proxy, the LiF-NaF-PuF$_3$ diagram, which was calculated in a similar way from the known binaries, is presented.

Differential Thermal Analysis

The thermal analysis on the salt samples was performed with Differential Thermal Analysis, using a Netzsch STA 449C Jupiter, see Figure 4.1. Since fluoride salts are hygroscopic, sample preparation and measurements were carried out in an inert argon atmosphere. LiF 99.98%, NaF 99.99% (on metals basis) and LaF$_3$ 99.99% (REO), all from Alfa Aesar were used. Before use the salts were dried in a furnace, for 5 hours at 523 K under continuous Ar 6.0 flow. Weighed mixtures were put in boron nitride crucibles. A picture of these is shown in Figure 4.2. After being closed with a screwed cap, they were transported immediately to the DTA apparatus, where the measurements were performed.

All the samples underwent two heating cycles. The first had to be discarded,

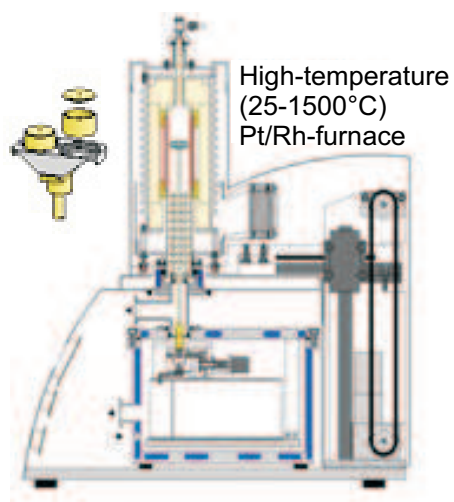High-temperature
(25-1500°C)
Pt/Rh-furnace

Figure 4.1: Netzsch STA 449C Jupiter.

Figure 4.2: Boron crucibles as used in the DTA experiments. The height is

8 mm, the outer diameter is 6.5 mm.

because it was assumed that mixing had not been complete yet. Only the heating curves from the second cycle were analyzed. Onset temperatures were taken for the determination of eutectic and peritectic temperatures. However, for the determination of the liquidus, the endset temperature [56] was selected. This was done for the following reason. In contrast to an isothermal effect, which gives a clearly defined signal, a liquidus peak has a different character. When increasing temperature for a certain composition, the amount of liquid phase present increases gradually, till the moment when the last solid crystal disappears. That moment is usually marked by a little cusp in the DTA spectrum. Moreover, taking the endset point as the temperature at which the melting process is complete, is also in accordance with the definition of a liquidus. This assumes that the liquidus temperature is the lowest temperature at a specified composition, above which only the liquid phase is present.

Table 4.2 lists the results of the DSC experiments on binary mixtures of LiF-LaF$_3$, LiF-CeF$_3$, NaF-LaF$_3$ and NaF-CeF$_3$.

The quasi-chemical model in quadruplet approximation

For the quasi-chemical model in quadruplet approximation, first-nearest and second-nearest neighbor short-range ordering in the liquid phase are considered at the same time [53]. It is assumed that the solution consists of two sublattices. This implies, for a AX-BY molten salt, that the cations, which are A and B, are allocated to sublattice I, while the anions X and Y belong to sublattice II. The following exchange reaction is considered:

$$(A \cdots X) + (B \cdots Y) = (A \cdots Y) + (B \cdots X) \qquad \Delta g_{AB/XY}^{exchange} \qquad (4.1)$$
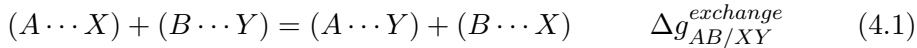
It should be noted that each quadruplet consists of two cations and two anions, where the cation-anion pair produces a first-nearest neighbor (FNN) interaction, while the cation-cation and the anion-anion pairs exert second-nearest neighbor (SNN) interactions. Since the only anion involved in this study is F$^-$, the quadruplet approximation is in principle reduced to the so-called pair approximation with two sublattices [57]. However, the quadruplet notation is kept here. The excess Gibbs energy can be expressed as SNN interaction terms $\Delta g_{AB/X_2}$ and can be expanded as a polynomial:

$$\Delta g_{AB/X_2} = \Delta g^0_{AB/X_2} + \sum_{(i+j)\geqq 1} \chi^i_{AB/X_2} \chi^j_{BA/X_2} g^{ij}_{AB/X} \qquad (4.2)$$

where χ^i_{AB/X_2} and χ^j_{BA/X_2} are the ratios of the summation of symmetric and the summation of asymmetric cation-cation, respectively anion-anion pairs mole fractions.

Thermodynamic assessment of the binary subsystems of LiF-NaF-MF$_3$

FactSage 5.3 [31] was used to obtain optimized values for the interaction co-efficients in the polynomial approach, as explained in the *Solvents* Chapter, for the quadruplet approach as well as for unknown parameters in the Gibbs energy equations of intermediate compounds, in a way that they were in best agreement with both the known theoretical Gibbs energy equations and the experimental data. The OptiSage module from FactSage uses the Bayesian Optimization Algorithm [32]. Its concept is based on the estimation of a probability distribution function, given an experimental data set and prior solutions, to generate new candidate solutions.

The standard enthalpy of formation, the standard entropy and the heat capacity functions of the pure components and the intermediate compounds in the LiF-NaF-MF$_3$ systems that were used in the thermodynamic assessment are listed in Tables 4.10 and 4.11 in the section *Gibbs energy data tables*.
The optimized excess Gibbs parameters of the liquid phase for LiF-NaF, LiF-MF$_3$ and NaF-MF$_3$, as obtained by the polynomial model, are tabulated in Table 4.1.

The optimized excess Gibbs terms for the quasi-chemical model with quadruplets approximation are listed below. The same notation as proposed by Chartrand and Pelton [58, 59, 54] is used here.

An important input parameter in this model are the coordination numbers of the cations in the liquid. We used the same numbers as Chartrand and Pelton [58]. The default value is '6', which is subject to change when cations of different valency are involved in one quadruplet so that the electroneutrality

Table 4.1: **Optimized excess Gibbs parameters of the liquid phase for LiF-NaF, LiF-MF$_3$ and NaF-MF$_3$, by the polynomial model**

A, B	p	q	$^0L_{A,B}$ J·mol^{-1}	$^1L_{A,B}$ J·K^{-1}·mol^{-1}
NaF-LiF	0	0	-5468.2	1.5505
	0	1	5133.2	-6.9989
LaF$_3$-LiF	0	0	-30371	17.023
CeF$_3$-LiF	0	0	-33179	19.980
PuF$_3$-LiF	0	0	3809.5	-9.0628
LaF$_3$-NaF	0	0	-67708	128.27
	1	0	-10990	14.895
	0	1	9563.4	-13.882
CeF$_3$-NaF	0	0	-34066	9.2741
	0	1	-26229	-0.187
PuF$_3$-NaF	0	0	-45790	74.016
	1	0	15172	-63.492
	0	1	-49495	-10.000

in a quadruplet is guaranteed.

For a La^{3+}-F^--Na^+-F^- quadruplet, the excess Gibbs terms were found to be

$$\Delta g_{LaNa/FF} = 908.25 - 14.974\,T - 9168.3\,\chi_{LaNa} + 2936.7\,\chi_{NaLa} \quad \text{J} \cdot \text{mol}^{-1}$$
$$(4.3)$$

using coordination numbers 6 for La^{3+} and 2 for Na^+. Ditto equations were found for the other quadruplets. In the case of the Na-F-Li-F quadruplet, the cations had the coordination number 6.

$$\Delta g_{LaLi/FF} = -192.06 - 5.0976\,T + 718.44\,\chi_{LaLi} + 2138.1\,\chi_{LiLa} \quad \text{J} \cdot \text{mol}^{-1}$$
$$(4.4)$$

$$\Delta g_{NaLi/FF} = -1691.6 + 656.65\,\chi_{NaLi} + 73.930\,\chi_{LiNa} \quad \text{J} \cdot \text{mol}^{-1} \quad (4.5)$$

The binary subsystems in LiF-NaF-MF$_3$

The phase diagrams of LiF-NaF and LiF-MF$_3$ are single eutectic systems. NaF-MF$_3$ on the other hand, contains an intermediate compound NaMF$_4$, which melts incongruently.

Different sets of experimental data exists for LiF-LaF$_3$ [60, 61, 62, 63] and NaF-LaF$_3$ [63, 23] and they show the largest variations at the LaF$_3$ rich side of the diagram. This is probably the case for the CeF$_3$ and PuF$_3$ analogues as well, but less data [64, 65, 66] are available to make a proper comparison. During the optimization, it is important to distinguish between the different experimental sets and to select the one that seems most correct. When all the sets are taken into account, unwanted curves may appear in the calculated diagram.

It appeared that the optimized excess parameters, which were obtained by only including literature data, gave an unsatisfactory result after extrapolation to the ternary system, especially for the liquidus at LaF$_3$ rich compositions. Therefore, a number of experiments on binary mixtures at the LaF$_3$ side were redone in this study as well and the results were included in the

assessment. The data are found in Table 4.2. Higher weight was given to our own experimental data to carry out the optimization of the excess parameters. This resulted consequently in a better fit with the ternary experimental data afterwards, since the experiments were performed under the same conditions and peak analysis was done in a similar way, which cannot be said from those reported in the literature.

The excess parameters of the binary systems LiF-NaF, LiF-LaF$_3$ and NaF-LaF$_3$ were optimized using both models: the polynomial and the quadruplet description. In Figures 4.3, 4.4 and 4.10, the two phase diagrams obtained by the different models are shown together. It can be seen that the differences are minor.

Table 4.3 lists all the calculated invariant equilibria in the above mentioned binary systems, giving the results for the simple quasi-chemical polynomial model as well as for the modified quasi-chemical model with quadruplets.

It can be seen in Figures 4.4 and 4.5 that the largest differences between the new experimental data and those from the literature arise in the LaF$_3$, c.q. CeF$_3$ side. This is probably caused by the difficulty to obtain a clear DSC signal at the liquidus temperature, considering the reasons given in the *Experimental* paragraph of this Chapter. However, the different series of data are consistent on their own. Care was taken to obtain a satisfying diagram, preferably in agreement with the present data, since the shapes of the binary diagrams greatly influence the ternary diagram.

Differences in the diagrams obtained by the different models exist as well, but are relatively small. The largest difference is in the NaF-LaF$_3$ system, in the way the two models for the liquid interplay with the enthalpy and entropy of formation of the intermediate compound, which is expressed as a difference in the peritectic point. Nevertheless, both diagrams appear to be reasonable fits of the available data. As it can be found in Table 4.10, the optimized values of the enthalpy of formation and entropy of the NaLaF$_4$ compound at T=298.15 K result in values for the enthalpy of formation -8.774 kJ·mol^{-1} and entropy of formation 2.675 J·K^{-1}·mol^{-1} from the pure components NaF and LaF$_3$. Although these values result from purely numerical means, it seemed that the values were realistic. They were therefore also used in the quasi-chemical model, where they provided a better result than a renewed optimization, which has been tested. However, after finalizing this study and submittance of the paper on it, calorimetric analyses were performed on NaLaF$_4$. The results were used for a reassessment of the NaF-LaF$_3$ system, that is explained in the next paragraph.

Table 4.2: **DTA data, interpreted as eutectic, peritectic and liquidus temperature, in LiF-MF$_3$ and NaF-MF$_3$, with M=La,Ce.**

Mole fraction	T_{eut}/K	T_{per}/K	T_{liq}/K
0.201 LaF$_3$/(LiF+LaF$_3$)	1043.9		1158.0
0.250 LaF$_3$/(LiF+LaF$_3$)	1035.5		1215.7
0.301 LaF$_3$/(LiF+LaF$_3$)	1027.0		1277.1
0.350 LaF$_3$/(LiF+LaF$_3$)	1027.6		1353.3
0.450 LaF$_3$/(LiF+LaF$_3$)	1040.9		1435.8
0.301 CeF$_3$/(LiF+CeF$_3$)	1022.7		1248.0
0.401 CeF$_3$/(LiF+CeF$_3$)	1022.3		1328.0
0.100 LaF$_3$/(NaF+LaF$_3$)	1013.6		1228.3
0.201 LaF$_3$/(NaF+LaF$_3$)	1014.8		1072.7
0.250 LaF$_3$/(NaF+LaF$_3$)	1014.6		1067.6
0.275 LaF$_3$/(NaF+LaF$_3$)	1015.5		
0.301 LaF$_3$/(NaF+LaF$_3$)	1014.8		1018.8
0.400 LaF$_3$/(NaF+LaF$_3$)	1010.2	1064.4	1212.1
0.449 LaF$_3$/(NaF+LaF$_3$)	1012.3	1064.2	1278.2
0.500 LaF$_3$/(NaF+LaF$_3$)	1005.6	1056.6	
0.601 LaF$_3$/(NaF+LaF$_3$)		1054.0	
0.601 LaF$_3$/(NaF+LaF$_3$)		1063.9	1558.1
0.700 LaF$_3$/(NaF+LaF$_3$)		1056.8	
0.700 LaF$_3$/(NaF+LaF$_3$)		1057.0	1652.8
0.799 LaF$_3$/(NaF+LaF$_3$)		1051.4	1688.8
0.890 LaF$_3$/(NaF+LaF$_3$)		1058.3	
0.301 CeF$_3$/(NaF+CeF$_3$)	1000.7		1052.1
0.400 CeF$_3$/(NaF+CeF$_3$)	1004.8	1098.4	1248.1

Table 4.3: **Equilibria in LiF-NaF, LiF-MF$_3$ and NaF-MF$_3$, according to the quasi-chemical model using general polynomials.** *In italics: values found for the quasi-chemical model in quadruplet approximation.*

| Equilibrium	T/K	Mole fraction
eutectic	921.9	0.394 NaF/(LiF+NaF)
eutectic	*921.4*	*0.392 NaF/(LiF+NaF)*
eutectic	1046.3	0.154 LaF$_3$/(LiF+LaF$_3$)
eutectic	*1046.9*	*0.161 LaF$_3$/(LiF+LaF$_3$)*
eutectic	1030.8	0.178 CeF$_3$/(LiF+CeF$_3$)
eutectic	1016.2	0.200 PuF$_3$/(LiF+PuF$_3$)
eutectic	1011.5	0.283 LaF$_3$/(NaF+LaF$_3$)
eutectic	*1011.5*	*0.274 LaF$_3$/(NaF+LaF$_3$)*
peritectic	1054.6	0.342 LaF$_3$/(NaF+LaF$_3$)
peritectic	*1046.2*	*0.318 LaF$_3$/(NaF+LaF$_3$)*
eutectic	1004.7	0.257 CeF$_3$/(NaF+CeF$_3$)
peritectic	1062.3	0.357 CeF$_3$/(NaF+CeF$_3$)
eutectic	1000.0	0.227 PuF$_3$/(NaF+PuF$_3$)
peritectic	1097.7	0.373 PuF$_3$/(NaF+PuF$_3$)
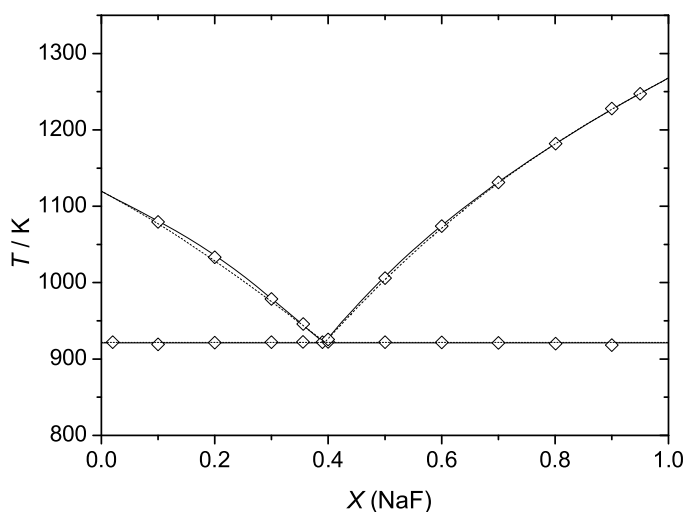
Figure 4.3: The calculated diagrams of LiF-NaF. Solid line: polynomial model;

dashed line: quadruplet model. Data are from Holm and Kleppa [35].

NaF-LaF$_3$ reassessed

The NaF-LaF$_3$ diagram was reassessed using the obtained C_p data on NaLaF$_4$. The excess Gibbs energy terms for the solution phase were optimized together with $\Delta_f H^0$(298.15 K) of NaLaF$_4$, which is still an unknown. This resulted in an excellent fit with the experimental data, but the compound is only stable above 810 K. This result is shown in Figure 4.10, where it is compared with the old diagram, which was calculated by also optimizing the complete Gibbs energy function of NaLaF$_4$ [24].

In an attempt to have the compound stable at room temperature, the standard enthalpy of formation $\Delta_f H^0$(298.15 K) was fixed in the assessment and only the excess Gibbs terms were optimized. This resulted in a diagram where the liquidus at the LaF$_3$ side became a plateau and the value of the eutectic point shifted to a temperature too low and a NaF content too high than could be justified by the experimental data. Preferred was then the diagram that gives a correct description of the liquidus and the eutectic and peritectic points, since the final goal of this study is a better understanding of the phase behavior of molten fluorides for Molten Salt Reactor applications. It has been tried to build in a couple of extra temperature terms ($T\ln T$ and/or T^2) in the
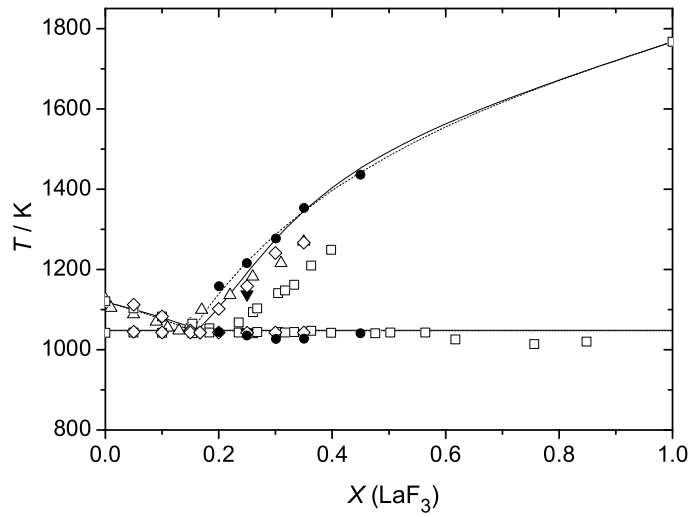
Figure 4.4: The calculated diagrams of LiF-LaF$_3$. Solid line: general polynomial model; dashed line: quadruplet model. ● our experimental data; △ Bukhalova and Babaeva [61]; □ Khripin [60]; ▼ Thoma *et al.* [62]; ◇ Agulyanskii and Bessonova [63].
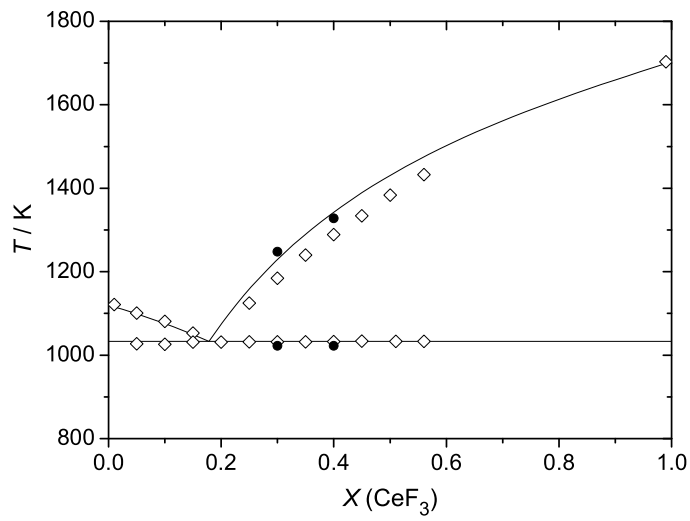
Figure 4.5: The calculated diagram of LiF-CeF$_3$. ● our experimental data; ◊
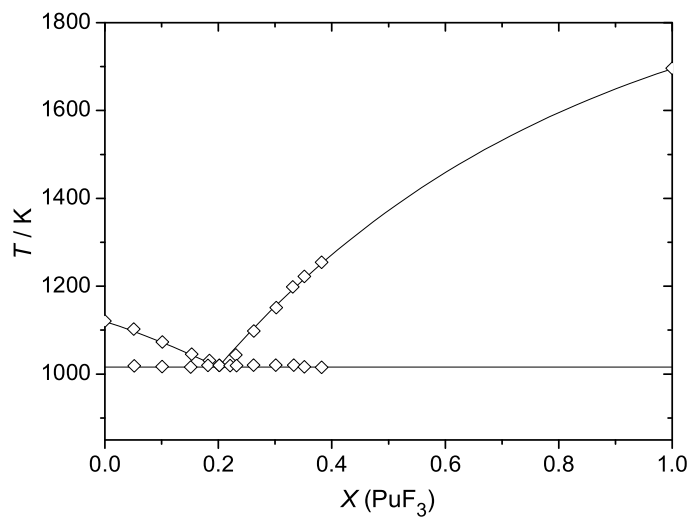
Barton *et al.* [64].

Figure 4.6: The calculated diagram of LiF-PuF$_3$. Data from Barton *et al.* [65].
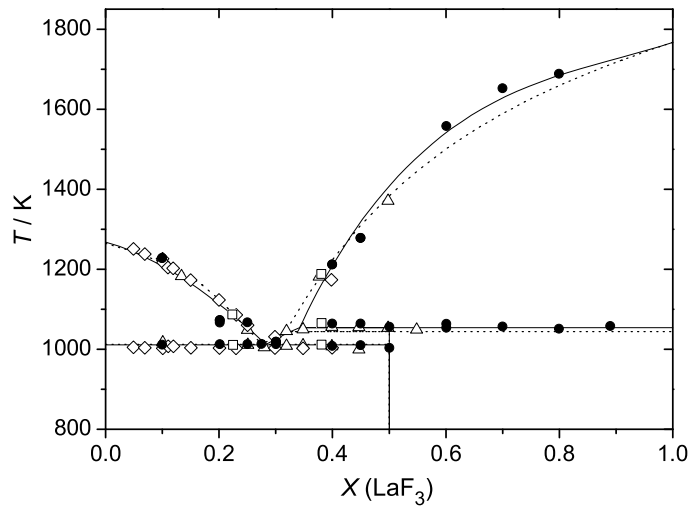
Figure 4.7: The calculated diagrams of NaF-LaF$_3$. Solid line: general poly-nomial model; dashed line: quadruplet model. ● our experimental data; △ Abdoun *et al.* [23]; ◇ Matthes and Holz [67]; □ Grande [68], the last two as a reference in [23].
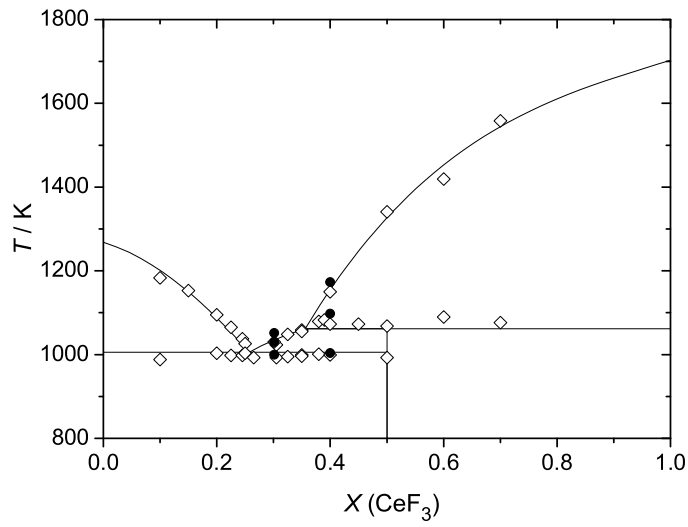
Figure 4.8: The calculated diagram of NaF-CeF$_3$. ● our experimental data; ◇
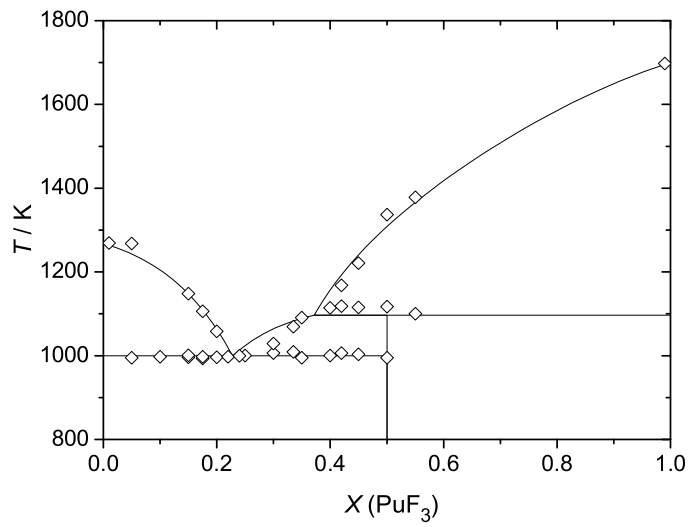
Barton *et al.* [66].

Figure 4.9: The calculated diagram of NaF-PuF$_3$. Data from Barton *et al.* [66].

description of the excess Gibbs energy of the liquid, but without the desired effect of improving the fit.

The difference between the old and the new, experimentally based diagram can be explained by the relatively large difference in the standard entropy of formation. In the old assessment, a value of $S^0(298.15 \text{ K}) = 155.5 \text{ J·K}^{-1}\text{·mol}^{-1}$ resulted from the optimization, while the measured value is $164.8 \text{ J·K}^{-1}\text{·mol}^{-1}$, as came out in this study.

The Gibbs energy of reaction for the NaLaF$_4$ compound that was taken as the difference between on the one hand the sum of $\Delta_\text{f}G^0(298.15 \text{ K})$ for NaF and LaF$_3$ and on the other hand $\Delta_\text{f}G^0(298.15 \text{ K})$ for NaLaF$_4$, which was calculated using the experimental $S^0(298.15 \text{ K})$ and the optimized $\Delta_\text{f}H^0(298.15 \text{ K})$, was $+4053 \text{ J·mol}^{-1}$. This indicates that, according to the thermodynamic model, the compound is not stable at room temperature. But this positive value is only small and it is explainable that a small discrepancy exists between the model and the experiments. It should be noted that this is an uncertainty of 0.18 % compared to the optimized $\Delta_\text{f}H^0(298.15 \text{ K})$ of 2240 kJ·mol, which is smaller than the analytical error in the low temperature heat capacity measurements (0.5%) and the error in the fit of the C_p function (0.75%). However, another possibility could be that the NaLaF$_4$ compound is a thermodynamically metastable phase at room temperature, becoming stable only at higher temperatures. To our best knowledge, no evidence exists in the literature for NaLaF$_4$ being stable or metastable at room temperature; a topic that might be studied in a future work.

However, the authors realize that improvements can possibly be achieved executing calorimetric experiments on the formation of this compound.

Calculations for ternary systems

By extrapolation of the acquired excess coefficients of the three binary subsystems LiF-NaF, LiF-MF$_3$ and NaF-MF$_3$, where M = La,Ce,Pu, the ternary system LiF-NaF-MF$_3$ was obtained. As a start, it was assumed there were no ternary interactions. The extrapolation of the excess terms was done in an asymmetrical way according to the Kohler-Toop method, since the ternary system is asymmetric, i.e. one component is chemically different from the other two. In the LiF-NaF-MF$_3$ systems, the trifluoride was selected as the asymmetric component in the extrapolation. This asymmetrical treatment of the ternary system was carried out for both the polynomial and the quadruplet

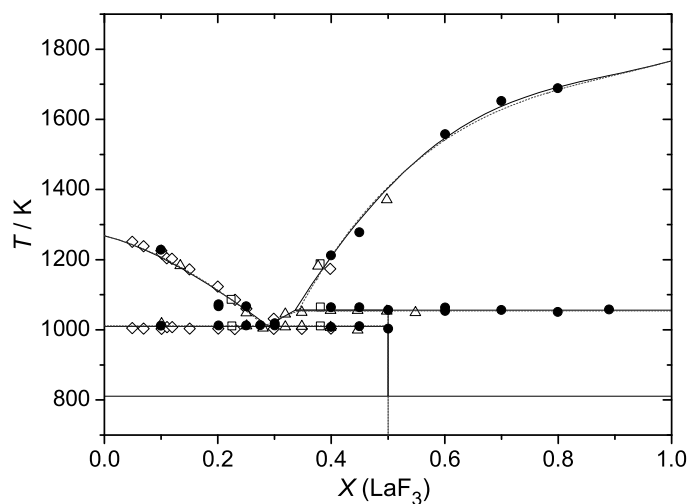Figure 4.10: The NaF-LaF$_3$ diagram reassessed with the C_p data for NaLaF$_4$.
Solid line: with C_p data used obtained by the calorimetry study as described
in Chapter 2 *Calorimetry*; dashed line: with optimized C_p data used, as men-
tioned in this Chapter. •: our experimental data [24]; △: Abdoun et al. [23];
◇: Matthes and Holz (1962); □: Grande (1992), the last two as a reference in
[23].

approach of the quasi-chemical model.

In the quasi-chemical model in quadruplet approximation it was chosen to introduce small ternary terms as in Eq. 4.2. They were included when the binary systems were expanded to a ternary. The ternary interaction terms arising from the interaction between system A-B with some C, are described in Eq. 4.6.

$$\Delta g_{AB(C)/X_2} = \sum_{i \geqq 0, j \geqq 0, k \geqq 1} \chi^i_{AB/X_2} \chi^j_{BA/X_2}$$

$$\left(\sum g^{ijk}_{AB(C)/X_2} \frac{X_{C/X}}{Y_X} (1 - \xi_{AB/X_2} - \xi_{BA/X_2})^{k-1} \right) \tag{4.6}$$

$X_{C/X}$ is a pair fraction, Y_X, as previously stated, the coordination equivalent fraction of component X and ξ_{AB/X_2}, ξ_{BA/X_2} are defined as the sums of $X_{A/X}/Y_X$, $X_{B/X}/Y_X$... as is explained in [69, 53].

Small ternary interactions terms in the quadruplet La^{3+}-F$^-$-Na$^+$-F$^-$ due to the interaction with Li were found to be

$$g^{001}_{LaNa(Li)/F} = 536.98 \quad \text{J} \cdot \text{mol}^{-1} \tag{4.7}$$

and

$$g^{011}_{LaNa(Li)/F} = -348.30 \quad \text{J} \cdot \text{mol}^{-1} \tag{4.8}$$

Idem were the the ternary interactions terms in La^{3+}-F$^-$-Li$^+$-F$^-$ with Na:

$$g^{001}_{LaLi(Na)/F} = 69.160 \quad \text{J} \cdot \text{mol}^{-1} \tag{4.9}$$

and

$$g^{011}_{LaLi(Na)/F} = 26.512 \quad \text{J} \cdot \text{mol}^{-1} \tag{4.10}$$

and in Na^{3+}-F$^-$-Li$^+$-F$^-$ with La:

$$g^{001}_{NaLi(La)/F} = 436.23 \quad \text{J} \cdot \text{mol}^{-1} \tag{4.11}$$

and

$$g^{011}_{NaLi(La)/F} = 826.85 \quad \mathrm{J \cdot mol^{-1}} \tag{4.12}$$

The ternary LiF-NaF-MF$_3$ phase diagrams

The calculated ternary diagrams of the systems LiF-NaF-LaF$_3$, LiF-NaF-CeF$_3$ and LiF-NaF-PuF$_3$, obtained after extrapolation of the excess Gibbs energy terms of the binaries, according to the polynomial model, are shown in Figures 4.11, 4.13 and 4.14. Figure 4.12 shows the LiF-NaF-LaF$_3$ diagram obtained by the quadruplet model. Table 4.4 lists all the calculated ternary invariant equilibrium points. The DTA data for the invariant equilibria are found in Table 4.5 and the experimental data for the liquidus in Table 4.6.

As it can be seen, the shapes of the diagrams are similar, which could be expected on the basis of the binary diagrams. They all have a ternary eutectic point close to the LiF-NaF axis and a ternary peritectic, which is slightly richer in LiF-MF$_3$ composition.

The experimental values of the ternary systems were compared to the results of the equilibrium calculations. For the systems LiF-NaF-LaF$_3$ and LiF-NaF-CeF$_3$, the calculations were done with the polynomial model and in case of LiF-NaF-LaF$_3$, for the quadruplet model as well. This was done by determining the precipitation temperature from the liquid phase by using the Equilib module in FactSage 5.3. The ternary data points with the accompanying experimental liquidus temperature and calculated precipitation temperature are listed in Table 4.6. The difference between the experimental liquidus temperature T_{exp} and the calculated precipitation temperature T_{calc} was normalized by T_{exp}. This deviation is plotted versus T_{exp} in Figure 4.15 for the systems LiF-NaF-LaF$_3$ and LiF-NaF-CeF$_3$.

It can be seen in Figure 4.15 that the deviation from the calculated model data with the experimental data was never exceeding $\pm$ 8%. 80% of the data fell in between $\pm$ 3% difference between experimental and theoretical values. Comparing the results for the polynomial and the quadruplet model, it is obvious that the differences between the models are random and very small. The similarity of the two models can be explained by the nature of the LiF-NaF-LaF$_3$ melt. In contrast to, for example, a LiF-BeF$_2$ melt, where BeF$_2$ acts as a chain-former, the liquid in this study has a more ionic character. Unfortunately, we do not have spectroscopic data on molten LiF-NaF-LaF$_3$.

Figure 4.11: The calculated liquid surface of LiF-NaF-LaF₃ by the polynomial model. Isotherms are labelled in K, with an interval of 25 K. ▲ Represent compositions of which experimental data are available, which can be found in Table 4.5 (invariant points) and Table 4.6 (liquidus).

Figure 4.12: As Figure 4.11, but by the modified quasi-chemical model in quadruplet approximation instead. Isotherms are labelled in K, with an interval of 25 K. ▲ The same experimental data as plotted in Figure 4.11.
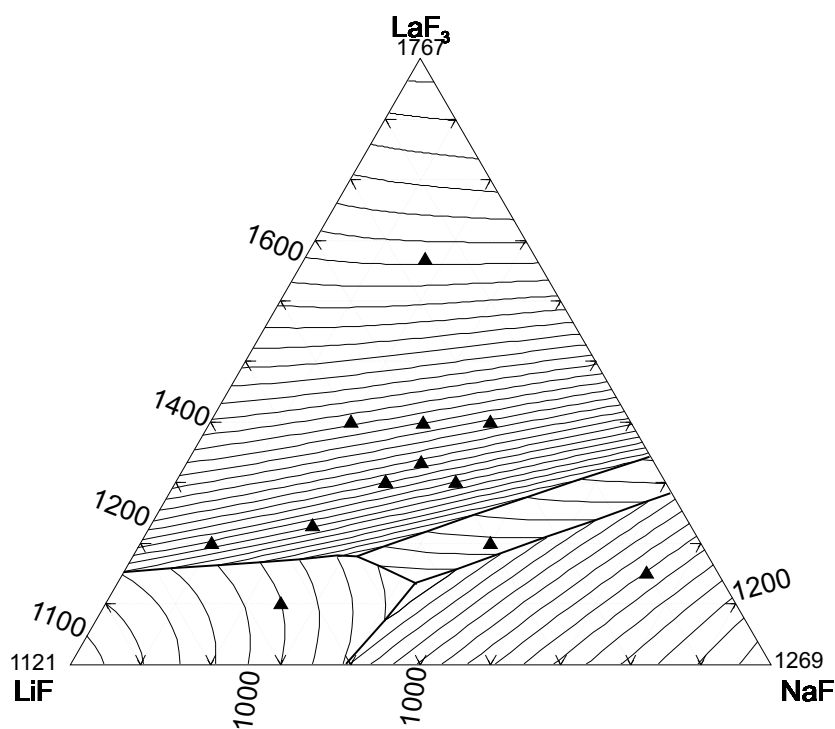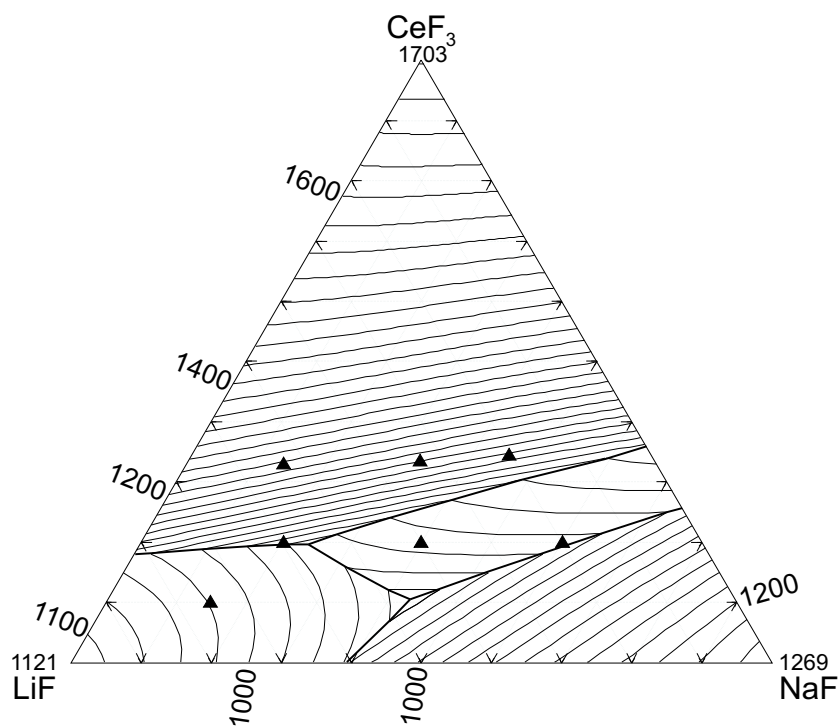
Figure 4.13: The calculated liquid surface of LiF-NaF-CeF$_3$. Isotherms are labelled in K, with an interval of 25 K. ▲ Represent compositions of which experimental data are available, which can be found in Tables 4.5 and 4.6.
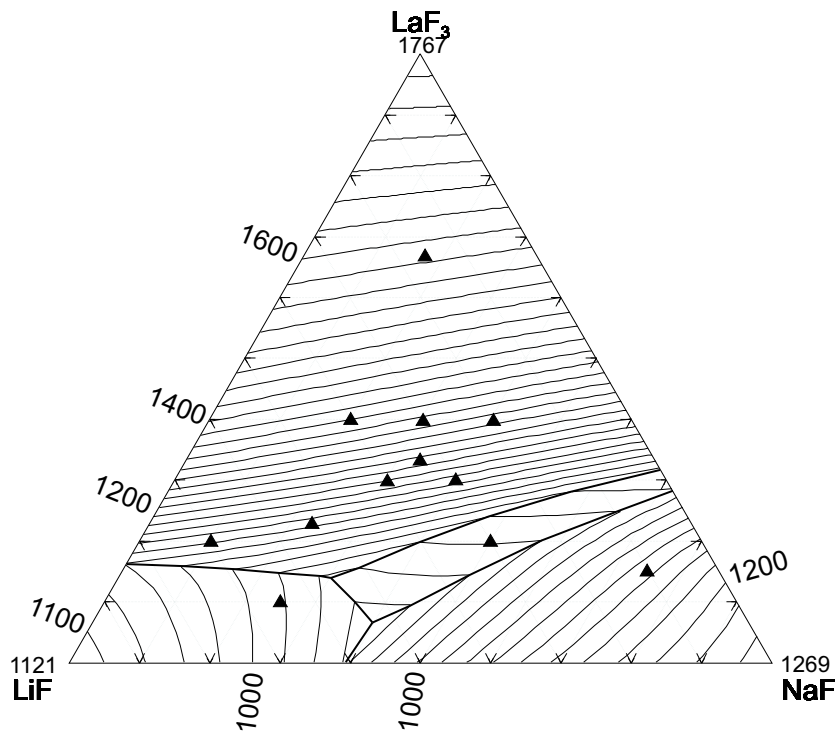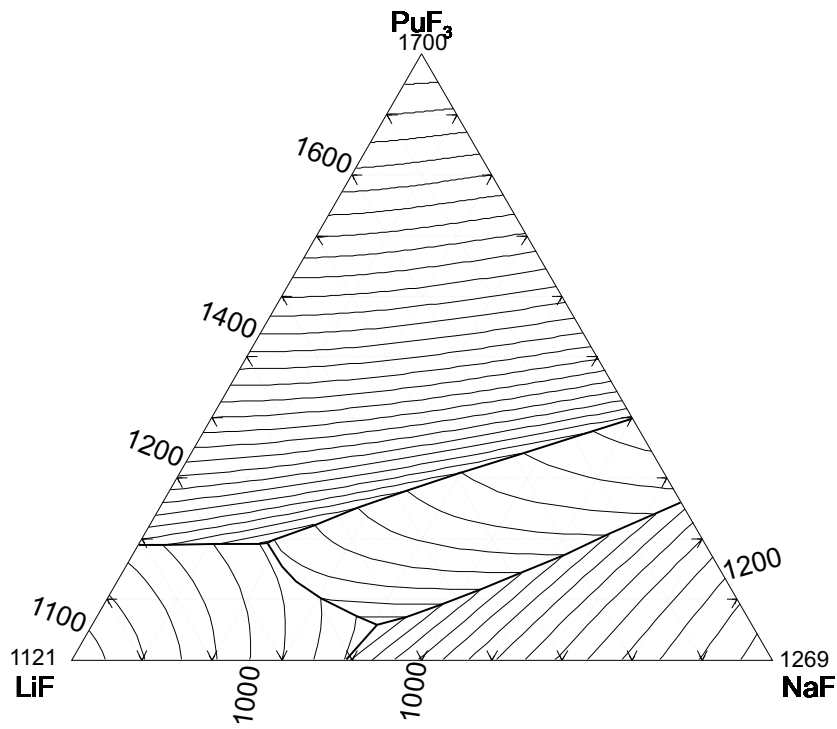
Figure 4.14: The calculated liquid surface of LiF-NaF-PuF$_3$. Isotherms are labelled in K, with an interval of 25 K.
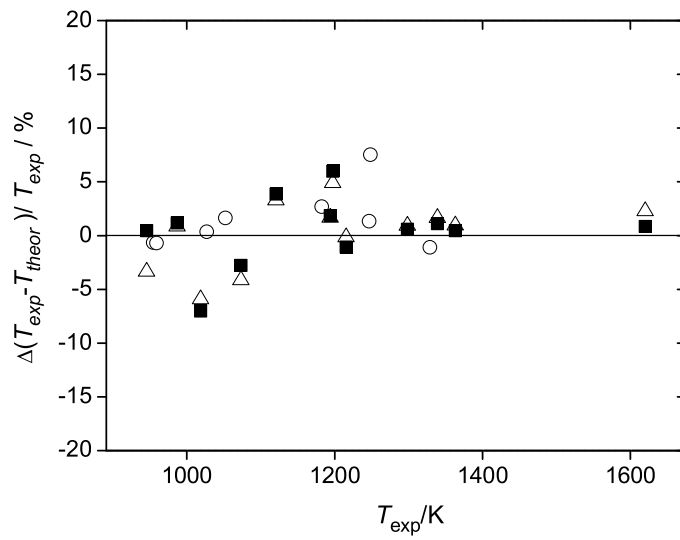
Figure 4.15: The deviation of the model precipitation temperature from the experimental liquidus temperature, normalized by the experimental temperature, as a percentage versus the experimental temperature. ■ for LiF-NaF-LaF₃ in simple quasi-chemical polynomial model; △ for LiF-NaF-LaF₃ in quasi-chemical quadruplet model; ○ for LiF-NaF-CeF₃.

Table 4.4: **Equilibria in LiF-NaF-MF$_3$.** *In italics: values found for the quasi-chemical model in quadruplet approximation.*

| M	Equilibrium	T/K	X LiF	X NaF	X MF$_3$
La	eutectic	874	0.441	0.425	0.134
	peritectic	909	0.501	0.321	0.178
La	*eutectic*	*907*	*0.534*	*0.399*	*0.067*
	peritectic	*942*	*0.558*	*0.304*	*0.138*
Ce	eutectic	884	0.465	0.430	0.105
	peritectic	936	0.561	0.243	0.196
Pu	eutectic	906	0.537	0.405	0.058
	peritectic	971	0.625	0.182	0.193

This would enable us to determine its structural characteristics and therefore to select the most appropriate thermodynamic model to describe it; an item that should be included in a future study on this system. However, Raman studies on molten LaF$_3$-KF showed that at mole fractions $X_{LaF_3} \leqq 0.25$, the La^{3+} ions are relatively shielded by the F$^-$ ions [70]. At compositions $X_{LaF_3} > 0.25$, the proposed structure of the melt is a loose network of distorted LaF$_6^{3-}$ octahedra bound by shared F$^-$ ions [71]. This implies a low tendency in this melt to form ternary complexes or chains. For melts with a stronger ordering, it is expected that the quasi-chemical model with the quadruplet approach should give the better description.

Note on the extrapolation from binary to ternary systems

The Kohler-Toop method of extrapolating excess Gibbs energy parameters from the binary subsystems to the ternary systems was applied, for the polynomial as well as for the quadruplet approach. This way of extrapolating takes different weights for the components into account, according to their chemical structure and behavior compared to the other components of the system. The method is thus suitable for chemically asymmetric systems, for which the systems studied here are an excellent example, with two univalent and one trivalent fluoride. However, in both models a comparison has been made by assigning LiF, NaF and LaF$_3$ to the same symmetry group and therefore

Table 4.5: **Experimental invariant points in LiF-NaF-LaF$_3$ and LiF-NaF-CeF$_3$.**

M	X LiF	X NaF	X MF$_3$	$T_{eut,exp}$	$T_{peri,exp}$
La	0.102	0.199	0.699	852.4	
	0.102	0.748	0.150	851.3	869.7
	0.159	0.172	0.669	849.1	862.7
	0.197	0.404	0.399	852.9	
	0.232	0.228	0.540	852.9	
	0.298	0.304	0.398	853.0	863.1
	0.299	0.400	0.301	852.9	863.5
	0.301	0.499	0.200	852.3	
	0.304	0.398	0.298	853.3	
	0.333	0.333	0.334	858.2	
	0.398	0.303	0.299	853.7	863.1
	0.398	0.303	0.299	853.1	859.7
	0.400	0.200	0.400	853.3	860.7
	0.400	0.200	0.400	852.0	
	0.400	0.301	0.299	852.2	
	0.402	0.399	0.199	854.7	
	0.499	0.401	0.100	854.3	
	0.540	0.232	0.228	851.4	856.0
	0.540	0.232	0.228	851.3	
	0.649	0.251	0.100	853.3	
	0.699	0.102	0.199	851.5	863.1
	0.699	0.102	0.199	852.6	860.9
Ce	0.199	0.601	0.200	851.9	
	0.202	0.453	0.345	864.1	
	0.334	0.332	0.334	852.1	889.9
	0.400	0.400	0.200		
	0.532	0.138	0.330	850.7	887.7
	0.597	0.203	0.200	851.9	890.4
	0.751	0.149	0.100	851.7	888.6

Table 4.6: **Experimental and calculated liquidus temperatures (in K)**
in LiF-NaF-LaF$_3$ (quasi-chemical model with general polynomials
and modified quasi-chemical model in quadruplet approximation)
and LiF-NaF-CeF$_3$ (quasi-chemical with polynomials).

M	X LiF	X NaF	X MF$_3$	$T_{liq,exp}$	$T_{liq,theor,pol}$	$T_{liq,theor,qua}$
La	0.102	0.748	0.150	1073.1.	1102.8	1117.6
	0.159	0.172	0.669	1620.0	1606.2	1583.0
	0.197	0.404	0.399	1298.2	1290.3	1286.6
	0.298	0.304	0.398	1338.8	1323.8	1317.3
	0.299	0.400	0.301	1197.5	1125.6	1138.5
	0.301	0.499	0.200	945.5	941.1	977.5
	0.333	0.333	0.334	1215.6	1228.5	1218.2
	0.400	0.200	0.400	1363.3	1357.0	1350.6
	0.398	0.303	0.299	1194.1	1171.8	1174.0
	0.540	0.232	0.228	1120.6	1077.3	1083.4
	0.649	0.251	0.100	986.8	975.2	978.3
	0.699	0.102	0.199	1018.5	1090.0	1078.3
Ce	0.199	0.601	0.200	958.8	965.4	
	0.334	0.332	0.334	1182.4	1150.5	
	0.597	0.203	0.200	954.6	960.7	
	0.751	0.149	0.100	1026.9	1023.3	

Please note that for some compositions peaks representing the eutectic and/or peritectic temperature could be detected, but not always for the liquidus temperature.

equalizing the weights. It has been found that the difference with the presented diagrams in Figures 4.11 and 4.12 is minimal, up to 10 K. It is more important that the binary diagrams give a satisfactory description, since that influences the shape of the ternary diagram much more than the way of extrapolating Gibbs energies.

In order to improve the fit with the measured and the calculated ternary eutectics in LiF-NaF-LaF$_3$ and LiF-NaF-CeF$_3$, ternary interaction terms were included in the simple quasi-chemical polynomial model, as was done for the quasi-chemical model in quadruplet approximation. However, it appeared that the agreement with the experimental data did not improve.

Implications for MSR fuel

The eutectic melt in LiF-NaF-PuF$_3$ is calculated at 906 K, its composition being 53.7 % LiF, 40.5 % NaF and 5.8 % PuF$_3$. Seen in the light of the Generation IV Molten Salt Reactor, this result implies that a eutectic mixture of LiF-NaF-PuF$_3$ is suitable as reactor fuel. Nowadays, several projects on the MSR as actinide burner are running. The TIER project [5] proposes for the fuel a composition of NaF, ZrF$_4$ and up to 3.5% actinide fluoride at an average operating temperature of 923 K. This temperature is also foreseen in the Czech SPHINX project [6], with compositions of LiF-NaF-BeF$_2$ as the solvent. However, the difference of only 17 K between the calculated melting temperature of the LiF-NaF-PuF$_3$ based fuel mixture and the designed operating temperature is probably too small, especially when computational uncertainties and the influence of other parameters related to the reactor design are taken into account. For safety reasons it might be therefore preferable to increase this margin between calculated and operating fuel temperature. This can be achieved by the addition of a melting point decreasing compound such as RbF, which we will investigate in the next section.

LiF-NaF-RbF-LaF$_3$

Since it was concluded in the former section that MSR burner fuel would probably need a melting temperature lowering compound, the effect of adding RbF was calculated. For MSR breeder fuel, adding RbF would be less suitable,

since the neutron capture cross section of Rb is large (0.7 barns to 0.010 barns for Be [4]), but a small cross section is less important for the MSR as waste burner.

The same method was applied as in the former section, namely the use of LaF_3 as an analogue for AnF_3. The model for LiF-NaF-LaF_3 was expanded with the component RbF, so that three additional binary systems had to be assessed: LiF-RbF, NaF-RbF, RbF-LaF_3. The quasi-chemical model in quadruplet approximation was used. After modelling the binaries, four ternary diagrams were calculated: LiF-NaF-LaF_3, LiF-NaF-RbF, LiF-RbF-LaF_3 and NaF-RbF-LaF_3. Some thermal experiments were performed on the binary LiF-RbF.

DTA analysis of LiF-RbF

The LiF-RbF diagram was measured with the DTA technique using the Netzsch STA 449C Jupiter, as was described in the *Experimental* section of this chapter. This system was analyzed before by Barton *et al.* in an unpublished study [72] using cooling-curve experiments and by Dergunov [73]. They found a eutectic at 56 mole % RbF and 743 K and very close to this a peritectic at 53 mole % RbF and 748 K. The system contains the intermediate compound $LiRbF_2$, of which the structure was established by Burns and Busing [74].

The interpreted data of our thermal analysis are listed in Table 4.7. Our analysis differed at some points from the previous ones. The eutectic point was almost identical and also the liquidus curve was in agreement. However, in our measurements we found a series of clear peaks over the full range below the eutectic temperature. They did not appear in the first heating and cooling cycle, but only from the second cycle on. We interpreted it as the decomposition of the intermediate compound. The compound was formed during the first heating cycle, so that no signal appeared then, but decomposed during the second cycle. We also have not found any evidence for a peritectic point, which is another argument that the compound decomposes in the solid state.

That Dergunov and Barton *et al.* came to another conclusion, could possibly be explained by the fact that they used only one heating and cooling cycle, so that they missed the signal of decomposition. The details of the experiments were not reported. It could also be possible that, in the 1950s, their equipment was not precise enough to determine these clear, but small signals. But the researchers knew there was an intermediate compound, so that they had to fit

it in the interpretation. The solution was then found in having the eutectic and peritectic very close to each other.

Assessment of the binary subsystems of LiF-NaF-RbF-LaF$_3$

The modified quasi-chemical model in quadruplet approximation [58, 59, 54], explained in the paragraph *The quasi-chemical model in quadruplet approximation*, was applied to assess the binary subsystems of LiF-NaF-RbF-LaF$_3$ containing RbF. The assessment of the LiF-RbF system was based on our experimental data and on the data by Barton *et al.* [72]. The Gibbs energy equation for the intermediate compound LiRbF$_2$, for which decomposition in the solid phase was assumed, was optimized in the assessment. The NaF-RbF diagram, a simple eutectic system, was measured by Holm [75], whose data were used in the assessment.

The RbF-LaF$_3$ system is not well known. The shape however, is very similar to the NaF-LaF$_3$ diagram, with an intermediate compound. Dergunov (1948, as a reference in Thoma [76]) found a eutectic point at 22 mole % LaF$_3$ and 855 K and a peritectic, where RbLaF$_4$ decomposes, at 38 mole % LaF$_3$ and 957 K. Optimisation of the excess Gibbs coefficients was enabled by scanning the drawn diagram that was proposed by Thoma [76] and using the data 'points'.

The equations for the RbLi/FF, RbNa/FF and RbLa/FF quadruplets were the following:

$$\Delta g_{RbLi/FF} = -4217.1 \; - \; 1442.6 \, \chi_{RbLi} \; - \; 452.22 \, \chi_{LiRb} \quad \text{J} \cdot \text{mol}^{-1} \quad (4.13)$$

$$\Delta g_{RbNa/FF} = 301.86 \; - \; 323.56 \, \chi_{RbNa} \; + \; 367.33 \, \chi_{NaRb} \quad \text{J} \cdot \text{mol}^{-1} \quad (4.14)$$

$$\Delta g_{LaRb/FF} = -14061 \; - \; 0.64743 \, T \; + \; (18281 \; - \; 47.924 \, T) \, \chi_{LaRb}$$

$$+ \, (1222.5 \; - \; 4.7935 \, T) \, \chi_{RbLa} \quad \text{J} \cdot \text{mol}^{-1} \quad (4.15)$$

Table 4.7: **DTA data, interpreted as decomposition, eutectic and liquidus in LiF-RbF.**

X RbF	T_{decom}/K	T_{eut}/K	T_{liq}/K
0.100		729.7	1079.9
0.200		746.3	956.2
0.300	686.3	746.7	933.8
0.400	688.8	746.8	861.9
0.500	688.8	747.2	752.9
0.599		745.7	
0.699	686.0	745.4	895.4
0.793	692.2	745.9	1005.1
0.894		746.6	1045.4
1.000			1070.5

As coordination number for the cations in the liquid, the default of '6' was used. In case of the La-F-Rb-F quadruplet, the coordination number for the La^{3+} cation was 6 and for Rb^+ it was 2. It is realized that rather large values are needed for the excess coefficients for the RbF-LaF$_3$ system, especially in the T-terms. However, it appeared that a satisfying result could not be reached with less or with smaller coefficients, probably also because the data on this system are very scarce.

Figures 4.16, 4.17 and 4.18 show the calculated phase diagrams of respectively LiF-RbF, NaF-RbF and RbF-LaF$_3$.

Calculation of the ternary subsystems of LiF-NaF-RbF-LaF$_3$

The ternary diagrams of LiF-NaF-RbF, LiF-RbF-LaF$_3$ and NaF-RbF-LaF$_3$ were calculated following the same method that was explained in the paragraph *Calculations for ternary systems*. LiF-NaF-RbF was considered as a chemical symmetric system, whereas LaF$_3$ was taken as the asymmetric component in the other two ternaries. In this case, no ternary interactions were introduced in the extrapolation from the binaries to the ternaries. The result is shown in Figure 4.19.
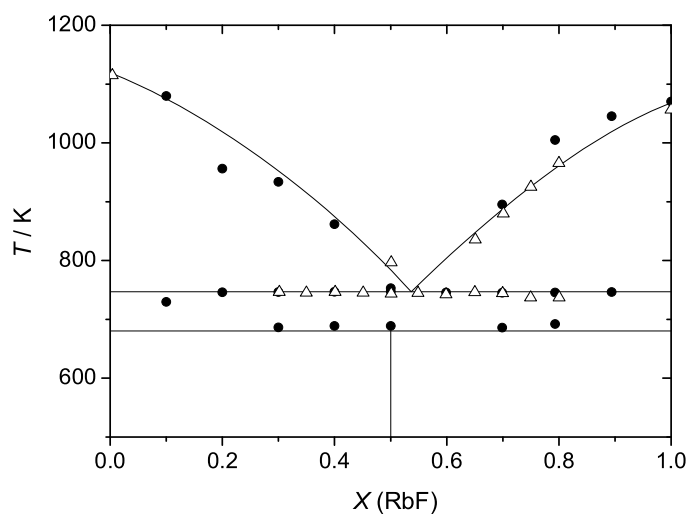
Figure 4.16: The calculated diagram of LiF-RbF. ● present experimental data;
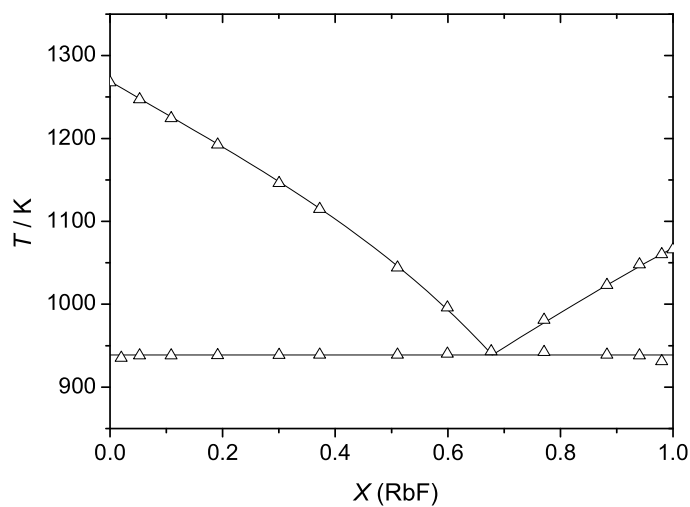
△ data by Barton *et al.* [72].

Figure 4.17: The calculated diagram of NaF-RbF. ● present experimental data;
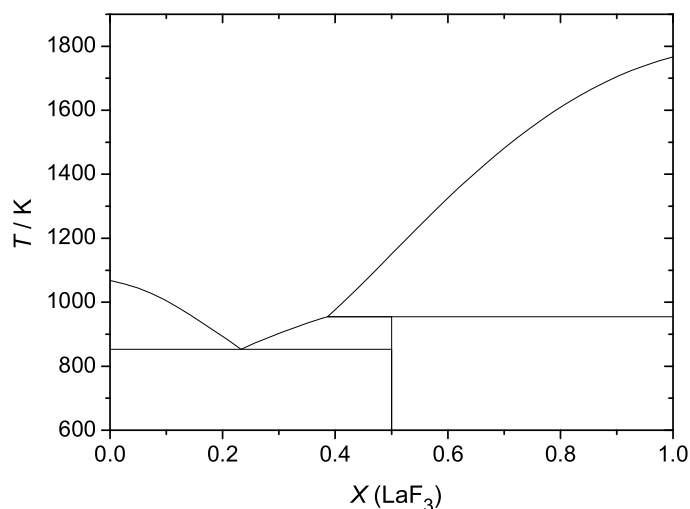
△ data by Holm [75].

Figure 4.18: The calculated diagram of RbF-LaF$_3$.

It can be seen that LiF-NaF-RbF is a simple ternary system with one eutectic. LiF-RbF-LaF$_3$ has a similar shape as LiF-NaF-LaF$_3$, namely with one eutectic and one peritectic. In the system NaF-RbF-LaF$_3$ two binary intermediate compounds are present (NaLaF$_4$ and RbLaF$_4$), leading to two peritectics in the ternary. The temperatures and compositions of the invariant equilibria are tabulated in Table 4.8.

The melting point decreasing effect by the addition of RbF to the LiF-NaF-LaF$_3$ system was investigated. The eutectic temperature and composition was calculated with the addition of respectively 5, 10 and 15 mole % RbF. The results are given in Table 4.9. It is clear that RbF has a significant lowering effect on the melting temperature, although the amount of LaF$_3$ that can be dissolved decreases a little as well.

Conclusions on LiF-NaF-RbF-MF$_3$

Thermodynamic assessments using own DTA data have been performed on the binary subsystems of LiF-NaF-LaF$_3$ and LiF-NaF-CeF$_3$. Two models were used to describe the excess Gibbs energy parameters of the system LiF-NaF-
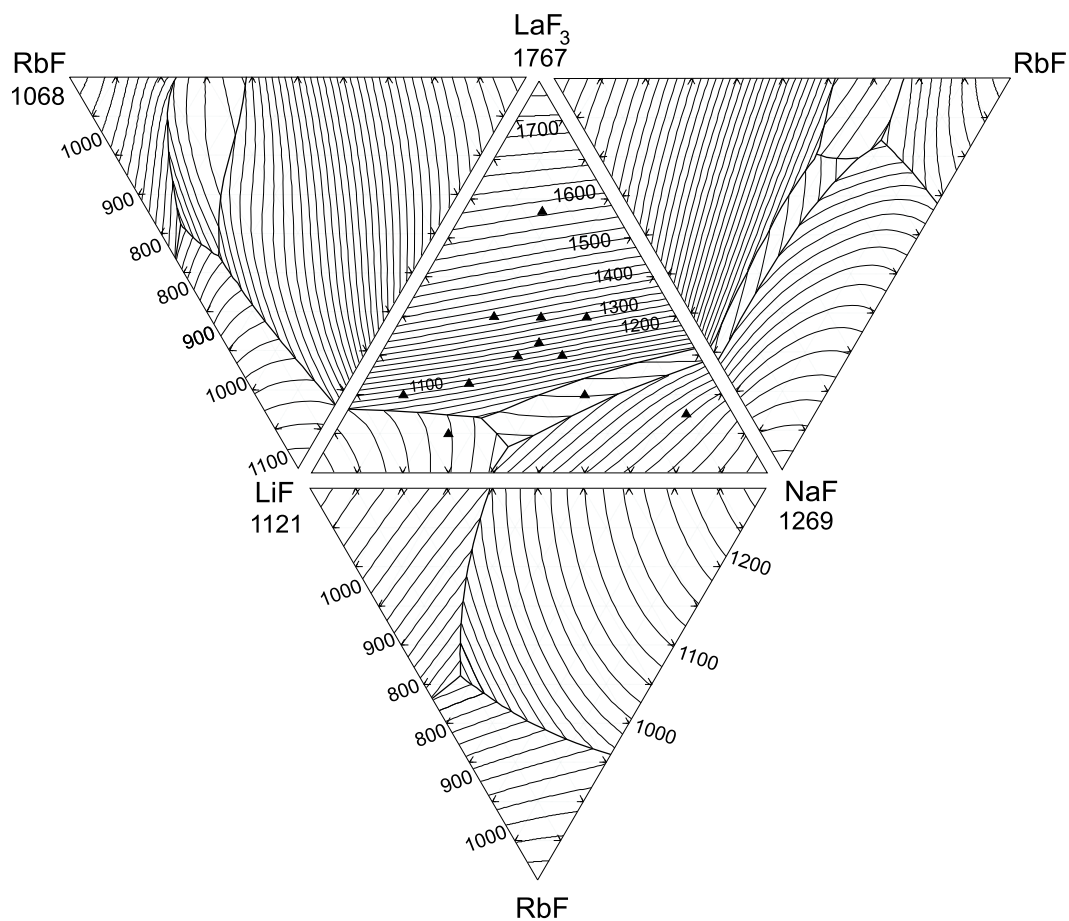
Figure 4.19: The four calculated ternary diagrams of LiF-NaF-LaF$_3$, LiF-NaF-RbF, LiF-RbF-LaF$_3$ and NaF-RbF-LaF$_3$, forming the boundaries of the quaternary system. Isotherms are shown with an interval of 25 K.

Table 4.8: **Invariant equilibria in LiF-NaF-RbF-LaF$_3$.**

equil.	phases present	T/K	X LiF	X NaF	X RbF	X LaF$_3$
eut	LiF+NaF+RbF+L	726	0.432	0.091	0.477	
eut	LiF+RbF+LaF$_3$+L	735	0.380		0.568	0.052
peri	LiF+RbLaF$_4$+LaF$_3$+L	840	0.460		0.444	0.096
eut	NaF+RbF+RbLaF$_4$+L	819		0.155	0.637	0.208
peri	NaF+NaLaF$_4$+RbLaF$_4$+L	838		0.203	0.567	0.230
peri	NaLaF$_4$+RbLaF$_4$+LaF$_3$+L	910		0.193	0.479	0.328

Table 4.9: **The effect on the eutectic temperature of LiF-NaF-LaF$_3$ by adding RbF.**

X RbF	X LiF	X NaF	X LaF$_3$	T_{eut}/K
0.000	0.534	0.399	0.067	907
0.050	0.518	0.373	0.059	886
0.100	0.506	0.339	0.055	875
0.150	0.492	0.305	0.053	864

LaF$_3$: a quasi-chemical model using general polynomials and the modified quasi-chemical model in the quadruplet approximation. The values obtained for the excess Gibbs energy parameters were extrapolated into the ternary systems according to the asymmetric Kohler-Toop model, where the trifluoride was selected as the asymmetric component. Thermal experiments on the ternaries were done as well and that showed that the agreement between calculated and experimental data was good, usually within $\pm$ 3% of the measured temperature. It also appeared that the difference between the two models is minor, which is probably due to the simple ionic nature of the melt. To describe the ternary system of LiF-NaF-PuF$_3$, which has not been measured yet, a similar method of extrapolating the optimized binary excess Gibbs energy parameters by the polynomial model was applied. The eutectic melt appeared to be at 906 K and at a composition of 53.7 % LiF, 40.5 % NaF and 5.8 % PuF$_3$, which makes it suitable for Molten Salt Reactor fuel as proposed in the Generation IV initiative. However, for safety reasons, the liquidus temperature of a LiF-NaF-PuF$_3$ based fuel mixture might have to be lowered by the addition of BeF$_2$, ZrF$_4$ or RbF.

The effect on the eutectic temperature by the latter was investigated. Again, LaF$_3$ was used as analogue for PuF$_3$. The binaries of LiF-NaF-RbF-LaF$_3$ were assessed with the modified quasi-chemical model with quadruplets using experimental data found in the literature. For LiF-RbF, our own DTA data were included in the assessment. The diagram we found was a little different than the one proposed in the literature. The three ternary diagrams containing RbF were calculated by extrapolation of the binary excess coefficients in the same way as was done for LiF-NaF-LaF$_3$. It appeared that addition of RbF has a significant effect on the melting temperature. Adding for example 10 mole % would decrease the amount of LaF$_3$ that can be dissolved by approximately 1 mole %, but the temperature is 30 K lower. From this study it would be recommended to add a small amount of RbF to MSR burner fuel. This should however be tested in the future with active samples.

Gibbs energy data tables

Table 4.10: $\Delta_f H^0$(**298.15 K**), S^0(**298.15 K**) **for the pure components and intermediate compounds of the system LiF-NaF-MF$_3$, with M=La,Ce,Pu.**

Comp.	$\Delta_f H^0$(298.15 K) /kJ·mol^{-1}	S^0(298.15 K) /J·K^{-1}·mol^{-1})
LiF (l)^a	-598.654	42.962
NaF (l)^a	-558.583	50.778
RbF (l)	-542.369	85.103
LaF$_3$ (l)^a	-1633.920	97.639
CeF$_3$ (l)^a	-1650.932	116.739
PuF$_3$ (l)^a	-1568.813	109.331
LiF (cr)^a	-616.931	35.660
NaF (cr)^a	-576.650	51.210
RbF (cr)	-559.700	77.700
LaF$_3$ (cr)^{a,b}	-1669.500	106.980
CeF$_3$ (cr)^a	-1689.200	118.700
PuF$_3$ (cr)^a	-1586.694	126.110
LiRbF$_2$ (cr)	-1177.711	111.773
NaLaF$_4$ (cr)^b	-2254.924	155.515
NaLaF$_4$ (cr)^c	-2240.125	164.80
NaCeF$_4$ (cr)^b	-2308.680	135.160
NaPuF$_4$ (cr)^b	-2221.946	130.110
RbLaF$_4$ (cr)^b	-2228.920	197.165

^{a} Data taken from an internal report [17].

^{b} Obtained by assessment with the polynomial model.

^{c} S^0(298.15 K) was derived from low temperature heat capacity measurements, as described in Chapter 2 (*Calorimetry*), while $\Delta_f H^0$(298.15 K) was optimized.

Table 4.11: C_p **data for the pure components and intermediate compounds of the system LiF-NaF-MF$_3$, with M=La,Ce,Pu.**

Comp.	a T^{-2} /K^{-2}	b	c T /K	d T^2 /K^2	e T^3 /K^3
LiF (l)[a]		64.183			
NaF (l)[a]		72.989			
RbF (l)		71.00			
LaF$_3$ (l)[a]		135.00			
CeF$_3$ (l)[a]		130.61			
PuF$_3$ (l)[a]		130.00			
LiF (cr)[a]	-5.6912E+05	43.309	1.6312E-02	5.0470E-07	
NaF (cr)[a]	-3.8773E+05	42.554	1.9881E-02		
NaF (cr)[b]	-4.6430E+5	47.630	1.4790E-2		
RbF (cr)	-4.6900E+4	42.343	2.6024E-2		
LaF$_3$ (cr)[a]	-2.1714E+06	122.119	-2.2467E-02	-1.6309E-05	2.8175E-08 T^3
CeF$_3$ (cr)[a]	-7.2087E+05	103.258	-1.2990E-02	2.4688E-05	
PuF$_3$ (cr)[a]	-1.0355E+06	104.078	7.07E-04		
LiRbF$_2$ (cr)	-6.1602E+05	85.652	4.2336E-02	5.0470E-7	
NaLaF$_4$ (cr)[c]	-2.2682E+06	165.00	-5.4388E-03	-1.6309E-05	
NaLaF$_4$ (cr)[d]	-4.6607E+05	132.61	2.9109E-02	3.4332E-05	
NaCeF$_4$ (cr)[c]	-1.1086E+06	145.812	6.8911E-03	2.469E-05	
NaPuF$_4$ (cr)[c]	-1.1323E+06	146.910	1.7736E-02		
RbLaF$_4$ (cr)	-3.7160E+06	207.3	-1.1098E-01	8.412E-5	

[a] Data taken from an internal report [17].

[b] Derived by a combination from our own heat capacity analysis of NaF, see Chapter 2 (*Calorimetry*) and data from King [19] and Macleod [22].

[c] Obtained by assessment with the polynomial model.

[d] Function derived from heat capacity measurements, as described in Chapter 2 (*Calorimetry*).

Chapter 5

MSR Breeder Fuels

The composition of MSR Breeder fuel

The uranium resources on Earth are plenty at the moment. May it happen that the reserves become too uneconomical to mine in the future, the use of thorium will be an alternative. Its natural abundance is about three times higher than for uranium [2].

The MSR has the capability of the breeding of uranium from thorium in a thermal spectrum, where neutron capture of ^{232}Th forms ^{233}Th, decaying rapidly to ^{233}Pa, which decays with a half-life of 27 days to ^{233}U, a fissile isotope. The reaction is depicted in Figure 5.1. Not only the best neutronic conditions facilitating this reaction, but also other thermal and physicochemical requirements have to be met. It has been proven that ^{7}LiF-BeF$_2$ is the most appropriate solvent for this fuel type. A small percentage of a fissile isotope, usually ^{235}U, is needed to start the neutron capture reaction. A typical fuel composition for the MSR is therefore a LiF-BeF$_2$-ThF$_4$-UF$_4$ mixture.

The contents of this Chapter were submitted as the papers Van der Meer, Konings and Oonk, "Thermodynamic assessment of the LiF-BeF$_2$-ThF$_4$-UF$_4$ system", J. Nucl. Mater. (in press) and Van der Meer and Konings, "Thermal and physical properties of molten fluorides for nuclear applications", J. Nucl. Mater. (accepted).
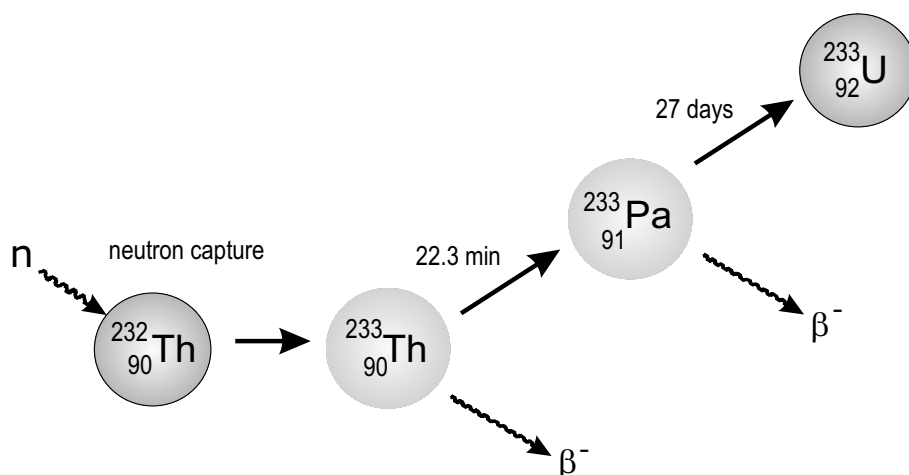
Figure 5.1: The thorium-uranium cycle. When ^{233}U decays, neutrons are released which can be captured by ^{232}Th to repeat the reaction.

Thermodynamic assessment of LiF-BeF$_2$-ThF$_4$-UF$_4$

The liquid phases of the LiF-BeF$_2$-ThF$_4$-UF$_4$ binary subsystems have been assessed using general polynomials, as was explained in Chapter 3 *Solvents*. By extrapolating the optimized Gibbs energy terms from the binaries, the ternary subsystems were calculated, which form the boundaries of the quaternary system.

For the compounds LiF, BeF$_2$, Li$_2$BeF$_4$, ThF$_4$ and UF$_4$, thermodynamic data were taken from an internal report [17]. This was not the case for the large number of intermediate compounds present in this system. Their Gibbs energy equations were obtained by optimization. All optimizations were done using the OptiSage module in the FactSage 5.3 software package [31]. It was assumed that, according to the Neumann-Kopp rule, the C_p could be added in weighted average of the pure compounds, while the enthalpy and entropy of formation needed to be assessed. Table 5.1 and lists these parameters, the literature data as well as the assessed values.

Table 5.1: $\Delta_f H^0$(**298.15 K**), S^0(**298.15 K**) **and** C_p **for the pure components and intermediate compounds containing fuels, as mentioned in this section**

Comp.	$\Delta_f H^0$(298.15 K) /kJ·mol^{-1}	S^0(298.15 K) /J·K^{-1}·mol^{-1}	a	b T /K	c T^{-2} /K^{-2}
ThF$_4$ (l)^a	-2064.491	156.629	133.9		
UF$_4$ (l)^a	-1914.658	115.400	174.74		
ThF$_4$ (cr)^a	-2097.900	142.05	122.173	8.37E-3	-1.2550E+6
UF$_4$ (cr)^a	-1914.200	151.7	114.5194	2.0555E-2	-4.1316E+5
Li$_4$UF$_8$ (cr)^b	-4361.970	344.921	286.724	8.9841E-2	-2.6873E+6
LiUF$_5$ (cr)^b	-2553.303	181.335	157.571	3.7877E-2	-9.8169E+5
LiU$_4$F$_{17}$ (cr)^b	-8367.599	577.206	501.129	9.95412E-2	-2.2212E+6
Li$_3$ThF$_7$ (cr)^b	-4038.525	176.972	251.327	6.0335E-2	-2.9606E+6
LiThF$_5$ (cr)^b	-2812.701	88.713	165.224	2.5692E-2	-1.8235E+6
LiTh$_2$F$_9$ (cr)^b	-4929.261	229.395	287.397	3.4062E-2	-3.0785E+6
LiTh$_4$F$_{19}$ (cr)^b	-9155.485	494.702	531.743	5.0802E-2	-5.5885E+6

^{a} Data taken from an internal report [17].

^{b} Obtained by assessment with the general polynomial model.

The binary subsystems of LiF-BeF$_2$-ThF$_4$-UF$_4$

Six binary subsystems are needed to build the four ternaries of which the quaternary LiF-BeF$_2$-ThF$_4$-UF$_4$ consists. LiF-BeF$_2$ was already described in Chapter 3 *Solvents*. As it was explained, the assessment demands the existence of a small miscibility gap near to the BeF$_2$ axis, in order to obtain an agreement between the enthalpy of fusion of BeF$_2$ and the experimental liquidus data.

LiF-ThF$_4$ and LiF-UF$_4$ are the most complex of the six diagrams containing a number of intermediate components: Li$_3$ThF$_7$, LiThF$_5$, LiTh$_2$F$_9$, LiTh$_4$F$_{17}$, respectively Li$_4$UF$_8$, LiFUF$_5$ and LiU$_4$F$_{17}$. The assessed diagrams of LiF-ThF$_4$ and LiF-UF$_4$ are shown in Figure 5.2, respectively 5.3.
BeF$_2$-ThF$_4$ and BeF$_2$-UF$_4$ are single eutectic systems with the eutectic point close to the BeF$_2$ axis. The assessed diagrams are shown in Figure 5.4, respectively 5.5. ThF$_4$ and UF$_4$ form a continuous solid solution series without a temperature minimum, but the experimental data, consisting of four points, are very limited. Figure 5.6 shows the ThF$_4$-UF$_4$ diagram. Data for the binaries can be found in Table 5.3.

Table 5.2: **Optimized excess Gibbs parameters of the liquid phase for the binaries of LiF-BeF$_2$-ThF$_4$-UF$_4$**

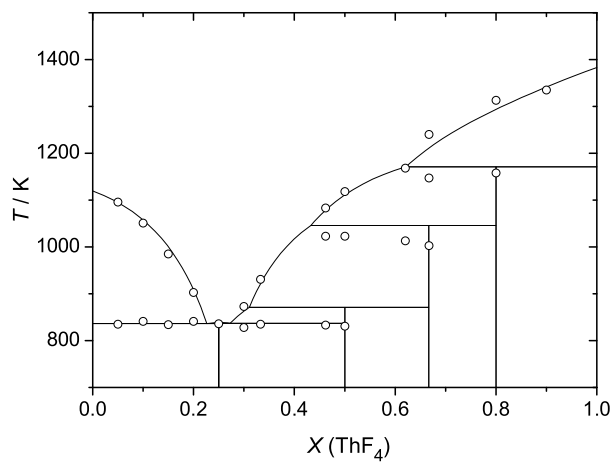| A, B	p	q	$^k L_{A,B}$ /J·mol^{-1}	$^l L_{A,B}$ /J·K^{-1}·mol^{-1}
UF$_4$-LiF	0	0	-75.252	-25.837
	0	1	-78694	38.406
ThF$_4$-LiF	0	0	-141298	102.50
	1	0	43130	-29.459
	0	1	-52637	38.821
BeF$_2$-LiF	0	0	-15580	-11.645
	1	0	71320	-63.487
	0	1	-71320	63.487
	1	1	-9612.0	0.000
	2	1	4806.0	0.000
	1	2	4806.0	0.000
UF$_4$-BeF$_2$	0	0	-33606	9.985
	1	0	-1630.0	27.447
	0	1	68012	-27.462
ThF$_4$-BeF$_2$	0	0	16749	-11.462
UF$_4$-ThF$_4$[a]	0	0	661.46	-1.4789

[a] ThF$_4$ and UF$_4$ form a solid solution.

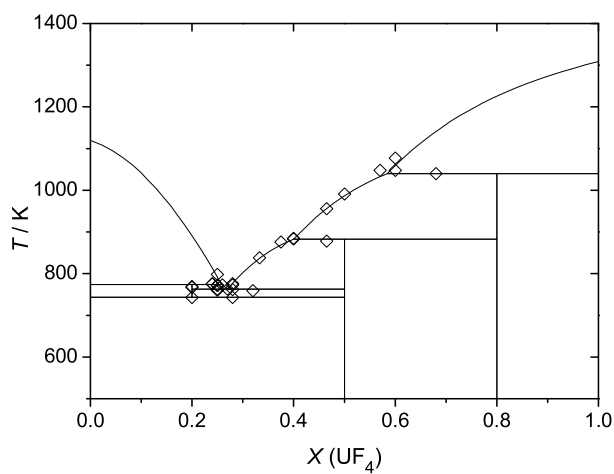Figure 5.2: The assessed LiF-ThF$_4$ diagram; ∘ experimental data from Thoma *et al.* [77].

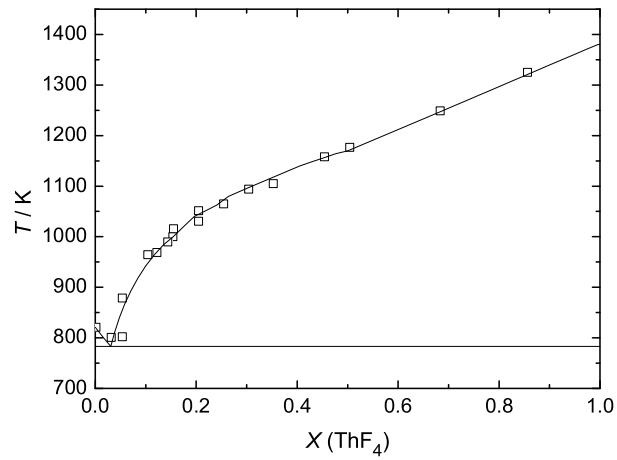Figure 5.3: The assessed LiF-UF$_4$ diagram; ◊ experimental data by Thoma *et al.* [77].

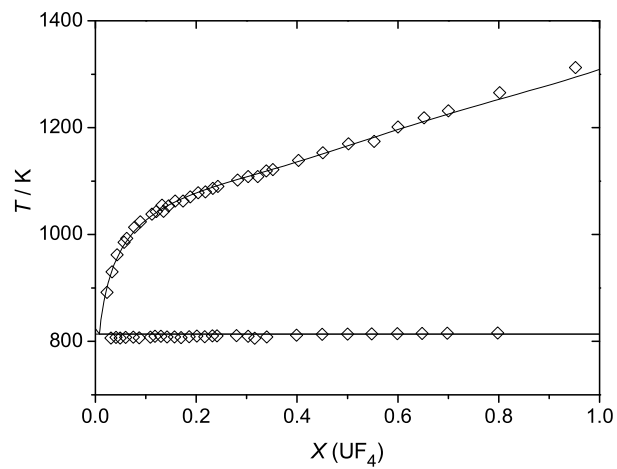Figure 5.4: The assessed BeF_2-ThF_4 diagram; □ experimental data from Thoma *et al.* [78].

Figure 5.5: The assessed BeF_2-UF_4 diagram ◊ experimental data by Jones *et al.* [79].

Table 5.3: **Invariant equilibria in the binary subsystems of LiF-BeF$_2$-ThF$_4$-UF$_4$, calculated and *experimental (in italics)*[a]**

A–B	X_B	T/K	$X_{B,exp}$	T_{exp}/K	type invariant
LiF-UF$_4$[a]	0.200	742.8	*0.200*	*743*	lower stab. 4LiF·UF$_4$
	0.258	774.2	*0.26*	*773*	peritectic
	0.269	763.7	*0.27*	*763*	eutectic
	0.400	883.1	*0.40*	*883*	peritectic
	0.586	1040.0	*0.57*	*1048*	peritectic
LiF-ThF$_4$[b]	0.224	841.8	*0.23*	*841*	eutectic
	0.250	846.5	*0.25*	*846*	congr. m.p.
	0.283	840.0	*0.29*	*838*	eutectic
	0.302	855.7	*0.305*	*870*	peritectic
	0.428	1035.7	*0.42*	*1035*	peritectic
	0.603	1171.4	*0.62*	*1170*	peritectic
LiF-BeF$_2$[c]	0.330	728.6	*0.328*	732.0	eutectic
	0.333	728.7	*0.333*	*732.3*	congr. m.p.
	0.519	635.0	*0.531*	*636.7*	eutectic
	0.760	786.5	*not found*		begin RoD[f]
	0.871	811.9			max. RoD
	0.950	786.5			end RoD
BeF$_2$-UF$_4$[d]	0.008	813.6	*0.005*	*808*	eutectic
BeF$_2$-ThF$_4$[e]	0.023	794.8	*0.020*	*800*	eutectic

[a] Experimentally determined invariant points by Barton *et al.* [81].
[b] By Thoma *et al.* [77].
[c] By Romberger *et al.* [40].
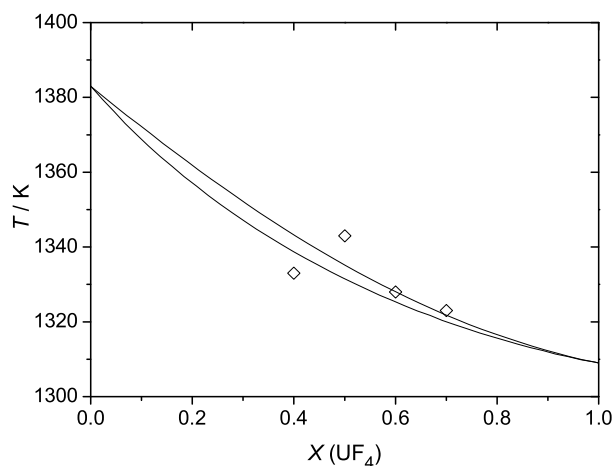[d] By Jones *et al.* [79].
[e] By Thoma *et al.* [78].
[f] Region of Demixing.

Figure 5.6: The assessed ThF$_4$-UF$_4$ diagram $\Diamond$ experimental data by Weaver

et al. [80].

Calculation of higher order phase diagrams

The ternary phase diagrams were obtained by extrapolation of the binary interaction coefficients. The Kohler-Toop method was applied, which is suitable for chemically asymmetric systems. In the systems LiF-ThF$_4$-UF$_4$ and BeF$_2$-ThF$_4$-UF$_4$, the chemical asymmetric component is evidently LiF, respectively BeF$_2$. However, for LiF-BeF$_2$-ThF$_4$ and LiF-BeF$_2$-UF$_4$ discussion could arise how to treat the different components. In this case, LiF was selected as the asymmetric component, as will be explained in the paragraph *The asymmetric component in LiF-BeF$_2$-ThF$_4$*. An example of how three binaries are combined to a ternary diagram is seen in Figure 5.7, where the LiF-BeF$_2$-ThF$_4$ triangle is shown with the three binary subsystems forming its boundaries.

Figure 5.8 shows the calculated liquidus surface of LiF-BeF$_2$-ThF$_4$, LiF-BeF$_2$-UF$_4$, LiF-ThF$_4$-UF$_4$ and BeF$_2$-ThF$_4$-UF$_4$, such that they form a quaternary system. The figure can be considered as an open-folded tetrahedron with LiF-BeF$_2$-ThF$_4$ as the base and UF$_4$ at the apex.

LiF-BeF$_2$-ThF$_4$ contains a eutectic and a (quasi) peritectic point in the LiF rich part. Another eutectic (695.0 K) and a quasi peritectic (751.0 K) are found very near to the LiF-BeF$_2$ axis, which is indicated in Table 5.4. The assessed diagram of LiF-BeF$_2$-ThF$_4$ was published previously by us [82]. However, a

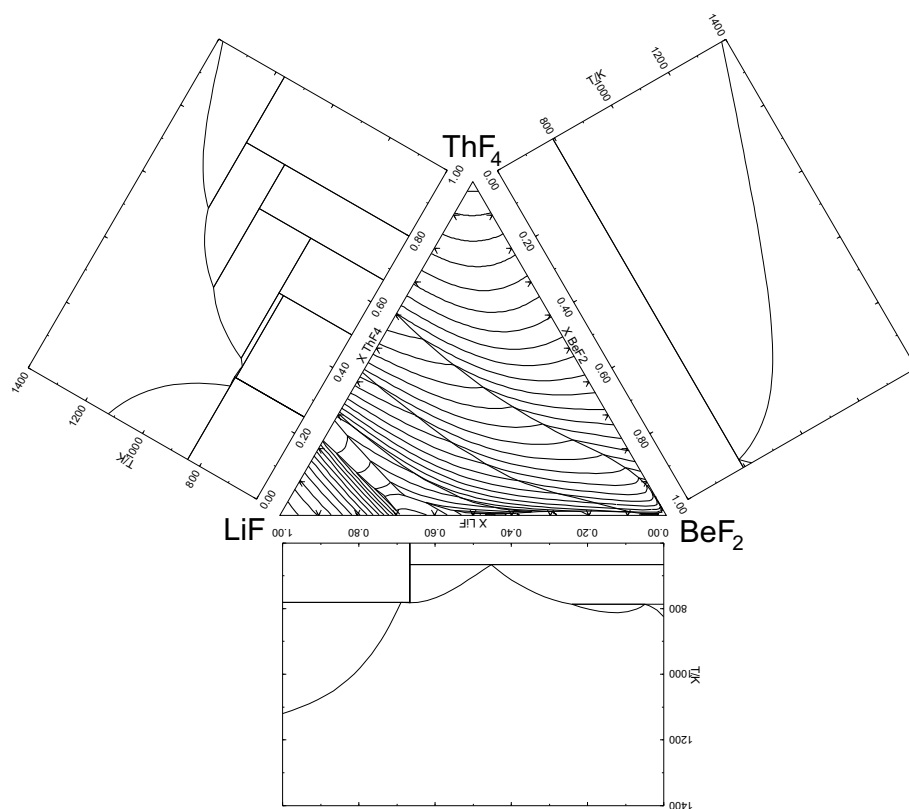Figure 5.7: The projection of the liquidus surface of LiF-BeF$_2$-ThF$_4$. Isotherms with an interval of 25 K are shown. The three binary subsystems are along the sides.

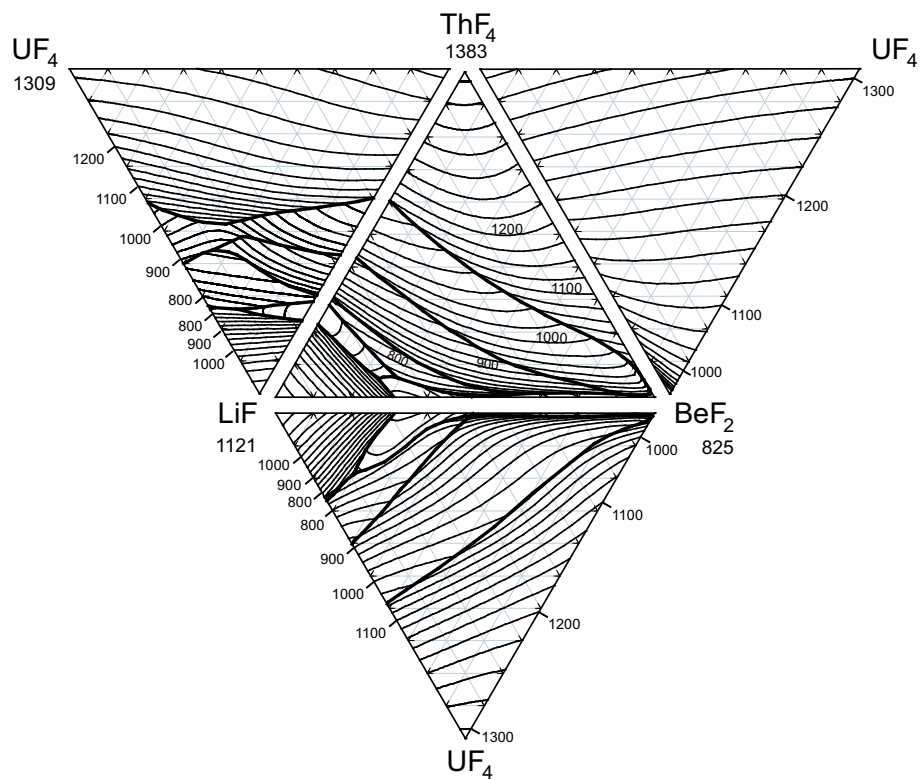Figure 5.8: The calculated liquidus surface of LiF-BeF$_2$-ThF$_4$, LiF-BeF$_2$-UF$_4$, LiF-ThF$_4$-UF$_4$ and BeF$_2$-ThF$_4$-UF$_4$, combined to a quaternary system. Melting temperatures are labelled in K and isotherms with an interval of 25 K are shown.

modification of the diagram is shown here. The diagram we published first [82] was characterized by a significant ternary miscibility gap in the BeF$_2$ apex. A more thorough discussion can be found in the paragraph *The asymmetric component in LiF-BeF$_2$-ThF$_4$*.

LiF-BeF$_2$-UF$_4$ is analogous to the former system, but not similar, as LiF-UF$_4$ has one intermediate compound less than LiF-ThF$_4$. The point, at which LiF·4UF$_4$ decomposes, is very near to the LiF-UF$_4$ axis of the ternary. A eutectic can be found in the LiF rich region (712.9 K). Two other invariant points, a quasi peritectic (691.9 K) and eutectic (695.0 K), nearly touch the LiF-BeF$_2$ axis.

LiF-ThF$_4$-UF$_4$ contains three solid solution series: LiF·(Th,U)F$_4$, LiF·4(Th,U)F$_4$ and (Th,U)F$_4$. The solid-liquid phase diagram of ThF$_4$-UF$_4$ (Figure 5.6) shows evidence of weak deviations from ideal-mixing behavior. For that matter, the solid solutions were treated as ideal mixtures, putting all deviations from ideality in the liquid. One eutectic (760.2 K) and two quasi peritectic points (767.7 and 903.8 K)are present in this ternary. The invariant points of the three ternary systems mentioned above are described in Table 5.4.

The simplest of the four ternaries is BeF$_2$-ThF$_4$-UF$_4$, where the solid solution series between ThF$_4$ and UF$_4$ dominates. A ternary eutectic point does not exist, however, a eutectic line smoothly connects the two binary eutectics, which are almost at the BeF$_2$ apex.

Comparison ternary model and experimental data

Table 5.4 lists the invariant points of the systems LiF-BeF$_2$-ThF$_4$, LiF-BeF$_2$-UF$_4$ and LiF-ThF$_4$-UF$_4$, as found in the calculated diagrams and compares these to the experimentally derived values. It can be noticed that many calculated equilibria differ, not only in temperature, but also in composition, from the experimental ones. The composition of a ternary invariant point is sometimes not so straightforward as one would expect from studying the ternary diagram. When plotting binary cross-sections, the so-called pseudobinaries, far more complicated phase field relationships are revealed, which are not directly visible in the ternary.

Tables belonging to the papers [78, 79, 80], which were deposited at the Library of Congress in Washington D.C., contain all experimental data on LiF-BeF-ThF$_4$ (thermal gradient quenching and DTA cooling), LiF-BeF$_2$-UF$_4$ (DTA

Table 5.4: **Invariant equilibria in the ternary subsystems A-B-C of LiF-BeF$_2$-ThF$_4$-UF$_4$, calculated and *experimental (in italics)*[a]**

A	B	C	T/K	type invariant	phases present
LiF	BeF$_2$	ThF$_4$			
0.70	0.24	0.06	758.9	eutectic[b]	LiF + 3LiF·ThF$_4$ + 2LiF·BeF$_2$ = L
0.65	0.29	0.06	754.7	peritectic	3LiF·ThF$_4$ + LiF·ThF$_4$ + 2LiF·BeF$_2$ + L[c]
0.48	0.515	0.005	695.0	eutectic	2LiF·BeF$_2$ + BeF$_2$ + LiF·ThF$_4$ = L
0.34	0.65	0.01	751.0	peritectic	LiF·ThF$_4$ + LiF·2ThF$_4$ + BeF$_2$ + L[d]
0.66	*0.30*	*0.04*	*717*	*peritectic*	*LiF + 3LiF·ThF$_4$ + 2LiF·BeF$_2$ + L*
0.63	*0.30*	*0.07*	*721*	*peritectic*	*3LiF·ThF$_4$ + LiF·ThF$_4$ + LiF·2ThF$_4$ + L*
0.61	*0.36*	*0.03*	*706*	*peritectic*	*3LiF·ThF$_4$ + LiF·2ThF$_4$ + 2LiF·BeF$_2$ + L*
0.47	*0.51*	*0.02*	*629*	*eutectic*	*2LiF·BeF$_2$ + BeF$_2$ + LiF·2ThF$_4$ + L*
0.34	*0.64*	*0.03*	*728*	*peritectic*	*LiF·2ThF$_4$ + LiF·4ThF$_4$ + BeF$_2$ + L*
0.15	*0.83*	*0.02*	*770*	*peritectic[f]*	*ThF$_4$ +LiF·4ThF$_4$ + BeF$_2$ + L*
LiF	BeF$_2$	UF$_4$			
0.72	0.05	0.23	742.3		decomposition of 4LiF·UF$_4$
0.70	0.12	0.18	712.9	eutectic	LiF + LiF·UF$_4$ + 2LiF·BeF$_2$ = L
0.49	0.50	0.01	695.0	eutectic	2LiF·BeF$_2$ + LiF·UF$_4$ + BeF$_2$ = L
0.48	0.51	0.01	691.9	peritectic	2LiF·BeF$_2$ + LiF·4UF$_4$ + BeF$_2$ + L[e]
0.72	*0.06*	*0.22*	*753*	*peritectic*	*decomposition of 4LiF·UF$_4$*
0.69	*0.23*	*0.08*	*699*	*eutectic*	*LiF + LiF·UF$_4$ + 2LiF·BeF$_2$ + L*
0.48	*0.515*	*0.005*	*623*	*eutectic*	*2LiF·BeF$_2$ + LiF·UF$_4$ + LiF·4UF$_4$ + L*
0.455	*0.54*	*0.005*	*654*	*peritectic*	*2LiF·BeF$_2$ + LiF·4UF$_4$ + BeF$_2$ + L*
0.295	*0.70*	*0.005*	*756*	*peritectic[f]*	*UF$_4$ + LiF·4UF$_4$ + BeF$_2$ + L*
LiF	ThF$_4$	UF$_4$			
0.74	0.07	0.19	767.7	peritectic	LiF + LiF·(Th,U)F$_4$ + L[g]
0.735	0.015	0.25	760.2	eutectic	LiF + 4LiF·UF$_4$ + LiF·(Th,U)F$_4$ = L
0.56	0.10	0.34	903.8	peritectic	LiF·(Th,U)F$_4$ + LiF·4(Th,U)F$_4$ + L[h]
0.725	*0.07*	*0.205*	*773*	*peritectic*	*LiF + 3LiF·ThF$_4$ + 4LiF·UF$_4$*
0.72	*0.015*	*0.265*	*761*	*eutectic*	*LiF + 4LiF·UF$_4$ + LiF·(Th,U)F$_4$ + L*
0.63	*0.18*	*0.19*	*882*	*peritectic*	*LiF·(Th,U)F$_4$ + LiF·2ThF$_4$ + LiF·4(Th,U)F$_4$ + L*

[a] Values in *italics* are proposed values, based on experiments and extrapolation. LiF-BeF$_2$-ThF$_4$ was analyzed by Thoma *et al.* [78], LiF-BeF$_2$-UF$_4$ by Jones *et al.* [79] and LiF-ThF$_4$-UF$_4$ by Weaver *et al.* [80].

[b] 2LiF·BeF$_2$ was considered as incongruently melting compound at the time of analysis. However, detailed measurements by Romberger et al. [40] showed that it melts congruently, so that the peritectic can now be interpreted as eutectic point.

[c] Saddle point: 3LiF·ThF$_4$ + LiF·ThF$_4$ + 2LiF·BeF$_2$ + L = 2LiF·BeF$_2$ + L

[d] Saddle point: LiF·ThF$_4$ + LiF·2ThF$_4$ + BeF$_2$ + L = L

[e] Saddle point: 2LiF·BeF$_2$ + LiF·4UF$_4$ + BeF$_2$ = 2LiF·BeF$_2$ + L

[f] This peritectic point has not been found in the calculated diagram.

[g] Saddle point: LiF + LiF·(Th,U)F$_4$ + L = L

[h] Saddle point: LiF·(Th,U)F$_4$ + LiF·4(Th,U)F$_4$ + L = L

cooling, thermal gradient quenching and high-temperature filtration) and LiF-ThF$_4$-UF$_4$ (thermal gradient quenching). A comparison was made between liquidus surface of the calculated and the experimentally defined diagrams. Therefore, all liquidus data were carefully extracted from the data tables. Then the precipitation temperature of these compositions were calculated using the Equilib module in FactSage. The difference between model and experimental temperature was normalized by the experimental temperature T_{exp} and plotted versus T_{exp}. The results are shown in Figure 5. It can be seen that the agreement in all three systems is generally good, all within $\pm$ 10 %, while 79.1 % of the data agree better than $\pm$ 5 %. It must be noted, however, that the difference between the quenching and the cooling results is significant. A comparison was made between liquidus temperatures obtained by cooling and quenching for similar compositions. It appeared that differences from 20, 30, even up to 70 K are common. Thus, as the data scatter internally to this extent, it makes it complicated to determine the differences between the model and experiment. Performing our own DTA experiments would be priority in a future study on this system.

The asymmetric component in LiF-BeF$_2$-ThF$_4$

In an initial calculation of the LiF-BeF$_2$-ThF$_4$ diagram, it was assumed that BeF$_2$ was the chemically asymmetric component, which was given therefore a different weight in the Kohler-Toop extrapolation of the binary excess Gibbs coefficients. BeF$_2$ was selected because it is known to form polymeric species in the liquid phase and it was therefore anticipated to exert a different behavior than the other two compounds. This resulted in a ternary diagram with a significant miscibility gap in the BeF$_2$ corner, which is shown in Figure 5.10.

However, we realized after comparing the excess Gibbs energy curves of the three binaries that selecting LiF would be a better option.

As it can be seen in Figure 5.11, the excess Gibbs curves of LiF-BeF$_2$ and LiF-ThF$_4$ at 1100 K are both negative and of the same order of magnitude. This is in contrast to the BeF$_2$-ThF$_4$ curve, which is smaller and positive at the same temperature. This difference due to the presence of LiF could be explained by the fact that LiF is highly ionic, whereas BeF$_2$ and ThF$_4$ have the tendency to form more molecular-type ions as BeF$_4^{2-}$ [83] and ThF$_6^{2-}$ in the melt. Raman spectroscopy on molten LiF-BeF-ThF$_4$ mixtures could provide welcome information on the structure of the melt, because the model used
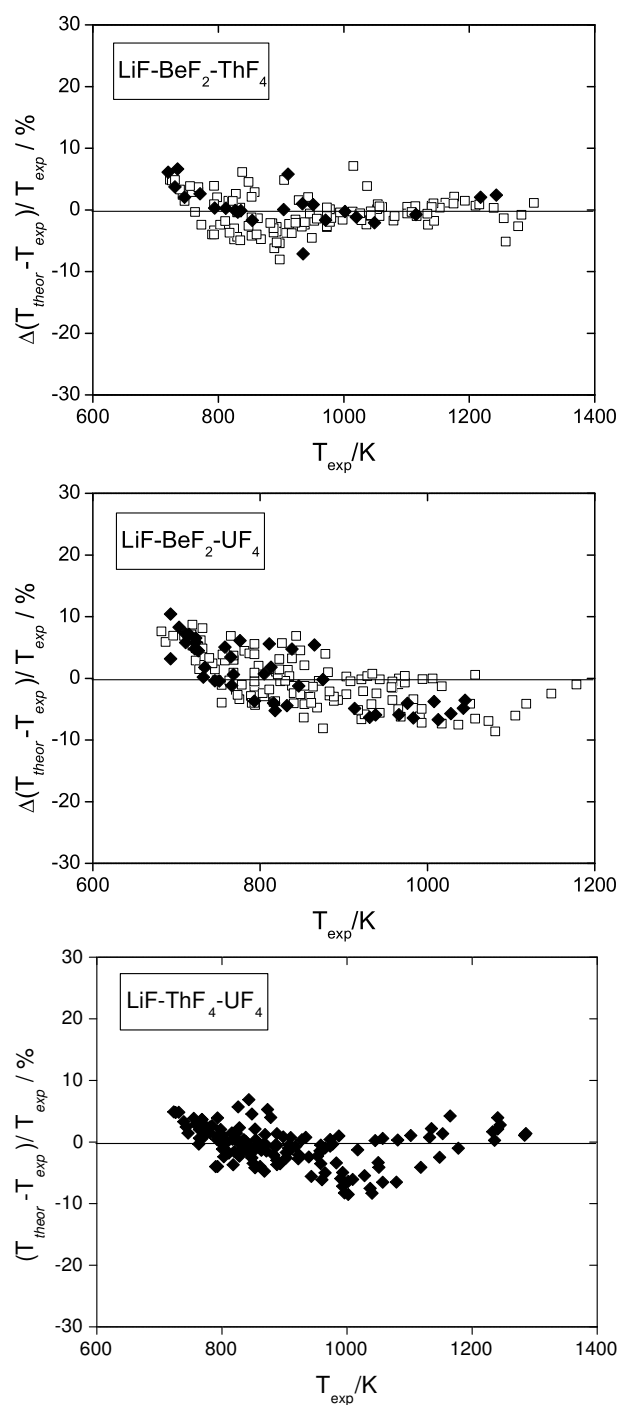
Figure 5.9: The difference between the calculated and the experimental ternary liquidus temperature T_{exp} of LiF-BeF$_2$-ThF$_4$, LiF-BeF$_2$-UF$_4$ and LiF-ThF$_4$-UF$_4$, normalized by T_{exp}, versus T_{exp}. Open symbols: obtained by cooling; closed symbols: obtained by quenching.
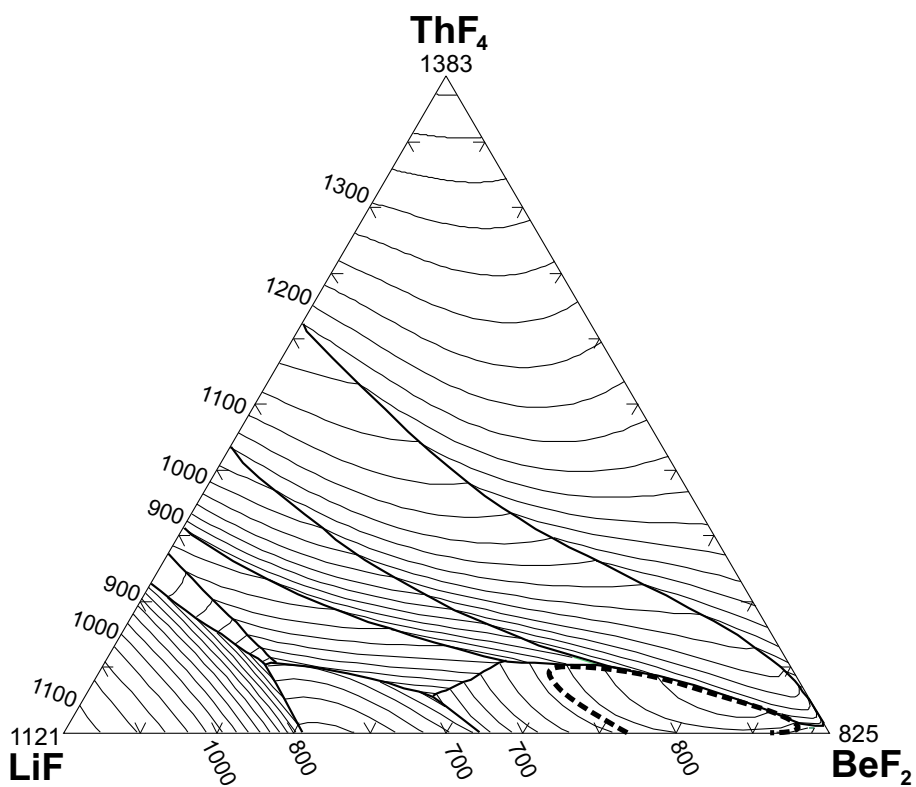
Figure 5.10: The calculated liquidus surface of LiF-BeF$_2$-ThF$_4$. The miscibility gap is indicated as a dashed line. Isotherms are labeled in K.

here is not conclusive.

The shape of the diagram, calculated by the LiF asymmetry model, resembles the experimental diagram from Thoma *et al.* [78] much better than the BeF_2 asymmetry model and also the overall agreement with the experimental data is better. However, there is a feature when comparing the two models, that should be noted. Concerning the LiF asymmetry model, the lowest temperatures appear to have the largest deviation from the experimental values, which can be seen in Figure 5, where the disagreement is slightly increasing with decreasing temperatures. This inevitably holds that the ternary invariant points, which belong to the lowest temperatures in the system, differ more from the experimental data than the liquidus at higher temperatures. A check was performed on the temperature dependance of the excess Gibbs energy. Therefore, a number of extra terms were introduced in the excess Gibbs energy function to see whether a better description could be obtained at the lower temperatures, but without satisfying result.

A similar plot comparing the model with the experiments was made for BeF_2 asymmetry as well. In this case, the deviations from the experimental data are larger and more scattered through the temperature spectrum. So, here it could happen that the invariant temperatures showed a better agreement with the experiments [82], but the compositions deviated more.

The miscibility gap present in LiF-BeF_2 has its influence on the ternaries LiF-BeF_2-ThF_4 and LiF-BeF_2-UF_4, where a small gap can be found close to the LiF-BeF_2 axis. However, the addition of exactly 1.0 mole % of ThF_4 and 0.9 mole % UF_4, which was revealed by systematically calculated pseudobinary diagrams crossing the ternary demixing areas, is enough to suppress this two-phase field. Hence it is explicable that Thoma *et al.* [78] and Jones *et al.* [79] do not mention the existence of ternary miscibility gaps.

Next to the miscibility gap, a couple of minor differences were found in the comparison with the invariant points of LiF-BeF_2-ThF_4, see Table 5.4, due to a change in the field stability of $LiThF_5$. Thoma *et al.* proposed the $LiF·ThF_4$ phase to be stable in a small part of the diagram, ending in a peritectic at 0.63 LiF-0.30 BeF_2-0.07 ThF_4. In our model, this field is broader and ends in the peritectic at 0.34 LiF-0.65 BeF_2-0.01 ThF_4. A possible explanation could be the fact that four intermediate LiF-ThF_4 compounds exist of which we do not have thermodynamic data. They were optimized in the binary system, but it cannot be excluded that the description of the thermodynamic parameters is not sufficient for extrapolation in a ternary system.
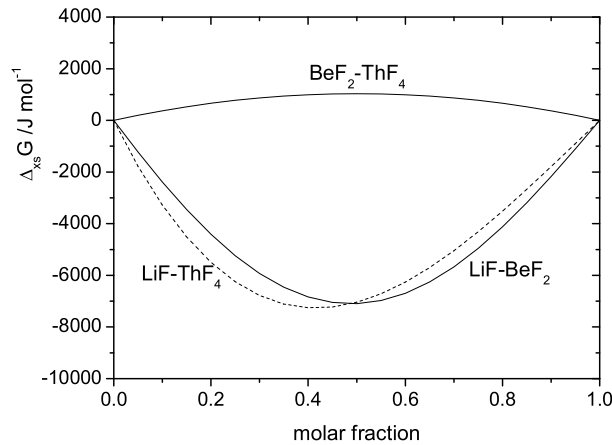
Figure 5.11: The excess Gibbs energy curves of LiF-BeF$_2$, LiF-ThF$_4$ (dashed line) and BeF$_2$-ThF$_4$.

Cross-section through LiF-BeF$_2$-ThF$_4$

Figure 5.12 is an example of a cross-section through the LiF-BeF$_2$-ThF$_4$ diagram. It shows the complexity of the system, especially below the liquidus. It can be seen that the model reproduces the available liquidus data well, with the exception of the range $0.3 < X_{BeF_2} < 0.4$. Here the ORNL data show even an increase towards the eutectic, whereas the model decreases in temperature. Something else that should be noted is the number of observed thermal effects that exceeds the number of phase boundaries. It can be partly explained by the fact that one intermediate compound, LiBeF$_3$, has deliberately been omitted from the assessment, since it decomposes in the solid phase and has no influence on the liquidus. But otherwise, it is interesting to have a closer examination of the range $0.2 < X_{BeF_2} < 0.4$ and to repeat the ORNL experiments to have more certainty which thermal signal corresponds to which phase transition. Generally, it would be helpful to know the intensity of the observed effects. We know from previous DTA measurements [24], that the formation of a eutectic or peritectic melt gives the largest signal, much more than when the liquidus is crossed. One can wonder if the two observed liquidus signals at X_{BeF_2}=0.221, T=754.9 K and X_{BeF_2}=0.244, T=758.5 K are probably not misinterpreted eutectic and peritectic events? They coincide namely almost exactly with our calculated ternary invariant points of 758.9 K and 754.7 K,

see Table 5.4.

In general, it can be concluded that the polynomial model with Kohler-Toop extrapolation gives a satisfactory description of the binary and the higher order systems of LiF-BeF$_2$-ThF$_4$-UF$_4$, especially LiF-BeF$_2$-UF$_4$, LiF-ThF$_4$-UF$_4$ and BeF$_2$-ThF$_4$-UF$_4$, since the diagrams agree with the determined invariant points and the experimental liquidus data. Nevertheless, it might be worthwhile for a future study to use another model, for example the quasi-chemical model in quadruplet approximation by Pelton *et al.* [53], to see if the agreement with experiments and model can be improved. For the system LiF-NaF-LaF$_3$ we made already a comparison between the results obtained by the quadruplet model and by the polynomial description we used in this study. In that case it appeared that the differences are minor, but it is not certain what the results will be in LiF-BeF$_2$-ThF$_4$-UF$_4$.

Comparison quaternary model and experimental data

A comparison considering the possible composition for a Molten Salt Reactor was also made. The Molten Salt Breeder Reactor, MSBR, was designed in the 1960's to breed ^{233}U from ^{232}Th in a LiF-BeF$_2$ melt. A favorable composition was 71.7 % LiF- 16 % BeF$_2$- 12 % ThF$_4$- 0.3 % UF$_4$ in moles, with the small amount of UF$_4$ to start the reaction [4]. The temperature of fusion was determined to be 773 ± 5 K, according to a report by Cantor [49]. This is in reasonable agreement with the somewhat higher calculated temperature of 794.5 K, which is the precipitation temperature of the composition 71.7 % LiF- 16 % BeF$_2$- 12.3 % (Th$_{0.9756}$U$_{0.0244}$)F$_4$. It has been found as well that without the addition of 0.3 % UF$_4$ the precipitation temperature would increase by exactly 2 K. Four possible compositions for breeder fuel, which were analyzed by Cantor [49], appear in Table 5.5 with the experimentally determined and calculated temperatures.

The vapor pressure of MSR Breeder fuel

Low vapor pressures at the operating temperature are desirable for safety reasons. The partial vapor pressures of the gaseous phase were calculated in the temperature range 400-1500 K for the typical Molten Salt Breeder fuel,
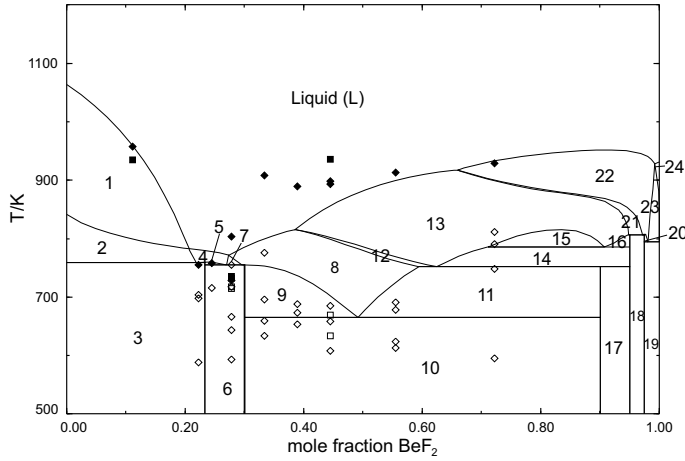
Figure 5.12: Pseudobinary $Li_{0.9}Th_{0.1}F_{1.3}$ - $Be_{0.9}Th_{0.1}F_{2.2}$ section of the pseudoternary LiF-BeF_2-ThF_4 system. ∎ liquid, obtained by quenching; ♦ liquid, obtained by cooling; □ other phase transitions obtained by quenching; ◇ other thermal effects occurring on cooling, all data extracted from tables according to Thoma et al. [78]. Phases: 1 LiF+L; 2 LiF+Li_3ThF_7+L; 3 LiF+Li_3ThF_7+Li_2BeF_4; 4 Li_3ThF_7+L; 5 Li_3ThF_7+Li_2BeF_4+L; 6 Li_2BeF_4+Li_3ThF_7+$LiThF_5$; 7 Li_3ThF_7+$LiThF_5$+L; 8 $LiThF_5$+L; 9 Li_2BeF_4+$LiThF_5$+L; 10 Li_2BeF_4+$LiThF_5$+BeF_2; 11 $LiThF_5$+BeF_2+L; 12 $LiThF_5$+$LiTh_2F_9$+L; 13 $LiTh_2F_9$+L; 14 $LiTh_2F_9$+BeF_2+L; 15 $LiTh_2F_9$+L+L_2; 16 $LiTh_2F_9$+L; 17 $LiThF_5$+$LiTh_2F_9$+BeF_2; 18 $LiTh_2F_9$+$LiTh_4F_{17}$+BeF_2; 19 $LiTh_4F_{17}$+ThF_4+BeF_2; 20 $LiTh_4F_{17}$+BeF_2+L; 21 $LiTh_2F_9$+$LiTh_4F_{17}$+L; 22 $LiTh_4F_{17}$+L, 23 $LiTh_4F_{17}$+ThF_4+L; 24 ThF_4+L

Table 5.5: **Compositions of MSR Breeder fuel as proposed by ORNL with experimental and calculated temperature**

LiF	BeF_2	ThF_4	UF_4	T_{exp}/K	T_{cal}/K
0.73	0.16	0.107	0.003	773	790
0.72	0.21	0.067	0.003	773	794
0.68	0.20	0.117	0.003	753	785
0.63	0.25	0.117	0.003	773	790

as mentioned in the *Thermodynamic assessment* section. The calculations were performed using the Equilib module in the FactSage software package. $\Delta_f H^0$(298.15 K), S^0(298.15 K) and C_p for the gaseous phase for every component present in the vapor were needed to calculate the partial and the total vapor pressures. The values were extracted from the NIST-JANAF thermochemical tables [29] and are listed in Table 5.6. For the liquid phase the solution model as presented in the *Thermodynamic assessment* section was used.

Figure 5.13 shows the partial and total vapor pressures of the Molten Salt Breeder fuel composition. LiF also exists as a dimer, Li_2F_2, in the gas. It can be seen that over the whole temperature range the total vapor pressure is dictated by BeF_2. In the range 750-900 K, in which the MSR will operate, the total pressure increases from 10^{-8} to 10^{-6} bar. This is a low value and it proves that this fluoride mixture meets the demand of a low vapor pressure in a MSR system at working temperatures.

Cantor *et al.* [49] investigated the vapor pressure of MSBR fuel. He proposed a pressure-temperature relation according to Eq. 5.1. This function is also plotted in Figure 5.13 and it can be seen that the agreement between the calculated and the experimental values is good.

$$^{10}\log(p/\text{torr}) = 8.0 - \frac{10000}{T/\text{K}} \tag{5.1}$$

Eq. 5.1 was estimated from the vapor pressure measurements of LiF-BeF_2 mixtures by Cantor *et al.* [84]. Compared were the mixtures with the same LiF/BeF_2 ratio as in MSBR fuel, which is 81.8 mole % LiF to 18.2 mole % BeF_2. At $T = 1273$ K, $^{10}\log(p/\text{bar})$ is -2.48 and at $T = 1373$ K $^{10}\log(p/\text{bar})$
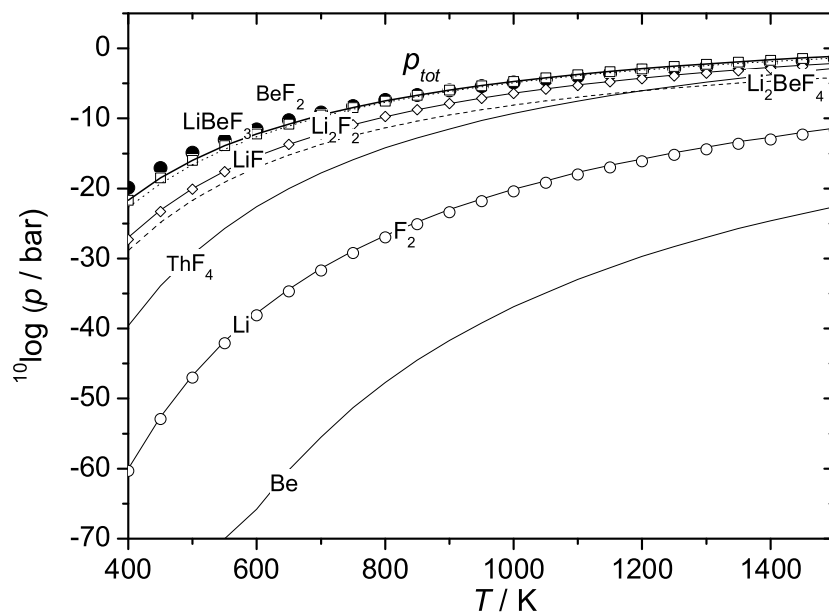
Figure 5.13: The partial and total vapor pressures of a typical Molten Salt Breeder fuel composition. Plotted as well is the total vapor pressure (•) as given by Cantor *et al.* [49].

Table 5.6: $\Delta_f H^0$(298.15 K)/kJ·mol^{-1}, S^0(298.15 K)/J·K^{-1}·mol^{-1} and C_p data for the components in the gas phase with composition 0.717 LiF - 0.16 BeF$_2$ - 0.123 ThF$_4$

X	$\Delta_f H^0$	S^0	a	bT /K	cT^2 /K^2	dT^3 /K^3	eT^{-2} /K^{-2}
LiF	-340.575	200.28	32.31	7.513·10^{-3}	-3.249·10^{-6}	5.010·10^{-10}	-2.657·10^5
Li$_2$F$_2$	-942.781	258.63	79.21	3.470·10^{-3}	-7.641·10^{-7}		-1.515·10^6
LiBeF$_3$	-1390.30	292.58	113.2	2.995·10^{-3}	2.701·10^{-6}	5.008·10^{-10}	-1.144·10^{4,b}
Li$_2$BeF$_4$	-1958.20	324.45	173.4	-3.112·10^{-3}	-1.001·10^{-6}	3.217·10^{-10}	-1.979·10^{4,b}
BeF$_2$	-796.190	227.56	47.30	1.895·10^{-2}	-8.438·10^{-6}	1.259·10^{-9}	-5.216·10^5
ThF$_4$^{a}	-1748.20	351.56	122.4	-1.406·10^{-2}	7.365·10^{-6}	-1.939·10^{-9}	-7.545·10^{3,b}

^{a} An extra term appeared to fit the C_p function optimally: 2.011·10$^{-13}T^4$/K^4.

^{b} This coefficient is eT^{-1}/K^{-1}.

is -1.93. The calculated total vapor pressure ^{10}log(p_{cal}/bar) for LiF-BeF$_2$ at the same conditions was -2.43, respectively -1.75, which is in good agreement with the experimental values.

The density of MSR Breeder fuel

The density of mixtures

Engineers need to know the density of the fuel mixture for the reactor design. Densities of pure components are usually known, but data on the densities of mixtures are scarcer. In this section it is investigated how the density of mixtures can be derived from the density of the pure components.

The density ρ is defined as the ratio of the molar weight M and the molar volume V_m:

$$\rho/\mathrm{kg}\cdot\mathrm{m}^{-3} = \frac{M/10^3 \mathrm{\ g}\cdot\mathrm{mol}^{-1}}{V_m/\mathrm{m}^3} \tag{5.2}$$

The molar weight of a mixture is simply the sum of the molar weights of its components:

$$\mathrm{M} = \sum N_i M_i \tag{5.3}$$

For the molar volume this is only the case for ideal mixtures:

$$\mathrm{V}_{idm} = \sum N_i V_i \tag{5.4}$$

resulting in a linear variation as a function of composition in case of a binary system. In practise many mixtures are not ideal but real, and deviations from the linearity can be observed:

$$\mathrm{V}_m = V_{idm} + V_{exs} \tag{5.5}$$

It should be noted that the melting point of a mixture is often much lower than that of the end member compounds, and the measurements for the mixture are made in a temperature range where the liquid phases of the end member compounds are thermodynamically not stable. In that case the experimental molar volume of the end-member compounds is extrapolated to the supercooled state.

LiF-BeF$_2$

The density of liquid LiF-BeF$_2$ has been measured by Blanke *et al.* [85] from 0 mole % to 55 mole % BeF$_2$, and Cantor *et al.* [86] for 50.2, 74.9 and 89.2 mole % BeF$_2$. The results are shown in Figure 5.14 in an isothermal section for T = 1073 K of the molar volume. This figure confirms the linear dependence on the mole fraction and thus the additivity of the molar volumes. It can also be seen that the result of Cantor [87] is in perfect agreement with the relation based on the experimental molar volume of BeF$_2$ and the extrapolated molar volume of LiF in the supercooled state.
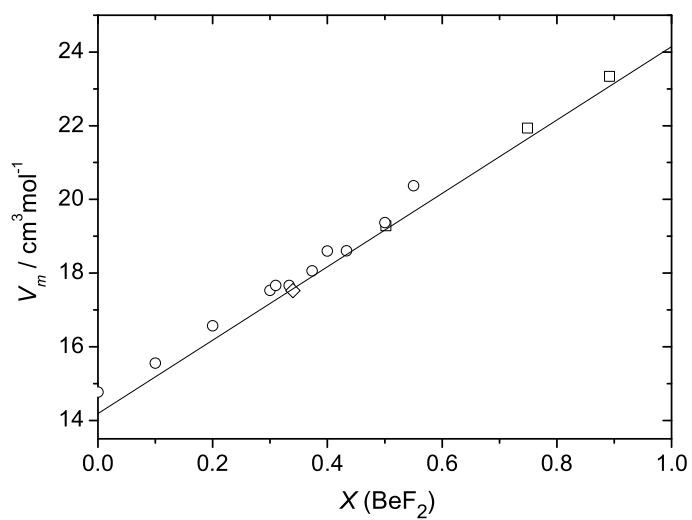
Figure 5.14: The molar volume of liquid LiF-BeF$_2$ at 1073 K; ∘ Blanke *et al.* [85], □ Cantor *et al.* [86]; ◇ Cantor [87]; the line represents V_m of the ideal mixture.

LiF-ThF$_4$

The density of LiF-ThF$_4$ mixtures was measured by Porter and Meaker [88] and Hill *et al.* [89]. The results are in good agreement and clearly indicate a linear dependence of the molar volume with composition, confirming ideal behavior, which is shown in Figure 5.15.

BeF$_2$-ThF$_4$

The density of liquid BeF$_2$-ThF$_4$ has not been determined experimentally. However, the density of the liquid of the analogous system BeF$_2$-UF$_4$ was measured by Blanke *et al.* [85], though only for a single composition (35 mol% UF$_4$). The molar volume derived from this value (30.4 cm$^3\cdot$ mol^{-1} at $T =$ 1073 K) is in reasonable agreement with the value calculated for an ideal mixture of the pure components (31.9 cm$^3\cdot$ mol^{-1}), taking into account the uncertainties for the value for BeF$_2$.

LiF-BeF$_2$-ThF$_4$

Since the molar volumes of the liquid phases of the LiF-BeF$_2$ and LiF-ThF$_4$ binaries show ideal behavior, the same can be assumed for the LiF-BeF$_2$-ThF$_4$ ternary system. The densities in the ternary can thus be simply calculated from the molar volume and the molar weight.

The density of LiF-BeF$_2$-ThF$_4$ of three compositions with almost constant LiF concentration was measured by Cantor [87]. As shown in Table 5.7, the molar volumes derived from these data are in excellent agreement with those calculated from the pure components.

Viscosity of LiF-BeF$_2$-ThF$_4$

As density, viscosity is also a key parameter for reactor design. Data on the pure components are known, but data on the viscosity of mixtures are scarcer. In this section we investigate ways to estimate the viscosity of a ternary mixture.
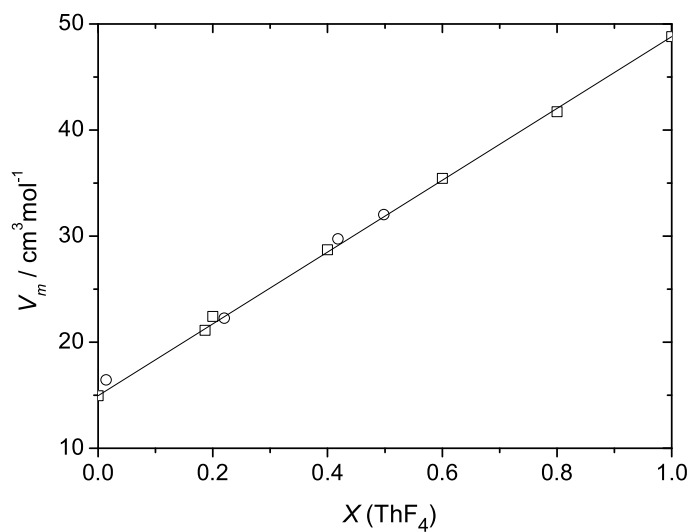
Figure 5.15: The molar volume of liquid LiF-ThF$_4$ at 1273 K; ∘ Porter and

Meaker [88], □ Hill *et al.* [89]; the line represents V_m of the ideal mixture.

Table 5.7: **The molar volumes of three LiF-BeF$_2$-ThF$_4$ mixtures at T = 1073 K: the experimental data from Cantor [87] and the calculated values from the end-members.**

X LiF	X BeF$_2$	X ThF$_4$	$V_{m,exp}$/cm^3· mol^{-1}	$V_{m,cal}$/cm^3· mol^{-1}
0.7011	0.2388	0.0601	20.0	20.0
0.7006	0.1796	0.1198	21.4	21.6
0.6998	0.1499	0.1503	22.4	22.4

The dynamic viscosity of a melt can be related to the Gibbs energy of activation for viscous flow, ΔG^*, by Eq. 5.6.

$$\eta = \frac{\text{Nh}\rho}{M}\exp\left(\frac{\Delta G^*}{\text{R}T}\right) \tag{5.6}$$

where ρ is the density of the melt in kg·m^{-3}, h is Planck's constant, N is Avogadro's number, M is molecular weight in g·mol^{-1}, T is the absolute temperature in K and R is the universal gas constant. Seetharaman *et al.* [90] proposed a method to estimate the viscosity of ternary silicate melts by suggesting that ΔG^* is the sum of the ideal activation energy for viscous flow and the thermodynamic excess Gibbs energy of mixing. We attempted to follow his method for our ternary fluoride system. However, when applying this method to the fluorides, we did not find a good result using the thermodynamical excess Gibbs energy of mixing.

We suggest that the viscosity of a ternary system can be described in a similar way as the thermodynamic properties of the liquid phase in a ternary diagram. Analogously to the thermodynamic Gibbs energy of mixing in a solution phase, which exists of a sum of the Gibbs energy of the pure components and a mixing term, the viscosity can be described as the sum of the activation energy of the pure components (the ideal part) plus an extra term that covers the ideal and the excess mixing part of the activation energy in a multicomponent system, as in Eq. 5.7.

$$\Delta G^* = \Delta_{\text{id}}G^* + \Delta_{\text{ex}}G \tag{5.7}$$

Data on the viscosity of LiF-BeF$_2$ [86, 91] and LiF-ThF$_4$ [92], which are plotted in Figure 5.16, respectively Figure 5.17, were used to derive the excess activation energy terms. For each composition, the viscosity η was given, such that every η is valid for a certain temperature range. By η, defined in Eq. 5.6, the total ΔG^* is known and its T-dependance can be fitted as a first order polynomial '$a + bT$'. So for every composition and temperature, ΔG^* can be calculated. The weighted average of ΔG^* for the pure components is the ideal term $\sum_i X_i \Delta G_i^*$. The extra term in the Gibbs energy of activation for LiF-BeF$_2$ and LiF-ThF$_4$, calculated as the total ΔG^* subtracted by the ideal part, can be described as the Redlich-Kister polynomials in Eq. 5.8, respectively Eq. 5.9. $\Delta_{\text{ex}}G$ is plotted for LiF-BeF$_2$ and LiF-ThF$_4$ in Figure 5.18.
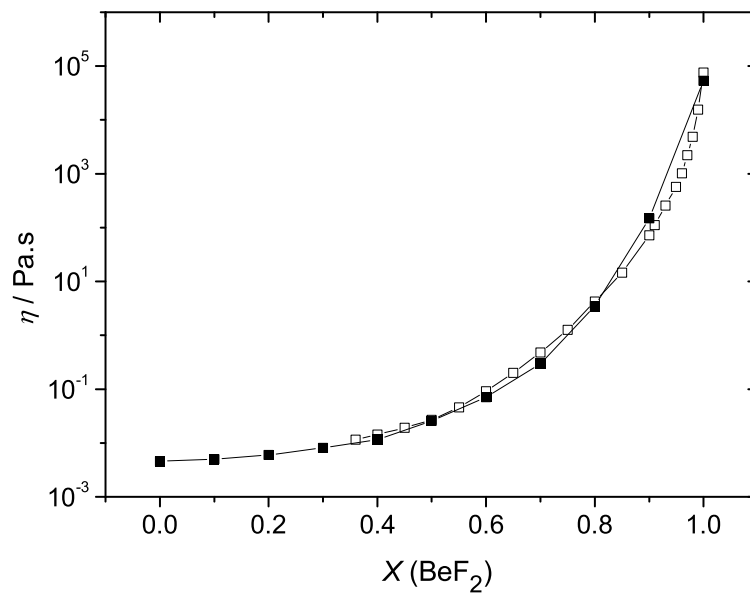
Figure 5.16: The dynamic viscosity of LiF-BeF$_2$ at 873 K by Cantor *et al.* [86]
($\square$) and Desyatnik *et al.* [91] ($\blacksquare$).
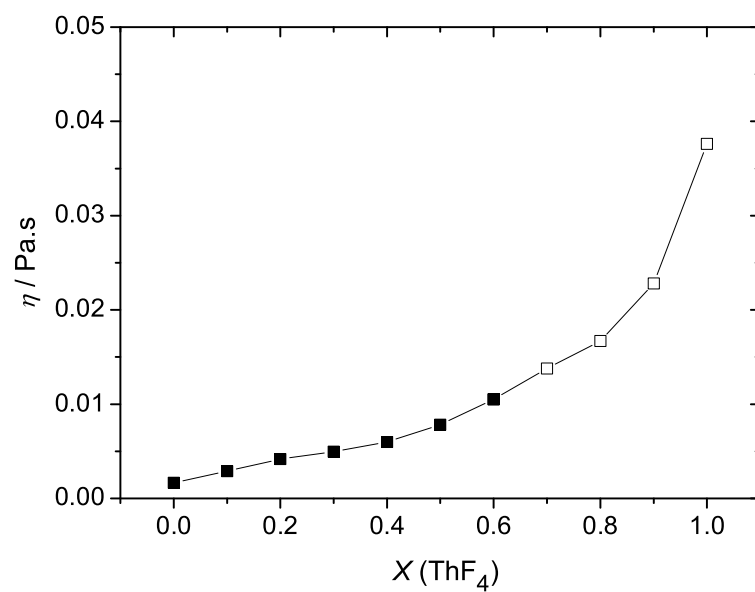
Figure 5.17: The dynamic viscosity of LiF-ThF$_4$ at 1200 K by Chervinskii *et al.* [92]. Open symbols indicate the extrapolation of the viscosity function in the supercooled region.

$$\Delta_{\text{ex}} G^*_{LiF-BeF_2} = X_{BeF_2} X_{LiF} \left(-284015 \cdot X_{BeF_2} * -57618 \cdot X_{LiF} \right) \qquad (5.8)$$

$$\Delta_{\text{ex}} G^*_{LiF-ThF_4} = X_{ThF_4} X_{LiF} \left(-22110 \cdot X_{ThF_4} * +17081 \cdot X_{LiF} \right) \qquad (5.9)$$

The viscosity of BeF_2-ThF_4 is not known. However, we treat the system LiF-BeF_2-ThF_4 as a binary system with xLiF - (1-x)BeF_2 as one and xLiF - (1-x)ThF_4 as the other end-member. Basically, the system is reduced as the sum of pseudobinary systems BeF_2-ThF_4 with a constant molar fraction of LiF. Eqs. 5.8 and 5.9 are substituted in Eq. 5.7 to calculate the activation energy for viscous flow. It should be noted that calculating the ternary viscosity by this way was analogous to the calculation of ternary phase diagrams from the binaries, where one would speak of an asymmetrical extrapolation, with LiF as the asymmetric component, exactly as was done for the LiF-BeF_2-ThF_4 diagram. By using Eq. 5.6, the viscosity of LiF isopleths in LiF-BeF_2-ThF_4 could be calculated. Plotted in Figure 5.19 is the viscosity for BeF_2-ThF_4 at a constant molar fraction of LiF = 0.70, since this is approximately the fraction of LiF in MSBR fuel.

A few data are available for the viscosity in LiF-BeF_2-ThF_4. One data point was reported by MacPherson [93] and three by Cantor *et al.* [49] for X_{LiF} = 0.70. It can be seen that the calculated viscosity follows the trend of the experimental data well. Also the values of model and data are in agreement, considering the uncertainty range of 25 % for the experimental data indicated by Cantor.

However, concise conclusions cannot be drawn from the comparison with four data points. More data are needed to study the viscosity model used here in more detail. To complete the model, we would need viscosity measurements on the binary BeF_2-ThF_4 system and more viscosity data on the ternary system would be desirable as well.

Conclusion on Molten Salt Breeder Fuels

The phase behavior, vapor pressure, density and viscosity of the candidate system for Molten Salt Breeder fuel, LiF-BeF_2-ThF_4 have been calculated. A
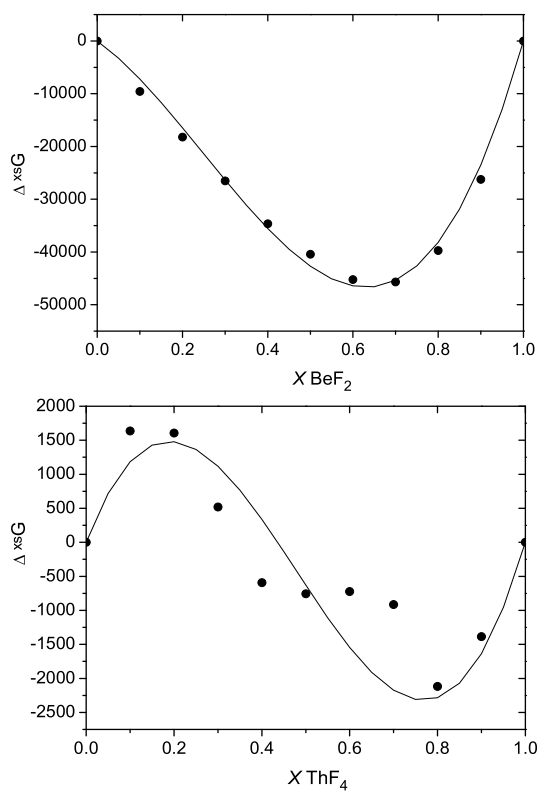
Figure 5.18: The excess activation energy for viscous flow for LiF-BeF$_2$ and LiF-ThF$_4$, fitted with a Redlich-Kister polynomial.
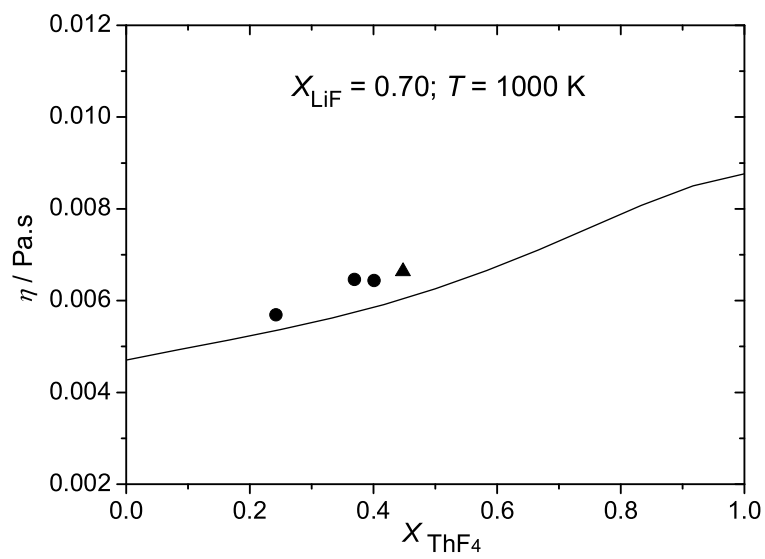
Figure 5.19: The pseudobinary ThF_4-BeF_2 viscosity diagram at 1000 K; at a constant molar fraction of LiF $= 0.70$. ▲ MacPherson [93]; ● Cantor *et al.* [49].

typical composition is 0.717 LiF - 0.16 BeF$_2$ - 0.12 ThF$_4$ - 0.003 UF$_4$, which is in this case simplified to 0.717 LiF - 0.16 BeF$_2$ - 0.123 ThF$_4$. The temperature of fusion, according to our calculated phase diagram, is 794.5 K, which is in agreement, but slightly higher than the 773 $\pm$ 5 K, reported by Cantor [49].

The vapor pressure of this composition at the operating temperature of a MSR (750-900 K) is low, namely between 10^{-8} and 10^{-6} bar. It is fully dictated by the partial vapor pressure of BeF$_2$.

A linear relationship exists between the density of the pure molten fluoride components and the density of a liquid mixture. The density of MSR fuel could therefore be calculated as the weighted average from the densities of liquid LiF, BeF$_2$ and ThF$_4$. The calculated and the experimental values were in perfect agreement: 21.6, respectively 21.4 cm$^3 \cdot$mol^{-1}.

The dynamic viscosity of a molten fluoride mixture can be calculated from the activation energy for viscous flow. This consists, analogously to the thermodynamic Gibbs energy of mixing, of an ideal and an excess part. The excess activation energy was derived from the viscosity data on LiF-BeF$_2$ and LiF-ThF$_4$ and was described as Redlich-Kister polynomials. The viscosity of LiF-BeF$_2$-ThF$_4$ at a constant molar fraction of LiF = 0.70 was calculated and compared to the few data available. It appeared that the values and the trend of the model and data were in agreement. The calculated viscosity of MSBR fuel is 6.0$\cdot 10^{-3}$ Pa$\cdot$s to 6.6$\cdot 10^{-3}$ Pa$\cdot$s reported by ORNL researchers. However, the number of data are too scarce to draw conclusions. More data on binary and ternary systems are needed for a better understanding of viscous flow in molten fluorides.

Chapter 6

Outlook

Which goals have been reached in this PhD study? To summarize it briefly, two fuel types for the Molten Salt Reactor were thermochemically investigated, including thermodynamic assessment and the performance of some experiments, resulting in the creation of an internally consistent thermodynamical database.

How should we see this thesis in the framework of the Molten Salt Reactor programme? In my opinion, this thermodynamic study gives a contribution to the MSR, although it is small. I do not have the illusion that the reactor has been basically improved or will be deployable years earlier. This work was merely pioneering, or at least for a part. A tool to evaluate binary systems and to extrapolate the results in order to calculate multi-order phase diagrams was developed with good results. The method used, which is also called the CALPHAD method, is not new, but it was the first time it was applied to MSR fuel compositions. Another new aspect was the including of some physicochemical parameters that are important for the reactor design in the model.

This Chapter discusses the, to my opinion, most important aspects of this thesis.

Calorimetric experiments on intermediate compounds

After successfully testing the new Setaram Multi-HTC calorimeter with NaF, experiments on the intermediate compound $NaLaF_4$ were performed. This was the first intermediate compound that was synthesized and calorimetrically analyzed in this PhD study.

In many binary systems that were studied, especially LiF-ThF_4 and LiF-UF_4, a considerable number of intermediate compounds is present. Thermodynamic data are most of the time not available for them, like the standard enthalpy and entropy of formation and/or the heat capacity. This implies that these values need to be optimized in the assessment, together with the coefficients for the excess Gibbs energy for the solution phase. The paradox is now, that having more thermodynamical information on the compounds, makes it in general more difficult to obtain a satisfactory fit of the phase diagram with the model. The reason is that a number of degrees of freedom is lost, when a number of parameters for an intermediate compound is fixed, so that the model is left less possibilities to produce a proper fit. This was illustrated by the reassessment of NaF-LaF_3 in Chapter 4, using the newly obtained calorimetric data for $NaLaF_4$, which is the single intermediate compound in that system. The fit before including the new data was better than the fit after.

However, since it was not our goal just to reproduce the smoothest phase diagrams using optimized coefficients, but to create an internally consistent thermodynamic database, more calorimetric experiments ought to be performed. Most interesting would be, of course, to carry out experiments on active compounds, especially on $M_nAn_mF_{n+4m}$ (with M=Li, Na and An= Th, U). But to analyze active materials, it is from utmost importance that the containment is not leaking. This was a little problem with the boron nitride crucibles, which we used for the synthesis and analysis of inactive $NaLaF_4$. Boron nitride has an excellent chemical resistance, but the crucibles could not be closed tightly. Even with a screwed cap, as we used them for the thermal analysis in the Netzsch STA 449C Jupiter, the containers always leaked a bit. At the moment of finishing this thesis, we are testing crucibles with a screwed cap that are made from Shapal (aluminumboron nitride), a machinable ceramic with high thermal conductivity. They are more robust than boron nitride crucibles and chemically resistent against molten fluorides as well. The first results are promising and we expect a successful continuation of the calorimetric work on active fluorides.

Thermal experiments and the analytical error

Differential Thermal Analysis was used to measure phase diagrams, which is a straightforward technique, but in the meanwhile, some difficulties raised during the interpretation of the diagrams. The invariant events are usually clearly marked. The eutectic and peritectic(s), if present, are the beginnings of the formation of a melt, which is indicated by a sharp peak in the heating curve. The problem lies in interpreting the peaks that correspond to the liquidus. Usually, a little cusp marks the end of the melting, but this is sometimes difficult to discern. The peak is clearer present in the cooling curve, but we decided not to use the cooling curve because of the supercooling effects that take place; even when the rate of cooling is programmed the same as the rate of heating.

Unfortunately, the majority of the experimental phase diagram in the literature are obtained by the interpretation of cooling curves or by quenching. We can almost be certain that differences exist between the values we found in the literature and those we would have obtained if we had performed the experiments ourselves, but we do not know exactly till what extent. It would make sense to remeasure a couple of known phase diagrams, at least the ones of the key systems.

In this study, an excellent example of how the results of the experiments influence the model is found in Chapter 4, *MSR Burner Fuels.* The thermodynamic model for LiF-NaF-LaF$_3$ was based first on the extrapolation of the binaries, which were assessed using literature data only. However, after comparing the model to the results of the DTA experiments on ternary samples, it appeared that the difference between the experimental data and the calculated liquidus values was unacceptably large. The model calculated consequently lower values than the experimental ternary liquidus data. We decided to partly remeasure the LiF-LaF$_3$ and NaF-LaF$_3$ diagrams and found a good agreement with the reported invariant values, but a significant difference with the binary liquidus data from the literature. A renewed assessment of the binaries using our own experimental data, followed by the extrapolation to the ternary diagram, resulted in a much better agreement between model and experiments.

This brings us to the difference between our own DTA experimental data and the two thermodynamic models, as discussed in Chapter 4. At the moment the deviation of both models from the data is 3% or smaller. Is 3% satisfying enough? For low temperatures, it is reasonable, but for high temperatures, the absolute difference becomes significant. How should this deviation be split

in an error of analysis, to which the error in the temperature measurement and the error in weighing and mixing contribute, and the error in the model? And is there a way to improve it?

Was the weighing and mixing of the samples good enough? The precision of the balance was 0.1 mg. Usually, about 100 mg of a mixture was prepared, of which a sample was taken for analysis. When duplex samples were measured -this means that two times a sample was taken from the same prepared mixture-, the eutectic temperature varied normally within 1 K, while the peritectic showed a 3 K spreading. Since these are invariant points, the melting temperature should always be the same, even if the composition is slightly different. Since we speak about melting temperatures between 850 and 900 K, the error is smaller than 0.5 %. Also in the case when all measurements are taken into account, the deviation in the eutectic temperature is smaller than 0.6 % and in the peritectic smaller than 0.9 %. We can conclude that the machine itself is rather precise.

However, when measuring the liquidus, which is much more difficult to determine, the difference between duplex analyses could be 5 to even 25 K. For the comparison with the model, the average value was taken in these cases. This would correspond -assuming that the equipment has almost the same precision at higher temperatures- to a composition difference of a few percents, which is also dependent on the slope of the liquidus. When the slope is steep, a small change in composition has a large influence on the temperature.

If the thermodynamic model would systematically differ from the experiments, one would expect a trend-wise deviation pattern. Since this is not the case -the pattern is scattered- we do not think that using another model will make the difference between model and experiments smaller. Although care was taken to mix the samples as well as possible, improvements are possibly achieved by better mixing. We could in the future probably work with finer powders. When this analytical error is more or less ruled out, it leaves us the error in the interpretation of the DTA spectrum.

It could be interesting to carry out a campaign to systematically mix and measure some samples a couple of times, for an improved error evaluation.

The need of another model?

The way of extrapolation of the excess coefficients to the ternary system can have a huge influence on the result. This was especially shown in the LiF-BeF$_2$-ThF$_4$ example in Chapter 5. The choice between LiF or BeF$_2$ as the asymmetric component was quite crucial. At the moment it is not possible to fine-tune the weight of a component in a multi-component system. A component is now placed in either group 1 or group 2. Especially LiF, as a component with an extremely ionic behavior, having a very small cation compared to many other cations, should be treated in a different way. It would therefore be interesting to develop or to collaborate in the development of a model in which the weight of the components in the extrapolation can be adjusted.

The quasi-chemical model with quadruplets has more possibilities than the simple quasi-chemical model and has also more physical sense. However, some input parameters are used, which we would like to verify, because we were using some default numbers at the moment, due to lack of information. For example the coordination numbers of the cations and anions and also the ratio of the numbers of first nearest neighbors to second nearest neighbors are taken by default. More knowledge on the structure in a fluoride melt, by performing some Raman or IR experiments, would be helpful in this case.

The influence of fission products

An often heard question at seminars and conferences was: "What will happen when, after a while, fission products enter your well-defined fuel plus solvent system?"

Although the MSR is designed such that the salt is chemically reprocessed in a continuous way, it is imaginable that a small percentage of fission products will accumulate in the salt mixture. The effect of fission products has not been studied in this thesis, but it would be worth it to investigate how the eutectic will be influenced in temperature and composition by including a few percents of some elements that represent the group of fission products. Because there are so many different fission products with various chemical properties, it will be rather complicated to select a couple of them to include in the model.

Basically there are four groups of fission products. The volatiles, mainly krypton and xenon, will probably increase the vapor pressure, but can also be

easily removed by the off-gas system. There is the group of noble metals that
will not dissolve in the matrix, but will most likely precipitate and therefore
be easy to remove as well. Fission products that belong to this group are
molybdenum, technetium, ruthenium, rhodium and palladium. Some of the
fission products, on the other hand, will dissolve in the matrix and are ex-
pected to increase the temperature of the melt (yttrium, barium, lanthanide
fluorides). However, they can be extracted by various separation techniques.
The last group of fission products contains the elements that dissolve in the
matrix and are hardly extractable, which will therefore accumulate in the salt
mixture. These will be mainly cesium and zirconium (as CsF and ZrF_4, which
is known as a melting point lowering component). Usually, iodine is a volatile
element, but in this case it is likely to dissolve as I^- in the fuel lattice. It is
hard to predict the exact influence on the eutectic temperature, but the small
additions of fission products might have a melting point lowering effect in the
end.

Collaboration with Partitioning & Transmutation

A substantial part of the fission products in spent fuel originating from or-
dinary PWR and BWR reactors are the lanthanides that behave chemically
rather similar to the actinides, which make up the most radiotoxic part of the
waste. For storage reasons, it is important that the most active part is iso-
lated. It can be stored separately, or be transmuted in, for example, a Molten
Salt burner Reactor, where is serves as fuel. Also MSR burner fuel itself would
need to be reprocessed to remove the fission products.

Separation chemists at CEA, CNRS and EdF have studied the reprocessing
of MSR fuel, based on the ORNL experience. The main technique proposed
is liquid-liquid extraction using the fluoride salt in combination with a liquid
metal. In this process, the separation efficiency depends on the activity coef-
ficients in the salt and metal phase. This is a highly interesting topic, where
experiments and thermodynamic modelling could interact and complete each
other. At ITU there has been already some collaboration between the separa-
tion chemists and the fuel modellers, but it could be intensified in the future.
There is a lot of experimental know-how from the pyrochemistry side; how to
cope with aggressive molten salts at high temperatures. The thermodynamists
on the other hand, could supply the modelling support.

Also in a larger scope, namely for the development of the Molten Salt Re-

actor, could it be very interesting to set up a common project. Research on both topics could interact and be streamlined, so that both groups work more efficiently to the end goal: a fuel that can be reprocessed in the most efficient and economic way.

Other physical parameters

A start was made in this thesis to investigate other physical properties that are important for the reactor design. In Chapter 5, the vapor pressure, density and viscosity were studied. It is already foreseen to install a viscometer at ITU next year, especially dedicated to molten salts. In this way, the viscosity can be further investigated, with emphasis on the analogy between thermodynamics and viscosity. The asymmetric approach to calculate ternary viscosity worked well and it would be interesting to expand and improve the viscosity model by experimental data. Next to this, more knowledge on the thermal conductivity of some compositions of interest would complete the thermo-physicochemical model of molten fluoride salts.

Structural materials

The difficulties encountered by finding proper container materials for the thermal and calorimetric experiments, makes one realize that the challenge of finding proper structural materials is enormous. Boron nitride appeared to be very appropriate for -inactive- experiments, but it cannot be used as cladding in a reactor, because boron is a neutron poison. Tests, where some LiF and NaF was molten in platinum and pure nickel crucibles, showed that the surface of both containers was etched afterwards. The temperatures reached here were higher than the operating temperature in a reactor would be. These materials might be usable, but platinum would probably be too expense anyway. Hope is also set on the use of carbon composites, although carbon is known to have poor thermal and mechanical properties in a neutron environment. This is a reason not to use it in a fusion reactor, where the neutron flux will be extremely high. However, the flux in a MSR will be much lower, so that carbon composites might be used in the future. But MSR designers will probably come back to "old boy" Hastelloy. However, to meet the demands of the Generation IV programme, improvements have to be made to make it

more resistant at higher temperatures. Some problems encountered during the Molten Salt Reactor Experiment, were the embrittlement by helium and the microcracking caused by tellurium. At the moment, Škoda in the Czech Republic is developing MONICR, a nickel alloy with promising corrosion resistance properties. At the Kurchatov Institute of the Russian Research Centre, a modified Hastelloy alloy was developed and tested, the so-called HN80MTY, which contains more titanium and aluminum than Hastelloy N, the material used in the Oak Ridge experiments. The tests proved that the corrosion resistance is higher than for Hastelloy N and that working temperatures can be up to 750 ^{O}C. The maximum operating temperature aimed for in the Generation IV programme is about 700, but preferably 800 ^{O}C, so this alloy is a step in the right direction.

Samenvatting in het Nederlands (Summary in Dutch)

Samenvatting - Inleiding

Generatie IV - nucleaire systemen van de toekomst

Het Generatie IV initiatief behelst zes reactorconcepten voor de toekomst. Momenteel behoort het merendeel van de huidige reactoren tot de tweede generatie. Derde generatie reactoren, die belangrijke verbeteringen ten aanzien van veiligheid en efficiëntie hebben, zullen in de nabije toekomst een deel van de huidige vloot vervangen. Ze worden gezien als de tussenstap op weg naar de vierde generatie.

Het Generatie IV Internationale Forum, waaraan negen landen plus Euratom deelnemen, is overeengekomen dat Generatie IV systemen duurzaam, veilig en economisch zijn, een minimum aan nucleair afval produceren en bovendien de verspreiding van nucleair materiaal, waar mogelijkerwijs wapens van gemaakt

zouden kunnen worden, tegengaat. Samen met drie typen snelle reactoren, een zeer hoge temperatuur reactor en een superkritisch water-gekoelde reactor, is de Gesmolten Zout Reactor uitgekozen voor verdere ontwikkeling. Het zal echter nog enige tijd duren voordat die daadwerkelijk operatief zijn, de eersten zullen pas rond 2030 werken.

De Gesmolten Zout Reactor

Het concept van de Gesmolten Zout Reactor (Molten Salt Reactor, MSR) bestaat uit het feit dat de brandstof, een splijtbaar materiaal, in een gesmolten zout is opgelost en door een gesloten circuit gaat. De warmte van de splijtingsreactie wordt afgevoerd door hetzelfde zout en overgedragen aan een tweede gesmolten zout circuit, waarvan de warmte de generator en turbines aandrijft, die uiteindelijk electriciteit produceren. Het zout wordt regelmatig gezuiverd en de brandstof ververst. Dit gebeurt ter plaatse, zonder dat de reactorcyclus onderbroken hoeft te worden. Hierdoor kan, in theorie, een zeer hoge opbrand worden bereikt. Andere voordelen zijn, vanwege de hoge temperatuur van het zout, de efficiënte energieproductie, en de kleine hoeveelheid splijtbaar materiaal, dat nodig is om de cyclus te starten. De reactor wordt gemodereerd door grafiet staven. De typische inlaat en uitlaat temperaturen zijn 565 $^\mathrm{O}$C, respectieveljk 700 $^\mathrm{O}$C.

Dit concept is niet geheel nieuw, aangezien in de Verenigde Staten het onderzoek aan een nucleaire reactor met gesmolten zout reeds uit de jaren vijftig dateert. Men begon met een ontwerp voor een op nucleaire energie aangedreven vliegtuig, met een circulerend gesmolten fluoride zout als brandstof. Dit werd het ARE (Aircraft Reactor Experiment) project genoemd. Wat later werd de nadruk gelegd op de ontwikkeling van een reactor, die op hetzelfde principe berustte, voor civiele doeleinden. Gesmolten fluoride zouten werden uitgekozen, omdat hun eigenschappen aan vrijwel alle gestelde eisen voldoen. Het betreffende zout behoort [4]:

- een groot oplossend vermogen te hebben voor thorium en uraan,

- thermisch stabiel te zijn tot bij hoge temperaturen,

- ongevoelig te zijn voor radiolyse,

- een lage dampdruk te hebben bij de temperaturen waarbij de reactor werkt,

- compatibel te zijn met de nikkel legeringen (Ni-Mo-Cr-Fe) die als constructie materiaal gebruikt kunnen worden (Hastelloy).

Het Gesmolten Zout Reactor Experiment (Molten Salt Reactor Experiment, MSRE) was een intensief onderzoeksprogramma naar de eigenschappen van gesmolten fluoride zouten in de jaren zestig in Oak Ridge National Laboratory. In het algemeen was de brandstof gesmolten UF_4 en/of ThF_4, opgelost in een mengsel van ZrF_4, NaF, LiF and BeF_2, met diverse samenstellingen.

De financiële ondersteuning in de Verenigde Staten voor de Gesmolten Zout Reactor werd in 1975 opgezegd. De fluoride zouten zijn echter weer in de belangstelling komen te staan sinds de jaren negentig, in het kader van de Partitionering en Transmutatie en Generatie IV programma's.

De Gesmolten Zout Reactor kan voor twee doeleinden worden gebruikt. Aan de ene kant kan het fungeren als een nucleaire afvalverbrander met uraan, plutonium of andere actiniden als brandstof. Een oplosmiddel bestaande uit LiF-NaF wordt dan gebruikt, omdat dit type zout een hoog oplossend vermogen voor actiniden heeft. Aan de andere kant kan de MSR ook ontworpen worden als een broeder op basis van de ^{232}Th/^{233}U cyclus. In dat geval wordt een kleine hoeveelheid uraan of plutonium gebruikt om de reactor te starten, om het splijtbare ^{233}U uit ^{232}Th, dat een fertiel materiaal is, te produceren. Het is aangetoond dat, om aan een optimale neutronenbalans en aan andere fysisch-chemische voorwaarden te voldoen, een samenstelling van hoofdzakelijk ^{7}LiF-BeF_2 de beste matrix is om de brandstof in op te lossen.

Thermodynamisch modelleren van fluorides

Kennis ten aanzien van de thermodynamische eigenschappen van het fluoride zout is zeer belangrijk voor het ontwerp van de reactor. Echter, er zijn onnoemelijk veel mogelijke samenstellingen voor de brandstof en het oplosmiddel en het zou ondoenlijk zijn om van allemaal de eigenschappen te meten. Het doel van dit promotieonderzoek was om de chemische systemen van diverse zoutsamenstellingen van belang thermodynamisch te evalueren met behulp van het software pakket van FactSage [31], en waar mogelijk, experimentele data om de thermodynamische modelleren te testen en te verbeteren aan te leveren.

De evaluatie van een systeem houdt in dat bekende thermodynamische data,

zoals de warmte capaciteit, de vormingsenthalpie en -entropie van een stof van belang, worden verzameld en zorgvuldig geselecteerd. Extra informatie wordt toegevoegd in de vorm van beschikbare experimentele data, zowel uit de literatuur, als uit eigen werk. Deze gegevens worden gebruikt om de onbekende data te optimaliseren; meestal gaat dit om de zogeheten exces Gibbs energie parameters, die de vorm van een fasendiagram definiëren. Het resultaat is dat een complete, intern consistente thermodynamische databank wordt verkregen. Met behulp hiervan kunnen fasendiagrammen berekend worden en kan het fasengedrag in een bepaald temperatuurbereik worden voorspeld.

Om de exces Gibbs coëfficiënten van een binair systeem voldoende nauwkeurig en met een minimum aan parameters te beschrijven, is het quasi-chemisch model, dat gebruik maakt van een beschrijving met algemene polynomen [30], zeer bruikbaar. De ge-optimaliseerde parameters van de binaire systemen kunnen naar multi-componenten systemen worden ge-extrapoleerd, zodat dat ook hiervan de fasendiagrammen berekend kunnen worden. Naast deze, min of meer, mathematische beschrijving, bestaan er ook andere modellen, die in meerdere mate een fysische betekenis hebben. Een voorbeeld hiervan is uitgewerkt in dit proefschrift.

Uit het oogpunt van de reactorfysica is het tevens interessant om fysisch-chemische eigenschappen, zoals dampdruk, molair volume en viskositeit, in één consistent model op te nemen. Dit maakt het mogelijk om preciezere voorspellingen te doen over het gedrag van het gesmolten zout in een werkende reactor.

Dit proefschrift

Hoofdstuk 1 geeft een algemene inleiding in de kernenergie, waarin de principes van kernsplitsing en een kernreactor worden uitgelegd. Daarnaast wordt de ontwikkeling van de eerste onderzoeksreactoren tot aan de geavanceerde reactoren van de toekomst, Generatie IV, beschreven. In dit Hoofdstuk worden ook het concept en de voordelen van de Gesmolten Zout Reactor uiteengezet. Tevens wordt zijn geschiedenis van test reactor in het Oak Ridge Nationaal Laboratorium tot aan het geavanceerde ontwerp in het Generatie IV programma uiteengezet.

In Hoofdstuk 2 wordt de techniek om de warmte capaciteit van een stof te meten uitgelegd. Om de nieuwe Differential Scanning heat flux calorimeter te

testen, die speciaal ontworpen is om de warmte capaciteit bij hoge temperaturen (vanaf ongeveer 600 tot maximaal 1673 K) te meten, werd NaF gebruikt. Nadat een goede overeenstemming tussen onze warmte capaciteitsdata en de waarden uit de literatuur was vastgesteld, werd $NaLaF_4$ gesynthetiseerd en gemeten. Daarnaast werd de warmte capaciteit van $NaLaF_4$ bij lage temperaturen (10 tot 300 K) gemeten met behulp van adiabatische calorimetrie. De twee data reeksen sloten mooi op elkaar aan, waarmee een nauwkeurige beschrijving werd gegeven van de thermische functies van deze compound.

De oplosmiddelen voor MSR brandstof staan centraal in Hoofdstuk 3. Uitleg wordt gegeven over de thermodynamische evaluatie van binaire systemen met behulp van een polynomische beschrijving. Vier verschillende samenstellingen werden bestudeerd; te weten $LiF-BeF_2$, $NaF-BeF_2$, $LiF-NaF$ en $NaF-ZrF_4$. Kleine ontmenggebieden in de vloeistof in het BeF_2-rijke gebied van de eerste twee systemen werden waargenomen in het model, die echter geen invloed hebben op het oplossend vermogen. $^7LiF-BeF_2$ staat bekend als het best mogelijke oplosmiddel voor MSR brandstof, wanneer die als broeder wordt toegepast. ^7Li produceert echter tritium na neutronenvangst in de reactor en dat is zeer ongewenst. Een gedeeltelijke substitutie van LiF door NaF zou het enigszins kunnen verhelpen. Helaas zijn de data voor het $NaF-BeF_2$ systeem zeer schaars en het resultaat van de evaluatie, het binaire fasendiagram, was niet goed genoeg om het verder mee te nemen in een model voor, bijvoorbeeld, $LiF-NaF-BeF_2$. $LiF-NaF$ en $NaF-ZrF_4$ zijn beide voorgesteld als oplosmiddelen voor de brandstof voor de MSR als afvalverbrander. Echter, de dampdruk van $NaF-ZrF_4$ werd berekend voor de typische werktemperaturen en bleek tamelijk, en wellicht te hoog.

Hoofdstuk 4 behandelt de brandstofsamenstellingen voor de MSR als afvalverbander. Twee verschillende thermodynamische modellen werden toegepast en vergeleken. Om de modellen te testen en te verbeteren, werden Differentiële Thermische Analyse (Differential Thermal Analysis, DTA) experimenten uitgevoerd. De ternaire $LiF-NaF-MF_3$ (M=La, Ce, Pu) systemen werden bestudeerd, met LaF_3 en CeF_3 als inactieve vervangingen voor de brandstof PuF_3. Een (bijna-) eutektische samenstelling van $LiF-NaF-PuF_3$ wordt namelijk beschouwd als een MSR brandstof kandidaat. De overeenstemming tussen de resultaten van de DTA experimenten aan de inactieve monsters en de modellen was goed. Analoog aan de systemen met LaF_3 en CeF_3, werd het $LiF-NaF-PuF_3$ fasendiagram berekend. De conclusie was dat de eutektische temperatuur, die de minimumtemperatuur in een werkende reactor bepaald, waarschijnlijk aan de hoge kant was, vergeleken met de huidige reactorontwerpen. RbF, als een smeltpuntsverlagende stof, werd om deze re-

den toegevoegd aan het LiF-NaF-LaF$_3$ model. Het resultaat voorspelt een significante daling in de eutektische temperatuur door de toevoeging van een kleine hoeveelheid RbF.

In Hoofdstuk 5 wordt de brandstof voor de MSR als broeder bestudeerd. Een thermodynamisch model voor LiF-BeF$_2$-ThF$_4$-UF$_4$ werd ontwikkeld en getest aan de hand van experimentele data van ORNL onderzoekers, met een naar tevredenheid stemmend resultaat. Tevens werden andere fysisch-chemische eigenschappen bestudeerd, die belangrijk zijn voor het reactorontwerp, namelijk dampdruk, dichtheid en viskositeit. De dampdruk werd berekend aan de hand van hetzelfde thermodynamisch model en het resultaat kwam mooi overeen met de beschikbare experimentele data. Dichtheid, oftewel molair volume, volgt ideaal gedrag. Dit houdt in dat de dichtheid van een mengsel de proportionele som is van de dichtheid van de zuivere componenten. De dynamische viskositeit kan worden berekend uit de activatie energie voor viskeuse stroming. Er werd verondersteld dat deze uit een ideaal en een exces gedeelte bestaat, geheel analoog aan de thermodynamische Gibbs energie van menging. Deze methode bleek goed te werken. Het resultaat was in overeenstemming met de paar beschikbare data, hoewel substantieel meer data nodig zijn om viskeuse stroming in gesmolten fluorides beter te begrijpen.

Hoofdstuk 6 geeft een synthese van het proefschrift en bediscussieert de mogelijkheden voor een succesvolle voortzetting van deze studie en de implicaties voor de Gesmolten Zout Reactor.

Summary (in English)

Summary - Introduction

Generation IV - nuclear systems of the future

The Generation IV initiative comprises the concepts of six reactor systems of the future. At present, the majority of the current reactors belong to the second generation. Third generation reactors, which have important improvements regarding safety and efficiency compared to the second generation, are foreseen to replace part of the nuclear fleet in the near future. They are also seen as the intermediate step towards the fourth generation.

It is agreed by the Generation IV International Forum, in which nine countries and Euratom take a seat, that Generation IV systems should be: sustainable, safe, economic and should produce a minimum of nuclear waste and prohibit the proliferation of potential weapons-grade nuclear material. Together with three fast reactors, a very high temperature reactor and a supercritical water-cooled reactor, the Molten Salt Reactor (MSR) was selected to be developed further. However, they will not be deployable in the near future; the first of them are planned to be operating around 2030.

Molten Salt Reactor

The concept of the Molten Salt Reactor is that the fuel, a fissile material, which is dissolved in a molten salt, circulates through a closed circuit. The heat of fission is transferred to a second molten salt coolant loop, the heat of which drives the generator and turbines to produce electricity. The salt is periodically purified and refuelled on-site, without interrupting the reactor cycle, so that very high burn-ups can be reached, theoretically. Other advantages are the efficient power production, because of the high temperature of the salt and the small fissile inventory that is needed to start the cycle. The reactor is moderated by graphite rods. Typical inlet and outlet temperatures that are aimed for are about 565 ^{O}C, respectively 700 ^{O}C.

This concept is not entirely novel, since the research on a nuclear reactor using molten salt fuel started already in the early fifties in the USA. First, there was the design of a nuclear-powered aircraft, using a circulating molten fluoride salt as fuel, which was the so-called ARE project. Later, the emphasis moved to the development of a civilian power reactor based on the same principle.

Molten fluoride salts were chosen, because their properties answer most of the requirements. The salt mixture should be [4]:

- soluble over a wide range for thorium and uranium,

- thermally stable up to high temperatures,

- stable to radiation (no radiolytic decomposition),

- exhibiting a low vapour pressure at the operating temperature of the reactor,

- compatible with nickel-based alloys (Ni-Mo-Cr-Fe) that can be used as structural materials (Hastelloy).

An intensive research programme was performed on molten fluoride salt systems in the Molten Salt Reactor Experiment (MSRE) at the Oak Ridge National Laboratory during the 1960's. The molten salt fuels were based in general on UF_4 and/or ThF_4 kept in solution in a mixture of ZrF_4, NaF, LiF and BeF_2 in different amounts.

In the USA, the support for the Molten Salt Reactor ceased in 1975. However, the fluoride salts have become subject to renewed interest since 1990 in the

frame of the Partitioning and Transmutation (P&T) and the Generation IV programmes.

Two approaches are being studied since this time. The Molten Salt Reactor can be used as a burner of actinides using uranium and/or plutonium or other minor actinides as a fuel. A LiF-NaF based solvent is to be used then, because of the high solubility of actinides in this type of salt mixture. On the other hand, the MSR can also be designed as a breeder based on the ^{232}Th/^{233}U cycle. In that case, a small amount of uranium or plutonium is used to start up the reactor to produce fissile ^{233}U from ^{232}Th, which is fertile. To obtain an optimum neutron balance and also to meet other important thermal and physicochemical demands, a composition of mainly ^{7}LiF-BeF$_2$ has been proved to be the most viable matrix for the fuel to dissolve in.

Thermodynamic modelling of fluorides

Knowledge of the thermodynamic properties of the fluoride salt mixtures is of major importance for the reactor design. But there are innumerable possible compositions and it would be impossible to measure the properties of all of them. The aim of this PhD project was to assess the chemical systems of various salt compositions of interest thermodynamically with aid of the software package of FactSage [31] and where possible, to provide experimental data to test and improve the thermodynamic models.

Assessing a system means that known thermodynamical data, like the heat capacity function, the enthalpy and entropy of formation of the components of interest are collected and carefully selected. Extra information is added in the form of available experimental data, from literature as well as from own work. These data are used to optimize the unknown data, which are most of the time the excess Gibbs energy parameters. They are necessary to define the shape of a phase diagram. As a result, a complete internally consistent thermodynamic database is obtained. From this database, phase diagrams can be calculated and phase behavior in a given temperature range can be predicted.

To describe the excess Gibbs coefficients of a binary system in a satisfactory way and with a minimum of parameters, the quasi-chemical model that makes use of a general polynomial description [30] has been proved to be very useful. The optimized parameters of binary systems can be extrapolated to multicom-

ponent systems, so that the phase diagrams of these systems can be calculated as well. Besides this more or less mathematical description, other models that give more physical sense exist as well, of which an example has been worked out in this thesis.

In addition, it is interesting from the point of view of reactor physics, to include physicochemical properties, such as vapor pressure, molar volume and viscosity, in one, consistent model. This will enable us to make more precise predictions on the behavior of the molten salt in an operating reactor.

This thesis

Chapter 1 gives a general introduction in nuclear energy, where the principles of nuclear fission and a nuclear reactor are explained. Further, the development of the first research reactors to the advanced reactors of the future, Generation IV, is described. In this Chapter, the concept and advantages of the Molten Salt Reactor are explained. Its history is given, from the test reactor in Oak Ridge National Laboratory, till the advanced design in the Generation IV programme.

In Chapter 2, the technique to measure the heat capacity of a substance is explained. NaF was used to test the new equipment of the Differential Scanning heat flux calorimeter, which is especially designed to measure high temperature heat capacities (from about 600 till 1673 K maximum). After finding a good agreement between our heat capacity data and the values known from literature, $NaLaF_4$ was synthesized and measured. In addition, the low temperature heat capacity of $NaLaF_4$ (10 to 300 K) was measured using adiabatic calorimetry. The two series fitted smoothly, thus describing the thermal functions of this compound accurately.

The solvents for the MSR fuel are central in Chapter 3. The thermodynamic assessment of binary systems, using the polynomial description, is explained. Four different solvent compositions were studied; these were LiF-BeF_2, NaF-BeF_2, LiF-NaF and NaF-ZrF_4. In the model, small miscibility gaps in the liquid in the BeF_2 rich part of the first two binaries appeared, which have, however, no influence on the solving capacities. [7]LiF-BeF_2 is known as the best possible solvent for MSR breeder fuel. A partial substitution of LiF by NaF could help to prevent the tritium production by [7]Li. Data on the NaF-BeF_2 system are very scarce and the result of the assessment, the binary phase

diagram, was not good enough to include it in a model for, for example, LiF-NaF-BeF$_2$. LiF-NaF and NaF-ZrF$_4$ have both been proposed as solvents for MSR burner fuel. The vapor pressure of NaF-ZrF$_4$ was calculated for typical operating temperatures and appeared to be rather high.

Chapter 4 deals with the fuel compositions for the MSR as waste burner. In this Chapter, two different thermodynamic models were used and compared. Differential Thermal Analysis experiments were performed to test and improve the models. The ternary LiF-NaF-MF$_3$ (M=La, Ce, Pu) systems were studied, with LaF$_3$ and CeF$_3$ as inactive proxies for the fuel PuF$_3$. A (near-) eutectic composition of LiF-NaF-PuF$_3$ is considered as a MSR fuel candidate. The agreement between the results of the DTA experiments on the inactive samples and the models was good. Analogously to the systems with LaF$_3$ and CeF$_3$, the LiF-NaF-PuF$_3$ phase diagram was calculated. It was concluded that the temperature of the eutectic, which defines the minimum temperature in an operating reactor, is probably a bit too high, when compared to the current designs. RbF, as a melting point lowering component, was added to the LiF-NaF-LaF$_3$ model. The result predicts a significant lowering in the eutectic temperature by adding a small amount of RbF.

In Chapter 5, the fuel for the MSR as breeder is studied. A thermodynamic model for LiF-BeF$_2$-ThF$_4$-UF$_4$ was developed and tested with experimental data from ORNL researchers, with a good agreement. Moreover, other physicochemical properties that are important for the reactor design were studied, and these were vapor pressure, density and viscosity. The vapor pressure was calculated from the same thermodynamic model and agreed nicely with the experimental data available for this system. Density, or molar volume, follows ideal behavior. This means that the density of a mixture is the proportional sum of the density of the pure components. The dynamic viscosity can be calculated from the activation energy for viscous flow. It was assumed that this consists, analogous to the thermodynamic Gibbs energy of mixing, of an ideal and an excess part. This method seems to work well; the result agrees with the few data available, although substantially more data are needed for a better understanding of viscous flow in molten fluorides.

Chapter 6 gives a synthesis of the thesis and discusses the possibilities for a successful continuation of this study and the implications for the Molten Salt Reactor.

162

Bibliography

[1] Uranium Information Center; http://www.uic.com.au.

[2] http://www.geology.wisc.edu.

[3] H. G. MacPherson, Nucl. Sci. Eng. 90 (1985) 374.

[4] W. R. Grimes, Nucl. Appl. Tech. 8 (1970) 137.

[5] R. C. Bowman, Tech. Rep. Report ADNA/98-04 (1998).

[6] M. Hron, M. Mikisek, in: Atelier GEDEON-PRACTIS, Cadarache, France. Les Réacteurs à Sels Fondus et la Pyrochimie, 2002, pp. cd–rom.

[7] C. W. Forsberg, Reactors with Molten Salts: Options and Missions, Frédéric Joliot and Otto Hahn Summerschool 2004, Cadarache, France (2004).

[8] H. P. Nawada, K. Fukuda, J. Phys. Chem. Solids 66 (2005) 647.

[9] H. Boussier, Pyrometallical Processing Research Programme "PY-ROREP", no. FIS5-1999-00199, 2003.

[10] O. Conocar, N. Douyere, J. Lacquement, J. Nucl. Mater. 344 (2005) 136.

[11] J. Lacquement, S. Bourg, H. Boussier, O. Conocar, A. Laplace, M. Lecomte, B. Boullis, J. Duhamet, A. Grandjean, P. Brossard, D. Warin, in: Proceedings of GLOBAL 2005, Tsukuba, Japan, 2005, p. paper nr. 153.

[12] J. Serp, P. Lefebvre, R. Malmbeck, J. Rebizant, P. Vallet, J.-P. Glatz, J. Nucl. Mater. 340 (2005) 266.

164

[13] C. D. Bowman, E. D. Arthur, P. W. Lisowski, G. P. Lawrence, R. J. Jensen, J. L. Anderson, B. Blind, M. Cappiello, J. W. Davidson, T. R. England, L. N. Engel, R. C. Haight, H. G. H. III, J. R. Ireland, R. A. Krakowski, R. J. LaBauve, B. C. Letellier, R. T. Perry, G. J. Russell, K. P. Staudhammer, G. Versamis, W. B. Wilson, Nucl. Instr. and Meth. A 320 (1992) 336.

[14] J. Vergnes, D. Lecarpentier, Nucl. Eng. Design 216 (2002) 43.

[15] R. W. Moir, E. Teller, Nucl. Technol. 151 (2005) 334.

[16] H. S. Khalil, Generation IV Overview, Objectives and Scenarios, Frédéric Joliot and Otto Hahn Summerschool 2004, Cadarache, France (2004).

[17] R. J. M. Konings, J. P. M. van der Meer, E. Walle, Chemical aspects of Molten Salt Reactor Fuel, European Commission Joint Research Centre, 2005, JRC-ITU-TN 2005/25.

[18] D. Sedmidubský, O. Beneš, R. J. M. Konings, J. Chem. Thermodyn. 37 (2005) 1098.

[19] E. G. King, J. Am. Ceram. Soc. 79 (1957) 2056.

[20] C. J. O'Brien, K. K. Kelley, J. Am. Ceram. Soc. 79 (1957) 5616.

[21] W. B. Frank, J. Phys. Chem. 65 (1961) 2081.

[22] A. C. Macleod, J. Chem. Soc. Faraday Trans. I 69 (1973) 2026.

[23] F. Abdoun, M. Gaune-Escard, G. Hatem, J. Phase Equil. 18 (1997) 6.

[24] J. P. M. van der Meer, R. J. M. Konings, K. Hack, H. A. J. Oonk, Chem. Mater. 18 (2006) 510.

[25] W. H. Zachariasen, Acta Cryst. 1 (1948) 265.

[26] J. H. Burns, Inorg. Chem. 4 (1965) 881.

[27] J. C. van Miltenburg, G. J. K. van den Berg, M. J. van Bommel, J. Chem. Thermodyn. 19 (1987) 1129.

[28] R. E. Thoma, H. Insley, G. M. Hebert, Inorg. Chem. 5 (1966) 1937.

[29] M. W. Chase Jr.(ed.), NIST-JANAF Thermochemical Tables Fourth Edition, J. Phys. Chem. Ref. Data Monograph 9.

[30] A. D. Pelton, M. Blander, Metall. Trans. 17B (1986) 805.

[31] C. W. Bale, P. Chartrand, S. A. Degterov, G. Eriksson, K. Hack, R. Ben-Mahfoud, J. Melançon, A. D. Pelton, S. Petersen, CALPHAD 62 (2002) 189.

[32] M. Pelikan, D. E. Goldberg, E. Cantú-Paz, in: Proceedings of the Genetic and Evolutionary Computation Conference, 1999, p. 525.

[33] H. L. Lukas, E. T. Henig, B. Zimmermann, CALPHAD 1 (1977) 225.

[34] E. Thilo, H.-A. Lehmann, Z. Anorg. Chem. 258 (1949) 332.

[35] J. L. Holm, O. J. Kleppa, Inorg. Chem. 8 (1969) 207.

[36] D. M. Roy, R. Roy, E. F. Osborn, J. Am. Ceram. Soc. 33 (1950) 85.

[37] D. M. Roy, R. Roy, E. F. Osborn, J. Am. Ceram. Soc. 37 (1954) 300.

[38] A. V. Novoselova, Y. P. Simanov, E. I. Jarembash, Zh. Fiz. Khim. SSSR 26 (1952) 1244.

[39] R. E. Thoma, H. Insley, H. A. Friedman, G. M. Hebert, J. Nucl. Mater. 27 (1968) 166.

[40] K. A. Romberger, J. Braunstein, R. E. Thoma, J. Phys. Chem. 76 (1972) 1154.

[41] A. D. Pelton, Thermodynamics and phase diagrams of materials, Vol. 5, VHC, Weinheim, 1991, Ch. 1.

[42] C. E. Vallet, J. Braunstein, J. Am. Ceram. Soc. 60 (1977) 316.

[43] H. E. Cook, J. E. Hilliard, Trans. AIME 233 (1965) 142.

[44] B. F. Hitch, C. F. Baes Jr., Inorg. Chem. 8 (1969) 201.

[45] V. B. M. Hageman, H. A. J. Oonk, Phys. Chem. Glasses 27 (1986) 194.

[46] J. C. Mailen, F. J. Smith, L. M. Ferris, J. Chem. Eng. Data 16 (1971) 68.

[47] C. J. Barton, W. R. Grimes, H. Insley, R. E. Moore, R. E. Thoma, J. Phys. Chem. 62 (1958) 665.

[48] R. E. Thoma, H. Insley, H. A. Friedman, G. M. Hebert, J. Chem. Eng. Data 10 (1965) 219.

166

[49] S. Cantor, J. W. Cooke, A. S. Dworkin, G. D. Robbins, R. E. Thoma, G. M. Watson, Tech. Rep. Report ORNL-TM-2316 (August 1968).

[50] A. Büchler, J. L. Stauffer, in: Proceedings of the Symposium on Thermodynamics with Emphasis on Nuclear Materials, IAEA, Vienna, 1965, 1966, p. 271.

[51] A. Snelson, B. N. Cyvin, S. J. Cyvin, J. Mol. Struct. 24 (1975) 165.

[52] B. N. Cyvin, S. J. Cyvin, J. Mol. Struct. 24 (1975) 177.

[53] A. D. Pelton, P. Chartrand, G. Eriksson, Metall. Trans. 32A (2001) 1409.

[54] P. Chartrand, A. D. Pelton, Metall. Trans. 32A (2001) 1417.

[55] A. D. Pelton, Calphad 25 (2001) 319.

[56] G. W. H. Höhne, H. K. Cammenga, W. Eysel, E. Gmelin, W. Hemminger, Thermochim. Acta 160 (1990) 1.

[57] P. Chartrand, A. D. Pelton, Metall. Trans. 32A (2001) 1397.

[58] P. Chartrand, A. D. Pelton, Metall. Trans. 32A (2001) 1361.

[59] P. Chartrand, A. D. Pelton, Metall. Trans. 32A (2001) 1385.

[60] L. A. Khripin, Izv. Sibir. Otdel. Akad. Nauk SSSR, Ser Khim. Nauk 7 (1963) 107.

[61] G. A. Bukhalova, E. P. Babaeva, Russ. J. Inorg. Chem. 10 (1965) 1026.

[62] R. E. Thoma, G. D. Brunton, R. A. Penneman, T. K. Keenan, Inorg. Chem. 9 (1970) 1096.

[63] A. I. Agulyanskii, V. Bessonova, Russ. J. Inorg. Chem. 27 (1982) 579.

[64] C. J. Barton, L. M. Bratcher, R. J. Sheil, W. R. Grimes, Oak Ridge National Laboratory (1956, unpublished).

[65] C. J. Barton, R. A. Strehlow, J. Inorg. Nucl. Chem. 18 (1961) 143.

[66] C. J. Barton, J. D. Redman, R. A. Strehlow, J. Inorg. Nucl. Chem. 20 (1961) 45.

[67] F. Matthes, S. Holz, Z. Chem. 2 (1962) 22.

[68] T. Grande, Ph.D. thesis, University of Trondheim (1992).

[69] A. D. Pelton, P. Chartrand, Metall. Trans. 32A (2001) 1355.

[70] V. Dracopolous, B. Gilbert, G. N. Papatheodorou, J. Chem. Soc., Faraday Trans. 94 (1998) 2601.

[71] V. Dracopolous, B. Gilbert, B. Børrensen, G. M. Photiadis, G. N. Papatheodorou, J. Chem. Soc., Faraday Trans. 93 (1997) 3081.

[72] C. J. Barton, T. N. McVay, L. M. Bratcher, R. R. Grimes, Oak Ridge National Laboratory (1954, unpublished).

[73] E. P. Dergunov, Dokl. Akad. Nauk. SSSR 58 (1947) 1369.

[74] J. H. Burns, W. R. Busing, Inorg. Chem. 4 (1965) 1510.

[75] J. L. Holm, Acta Chem. Scand. 19 (1965) 638.

[76] R. E. Thoma, Advances in Molten Salt Chemistry, Vol. 3, Plenum Press, 1975, Ch. 6, p. 275.

[77] R. E. Thoma, H. Insley, B. S. Landau, H. A. Friedman, W. R. Grimes, J. Phys. Chem. 63 (1959) 1266.

[78] R. E. Thoma, H. Insley, H. A. Friedman, C. F. Weaver, J. Phys. Chem. 64 (1960) 865.

[79] L. V. Jones, D. E. Etter, C. R. Hudgens, A. A. Huffman, T. B. Rhinehammer, N. E. Rogers, P. A. Tucker, L. Wittenberg, J. Am. Ceram. Soc. 45 (1962) 79.

[80] C. F. Weaver, R. E. Thoma, H. Insley, H. A. Friedman, J. Am. Ceram. Soc. 43 (1960) 214.

[81] C. J. Barton, H. A. Friedman, W. R. Grimes, H. Insley, R. E. Moore, R. E. Thoma, J. Am. Ceram. Soc. 41 (1958) 63.

[82] J. P. M. van der Meer, R. J. M. Konings, M. H. G. Jacobs, H. A. J. Oonk, J. Nucl. Mater. 344 (2005) 94.

[83] F. Vaslov, A. H. Narten, J. Chem. Phys. 59 (1973) 4949.

[84] S. Cantor, D. S. Hsu, W. T. Ward, Tech. Rep. Report ORNL-3913 (March 1966).

[85] B. C. Blanke, E. N. Bousquet, M. L. Curtis, E. L. Murphy, Tech. Rep. USAEC MLM-1086 (1956).

[86] S. Cantor, W. T. Ward, C. T. Moynihan, J. Chem. Phys. 50 (1969) 2874.

[87] S. Cantor, Tech. Rep. ORNL-TM-4308 (1971).

[88] B. Porter, R. E. Meaker, Tech. Rep. BMI RI-6836 (1966).

[89] D. G. Hill, S. Cantor, W. T. Ward, j. Inorg. Nucl. Chem. 29 (1967) 241–243.

[90] S. Seetharaman, D. Sichen, F.-Z. Ji, Metall. Trans. 31B (2000) 105.

[91] V. N. Desyatnik, A. I. Nechaev, Y. F. Chervinskii, trans. from Zh. Prik. Kh. 54 (1981) 2310.

[92] Y. F. Chervinskii, V. N. Desyatnik, A. I. Nechaev, Russ. J. Phys. Chem. 56 (1982) 118.

[93] H. G. MacPherson, Tech. Rep. Report ORNL-2890 (October 1959).

Dankwoord

Velen hebben op de één of andere manier bijgedragen aan mijn proefschrift, maar degene aan wie ik veruit het meeste te danken heb is Rudy Konings. Je bent in één woord een fantastische begeleider, die iedere PhD student zich wel zou willen wensen.

Mijn dank gaat ook uit naar mijn promotor Harry Oonk. Je hebt me veel bijgebracht over mengentropieën, vormingsenthalpieën en Gibbsenergieën. Je was ons thermodynamisch geweten van deze studie, met veel oog voor stijl en detail; voor de puntjes op de i en de nulletjes bij de H.

Klaus Hack von GTT, Du hast uns viel gelehrt über FactSage, SUBG, Z-Werten und modellieren in allgemeinem. Die Zusammenarbeit hat mir auch viel Spaß gemacht; ein schönes Danke schön!

De lage temperatuurs calorimetrie experimenten waren niet mogelijk geweest zonder Aad van Genderen en Cees van Miltenburg.

Bedankt Michel Jacobs, voor het mij op gang helpen en me wegwijs te maken in het thermodynamisch modelleren.

Grote dank gaat ook uit naar Herwin Hein, voor het me zo goed op weg helpen met diverse experimenten. *Den Mitarbeitern von der ITU Werkstatt danke ich für die geleistete Arbeit (Tiegel, Presse, Handschuhkasten). Auch Christos Apostolidis danke ich, für das Thoriumfluorid, aber auch für deine muntere Haltung. Wenn jeder so arbeiten würde, wäre das Institut zehn Jahre weiter. David Sedmidubský, your experience with calorimeters was more than valuable. Thanks for sharing it with us; sometimes enjoying a 'pivo' in the meanwhile. Staying with the Czechs, I would also like to thank Ondrej Beneš, who will continue the thermodynamic modelling on molten salts. We had useful discussions and I found it really nice and inspiring to work together. We have laughed a lot too, together with my office mate Karin Popa, who is a man and not a girl, which sometimes led to funny confusions on the phone.*

169

170

Een persoon die een belangrijke plaats inneemt is Annemieke, mijn grote vriendin; ik geloof vanaf onze eerste wiskundeles op het IvA. Na onze geostudie (de állerleukste die er is), hebben we elk onze wegen gekozen. Op het moment van dit schrijven ben je je hard aan het voorbereiden om naar Amerika te gaan. Naar je vent en om te schitteren voor Shell. Het wordt ongetwijfeld een geweldige tijd voor jou, maar ik zal je natuurlijk erg missen. An, je bent mijn uitlaatklep voor werkfrustraties, relatieproblemen en allerhande zaken. En naast het lekker lachen samen, kun je met jou ook uitgebreid discussiëren over politiek, religie en de zin des levens. Dank voor je gezelligheid, je scherpe geest en voor wie je bent!

En hoe had ik ooit de lange dagen achter de computer door kunnen brengen zonder mijn mailvriend Der Pauli? Goed beschouwd gaat er nauwelijks een dag voorbij waarbij we elkaar niet op de hoogte stellen van ons wel en wee. De hoeveelheid zin, maar vooral ook de hoeveelheid onzin die we in de loop der jaren besproken hebben is onvoorstelbaar. Opblaaskrokodillen, Lada's, voor- en achterbaarden, u kunt het zo gek niet bedenken. Wat lang geleden begonnen was als een studentikoze Saxifraga-Tartaros flirt (nóg zie ik de bloempot met afwasborstels voor me), is inmiddels al lang uitgegroeid tot echte vriendschap.

Dank ook aan de Saxi-dames en de ouwe Utrecht club, alhoewel sommigen van jullie inmiddels ook uitgewaaierd zijn; voor jullie belangstelling, jullie bezoekjes hier in Duitsland en voor mijn logeerpartijtjes op mijn beurt als ik weer 's in het Stichtse was (Tuur). Een speciale vermelding voor de enige echte IJsbeer Martijn is ook gepast op deze plek.

Dear colleagues and ex-colleagues at the ITU, I would like to thank you all. For your company, good laugh, advice and help. Without forgetting or passing anyone, I will not try to mention every name. Of course I think of my fellow-students and friends, with whom I enjoyed a great time at the quiz nights in the Flynn's Inn, during simple coffee breaks and at innumerable dinners, barbecues and parties. I think of the colleagues with whom I swam, biked and participated in the memorable Linkenheimer Triathlon. However, there are a couple of names to be mentioned at this place though. Cathy, we have shared a good time. It is a pity you had to move so far, but I'm sure you're doing great in Canada. Jean, Jussi, Leena, Monique en mijn cultuurkompaan Stefaan, oftewel de man die alles kan; ik ben blij dat ik jullie heb leren kennen.

Thanks Denis for our friendship. Together with Jerome we used to form a sort of Bermuda triangle... And going together to the Oktoberfest with Freddi was an unforgettable experience. Matthias, nächstes Mal bist Du dabei.

Esther en Raúl, ik ben blij dat ik jullie heb ontmoet; het is heerlijk om zo af en toe 'ns lekker nederlands te praten. *Damon und Yuka, schön daß es euch gab hier in Karlsruhe. Das essen beim Bangkok, grillen im Park und besonders die Konzerte für moderne Musik werde ich nicht leicht vergessen. Ihr seid großartig!* De bizarste ontmoeting uit mijn leven tot nu toe was wel met met Liong-Seng, mijn achterbuurman. Toeval bestaat niet, daar ben ik nu van overtuigd. Liong, je bent een bijzonder persoon en ik heb vaak geboeid geluisterd naar jouw verhalen over China en Indonesië.

Het eerste wapenfeit van mijn verblijf in Karlsruhe, namelijk het vinden van een balletschool, en wel die van Carlos Lagunilla en Aina Reijerink, bleek een goede zet. Gesmolten zouten zijn niet altijd een passie gebleken; dansen daarentegen zou ik altijd en overal kunnen doen (zelfs in de lange gangen van het ITU, waar ik 's avonds laat nog wel eens een combinatie pleegde te oefenen). Ook het meedansen in Parsifal in Baden-Baden was een erg leuke ervaring.

En één van de personen met wie ik deze passie kan delen, is mijn zusje Chantal. Van kleine zus ben je in de loop der jaren grote vriendin geworden. Het is jammer dat we zo ver van elkaar wonen, maar dat maakt de weekenden samen des te leuker. Samen naar ballet, samen koken, wandelen in het Zwarte Woud, kamperen in de Pfalz en daarna bibberen van de kou in het tropisch zwembad... Je bent ook een lekker gek wijf af en toe, maar ik ben supertrots op je!

Dit brengt me als laatste bij mijn ouders. Ik dank jullie voor jullie niet aflatende ondersteuning en voor alles wat jullie voor me hebben gedaan.

Curriculum Vitae

Ik werd op 9 mei 1978 in Alphen aan den Rijn geboren. Na daar de eerste 10 jaar van mijn leven te hebben doorgebracht, verhuisden we naar Rijnsburg. Mijn middelbare school doorliep ik aan het Stedelijk Gymnasium te Leiden. Direct daarna, in september 1996, begon ik met de studie geologie aan de Universiteit Utrecht. Na het cum laude behalen van mijn propaedeuse besloot ik verder te gaan met de vervolgstudie geochemie. Ik specialiseerde me in materiaalkunde en petrologie. Tot de hoogtepunten van mijn studie behoorden onder andere een geochemisch veldwerk in de Pilbara in Australië en een stage bij staalbedrijf Corus te IJmuiden. Mijn afstudeerscriptie behelsde een studie naar de oorsprong van Sangihe lavagesteenten uit Noord-Indonesië, met behulp van Sr, Nd en Pb isotopen. Nadat ik mijn doctoraaldiploma in de geochemie, met het judicium cum laude, had behaald, begon ik in januari 2003 met mijn promotieonderzoek aan het Instituut voor Transurane Elementen in samenwerking met de Universiteit Utrecht, waar ik ook mijn proefschrift verdedig. Per najaar 2006 werk ik als post-doc voor het franse CEA (Commissariat à l'Energie Atomique) in Marcoule.

I was born on 9 May 1978 in Alphen aan den Rijn. After living there the first 10 years of my life, we moved to Rijnsburg. I got my secondary education at the Stedelijk Gymnasium in Leiden. Immediately after, in September 1996, I started with the study geology at Utrecht University. After the first year (propaedeuse) I decided to continue with geochemistry. My specialisations were materials science and petrology. Remarkable highlights of my study were a geochemical fieldwork in the Pilbara, Australia, and an internship at the Corus steel plant in IJmuiden. My Master thesis dealt with a study on the origin of volcanic rocks from the Sangihe Arc, North Indonesia, using evidence from Sr, Nd and Pb isotopes. After graduating in geochemistry (with the

highest distinction), I started my PhD project at the Institute for Transuranium Elements in January 2003. This was done in collaboration with Utrecht University, where the defense of this thesis takes place. As from the autumn 2006, I work as a post-doc for the French CEA (Commissariat à l'Energie Atomique) at Marcoule.